Giulia Longo

Hybrid perovskites for light-emitting and photovoltaic devices

2017

VNIVERSITAT DE VALÈNCIA

Doctorado de Nanociencia y Nanotecnología

Tesis doctoral

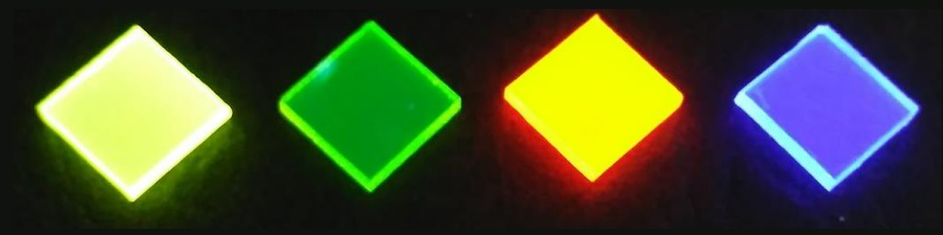

Hybrid perovskites for light-emitting and photovoltaic devices

Giulia Longo

Junio 2017

Directores:
Dr. Hendrik Jan Bolink
Dr. Michele Sessolo

VNIVERSITAT DE VALÈNCIA

Doctorado en Nanociencia y Nanotecnología

Ph.D. thesis:

Hybrid perovskites for light-emitting and photovoltaic devices

Ph.D. candidate:

Giulia Longo

Supervisors:

Dr. Hendrik Jan Bolink

Dr. Michele Sessolo

Tutor:

Dr. Hendrik Jan Bolink

Junio 2017

Dr. Hendrik Jan Bolink y **Dr. Michele Sessolo**, Investigador de la Universidad de Valencia en el Instituto de Ciencia Molecular (ICMol) e Investigador Postdoctoral del Instituto de Ciencia Molecular, respectivamente, certifican que la memoria presentada por la doctoranda Giulia Longo con el título "Hybrid perovskites for light-emitting and photovoltaic devices" corresponde a su Tesis Doctoral y ha sido realizada bajo su dirección, autorizando mediante este escrito la presentación de la misma.

En Valencia, a 5 de junio del 2017

Dr. Hendrik Jan Bolink	Dr. Michele Sessolo
(director y tutor)	(director)

Dedicato a tutte le mie famiglie,

naturali, scelte e incontrate

Index

Aknowledgments

First of all I would like to thank my thesis director, Dr. Hendrik Jan Bolink to accept me in his wonderful group giving me this possibility. Thanks for your support over these years. Altro sentito ringraziamento va diretto al Dr. Michele Sessolo, co-direttore della mia tesi e instancabile fonte di idee. Grazie Michele, senza il tuo aiuto e i tuoi suggerimenti (e i tuoi caffé) questa tesi non sarebbe stata possibile. Grazie di cuore.

A continuación, tengo que agradecer mucho a mis compañeros de trabajo por haber sido mi familia durante estos 4 años, sin vosotros no habría aguantado tanto! Gracias Lidón por tu capacidad de transmitir paz y serenidad, tan necesarias durante un doctorado! Cristina, gracias por tu amistad y compañía. Gracias a Laura por su inagotable energía, por sus retos y por sus patines. Gracias María por haber sido mi hermana mayor durante estos años, por acogerme en tu casa y por simplificarnos la vida con todo el papeleo! Gracias Toni por enseñarme tanto y por ser siempre disponible a ayudar. Jorge A., gracias por tu humor tan malo y tan parecido al mío!! Gracias a Dani por apuntarse siempre a cualquier plan y por llevarnos en su coche a pesar de nuestros comentarios! Gracias Pablo por tu ayuda y tus explicaciones de física! Thank you Azin for being so "crazy" and for cooking so well! Benni, thank you for being so funny and for all the coffee you paid me! Grazie a Maria Grazia, per aver condiviso con me le gioie e i nervosismi inevitabili durante una tesi! Gracias Jorge F. por tu incansable ayuda con todos los equipos del laboratorio….sin ti estaríamos todos perdidos! De igual manera, gracias Ángel, por tu corazón de oro y por querer siempre ayudar! Gracias Alejandra por todas las medidas que me hiciste! Thanks to all the people that already left the group, Dani, Cristina, Olga, David, Enrico, and thanks to those who joined our group for some time....you have been part of this fantastic family to which I will be always grateful!

Un grazie speciale alla mia famiglia, che mi ha accompagnato ogni giorno non facendomi mai sentire sola o senza appoggio, nonostante la distanza. E, infine, un grazie di cuore a Luca, mio compagno di vita, che mi ha sostenuto nei momenti piú difficili.

Questa tesi é per tutti voi, spero possiate esserne orgogliosi. Grazie.

Chapter 1.

Introduction and aim of the thesis.

1.1 Hybrid perovskites

The name perovskite identifies minerals with a crystal structure similar to the one of calcium titanate $CaTiO_3$. The name derives from the Russian mineralogist Lev Perovski, and applies to all compounds with general crystal structure AMX_3. A particular subclass of these materials includes the hybrid perovskites, where A is an organic cation, M a divalent transition metal and X a halide. The perovskites studied in this work are based on lead (Pb^{2+}), however hybrid perovskites with Sn^{2+}, Ge^{2+}, Sb^{3+} and Bi^{3+} have also been reported.[1-4] The structure of hybrid lead halide perovskites consists in a lattice of corner sharing PbX_6 octahedra intercalated with the organic cation A. In order to create stable 3D structure, the cation A must fit in the cavity delimited by four adjacent lead halide octahedra. This geometrical constrain can be expressed by the Goldschmidt tolerance factor[5]

$$t = \frac{r_A + r_X}{\sqrt{2}(r_M + r_X)}$$

Equation 1

Where r represents the ionic radii of A, X or M, as indicated. In lead halide perovskites, a tolerance factor of $0.7 < t < 1.1$ predicts stable structures, and this applies to organic cations such as methylammonium (MA) and formamidinium (FA). If a larger cation is used, the 3D lattice collapses into a two dimensional structure characterized by the alternation of inorganic MX_4 sheets and organic layers (Fig. 1).[6] The alternation of semiconducting metal-halide sheets and insulating organic layers creates a quantum well structures with large energy barriers between the conduction/valence band of adjacent inorganic component and the LUMO/HOMO of the organic part. In this situations excitons are localized in the inorganic sheets and their exciton binding energy increases up to hundreds of meV.[7, 8]

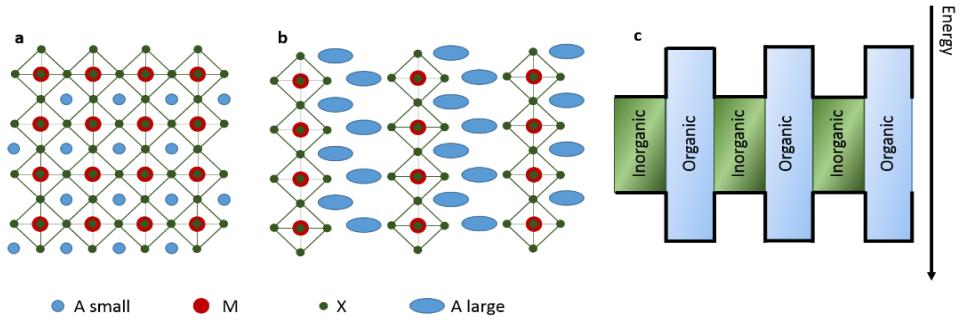

Fig. 1 *Schematic representation of* ***a)*** *3D and* ***b)*** *2D perovskite structures.* ***c)*** *Energy profile for a 2D perovskite structure.*

The first studies on the application of perovskites as active materials for electronic devices were conducted on the two dimensional perovskites, due to their high exciton binding energy. Strong photo- and electroluminescence were demonstrated, even if only at low temperatures.[9, 10] More recently, thanks to the promising photovoltaic performances of $MAPbI_3$,[11, 12] several studies appeared on the electroluminescent properties of the methylammonium lead halide ($MAPbX_3$)[13] family. 3D perovskite are appealing materials for optoelectronic applications for the following characteristics:

- Simple tuning of the band gap energy (E_g).

  The bottom of the conduction band of hybrid perovskite is mainly formed by the *p* orbitals of the Pb atoms,[14] while the valence band maximum is mainly composed by the *p* orbitals of the halide. Consequently the substitution of the halide leads to a modulation of E_g that is enlarged with lighter halides,[15, 16] providing small bandgap materials (*i.e.* $MAPbI_3$, E_g ~ 1.6 eV) suitable for photovoltaic applications as well as large bandgap compounds ($MAPbBr_3$, E_g ~ 2.3 eV) appealing for light-emitting devices. Moreover, by mixing different halides one can tune E_g over a wide spectral range (Fig. 2).

- Low exciton binding energy.

  This feature implies spontaneous and efficient charge separation at room temperature, highly desirable for photovoltaic applications. The binding

energy can be increased by substitution of the halide or through morphological modifications.

- Large absorption coefficient.
  The strong light absorption ($\alpha > 10^5$ cm^{-1}, Fig. 2), comparable to inorganic semiconductors such as GaAs, permits to create large number of photo-generated carriers, leading to high photocurrent generation with relatively thin films.[17]

- Long-range diffusion length and high carrier mobilities.
  Highly desirable for maximizing the charge extraction/injection from/into a perovskite thin film.

- Inexpensive precursor materials and simple synthesis.
  Methylammonium and lead halides are inexpensive compounds, which can be easily processed by solution or vacuum techniques (details in the following paragraph).

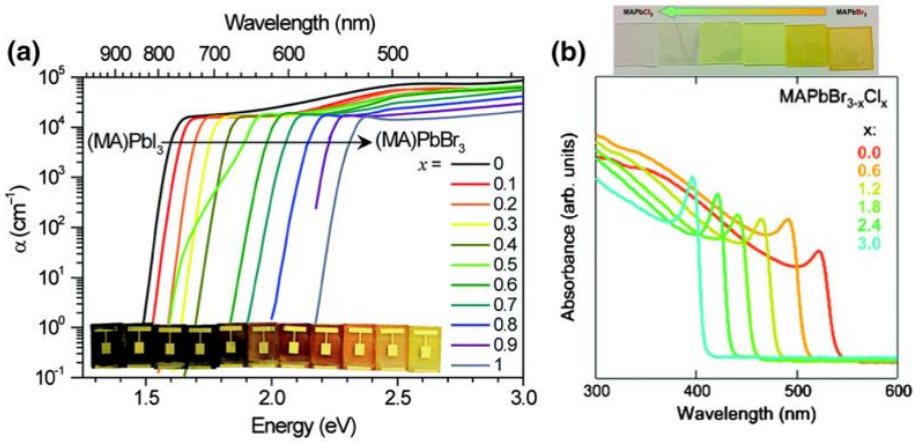

Fig. 2 a) *Absorption coefficient of mixed MAPb($I_{3-x}Br_x$) thin film with increasing bromide content, adapted from reference 18.* ***b)*** *Absorption coefficient of mixed MAPb($Br_{3-x}Cl_x$) thin film with increasing chloride content, adapted from reference 19.*

As mentioned before, the perovskite morphology can induce relevant differences irrespectively of the material stoichiometry. For example, it has been

demonstrated that large $MAPbI_3$ crystals are characterized by excitonic states which are absent in smaller grains.[20] This implies that the perovskite thin-film deposition is an important step at the moment of preparing optoelectronic devices, since different deposition techniques will lead to different morphologies and properties. The most important deposition methods will be discussed in the following section.

1.2 Deposition techniques

One of the advantages of hybrid perovskites, when compared to more traditional semiconducting materials, is the possibility to use several simple deposition techniques to form high quality perovskite films.[21-23] However, different deposition methods, as well as different substrates, can lead to diverse film morphologies and properties[24] highlighting the importance of selecting the most appropriate process depending on the desired application. The deposition methods commonly used for the preparation of perovskite films can be divided in two subclasses, the solution-based and the vacuum assisted techniques. Each of them includes a variety of modified processes, which will be discussed below.

1.2.1 Solution-processing methods

Solution-based deposition techniques are the most widespread for the preparation of perovskites films for both solar cells and light-emitting diodes (LEDs). These methods are simple and potentially inexpensive, and can be implemented in roll-to-roll fabrication, which is suitable for large area production. The precursors of the perovskite are highly soluble in common solvent, such as dimethylformamide (DMF), dimethyl sulfoxide (DMSO) or γ-butyrolactone. Two main approaches can be followed: a single step deposition or a sequential deposition route. In the single step deposition (Fig. 3a), solutions of the organic and inorganic precursors (usually in DMF or DMSO), are deposited on a substrate by spin-, meniscus/blade- or dip-coating. The crystallization of the film relies on the evaporation of the solvent, which often requires a subsequent thermal treatment.

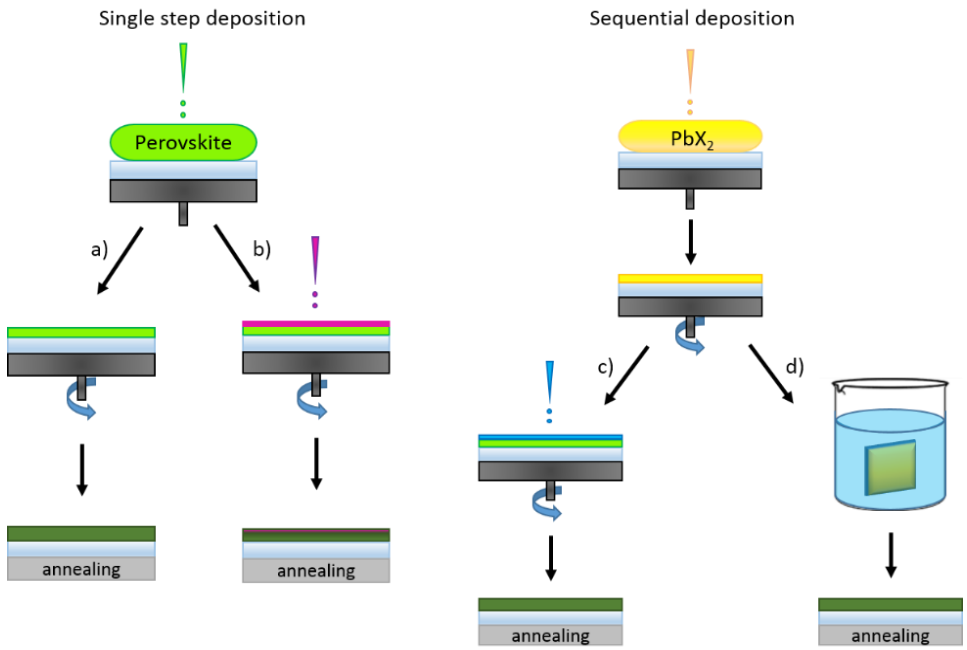

Fig. 3 *Scheme of solution-based deposition methods. One-step deposition* ***a)*** *without and* ***b)*** *with anti-solvent dripping. Sequential deposition with intercalation of methylammonium through* ***c)*** *spin-coating or* ***d)*** *dip-coating.*

Since the film morphology influences the optoelectronic properties of the perovskite, a careful control over the crystallization kinetics is essential.[25] The use of solvents with high boiling point, as well as the change in the precursor stoichiometry, can lead to substantial changes in the final film morphology. Typically, volatile solvents lead to a fast drying of the layer and hence crystallization in the form of small crystals. On the other hand, high boiling point solvents leave more time for the nucleation centers to grow, resulting in larger grains.[26, 27] The wettability of the perovskite solution on the substrate is also critical for the control of the crystallization process. Due to the polar nature of the perovskite precursors and solvents, polar surfaces ensure a larger contact angle and more compact and uniform layers. The substrate surface can be activated by exposure to oxygen plasma or ozone treatments, as well as with a simple pretreatment by spin coating with the perovskite solvent. An interesting variation to control the crystallization kinetics during the spin-coating consists in dripping a non-polar solvent on the forming perovskite layer in order to induce a

rapid crystallization (Fig. 3b).[27] The anti-solvent effect can be modulated by changing its nature and the dripping time.[28] In addition, a passivating agent can be added in the non-polar solvent during the dripping step, helping passivation of surface traps and enhancing the optical properties of the perovskites.[29] An alternative method is the sequential deposition,[30] where the inorganic and organic precursors are sequentially deposited to form the perovskite film. The lead halide layer is spin coated and then converted to perovskite through the intercalation of the organic molecules by spin- or dip-coating in a methylammonium solution (Fig. 3c and d respectively).[31-33] The process usually involves an annealing step which promotes the organic cation intercalation and the perovskites formation. This route leads to uniform and compact layers with improved photovoltaic and electroluminescence properties.

1.2.2 Vacuum deposition

Physical vapor deposition methods are widely employed in the semiconductor industry for the preparation of optoelectronic devices, and its use for the formation of perovskite (3D and 2D) thin films have been also reported.[34, 35]

Vacuum deposition presents many advantages compared to solution processing techniques:

- High purity of the precursors.
  The sublimation at controlled temperature in high vacuum can separate impurities with different volatility.

- Fine control of the layer thickness and stoichiometry
  Using very sensitive quartz crystal microbalances (QCMs), the thickness of the film can be monitored during the deposition with sub-nanometer precision, and a mechanical shutter can be closed when the desired thickness is reached. This allow to prepare devices in which the film thickness must be extremely precise, like optical cavities and resonators. In addition the

separate control of the precursor evaporation rates permits a fine control of the stoichiometry and composition of the perovskite material.

- Additive technique.
  Physical vapor deposition is intrinsically additive, which allows the design of multilayer devices. Differently from solution deposition methods, evaporation allows to form high quality perovskite films without the need to employ orthogonal solvents.

- Compatible with a wide range of substrates.
  If the deposition is carried out in stoichiometric conditions, no thermal treatments are needed, allowing the preparation of films on sensitive substrates such as plastics or textiles.

There are three main strategies to form perovskite layers through vacuum assisted deposition: dual source vacuum deposition, flash evaporation and sequential evaporation (Fig. 4). In the dual source deposition (Fig. 4a), the perovskite precursors are placed in thermally controlled ceramic crucibles inside a high vacuum chamber. The samples, protected by a mechanical shutter, are placed above the thermal sources. The precursors are simultaneously heated to their corresponding sublimation temperatures and condense on the substrates, forming the perovskite layer. Dual source deposition has been used for both 2D and 3D hybrid perovskites,[34, 36] demonstrating the flexibility of the method. The stoichiometry can be finely tune by the control of the evaporation rates of the single components,[22] leading to the formation of compact and uniform films with well-connected grains and smooth surfaces. Employing different halides precursors, mixed anion perovskite can also be prepared.[37]

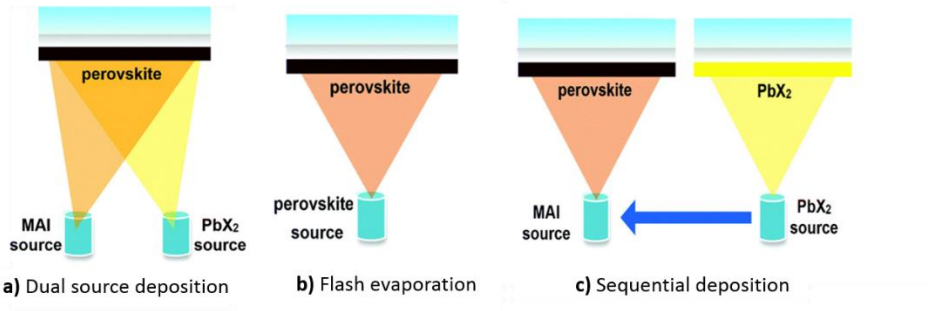

Fig. 4 *Schematic representation of the* ***a)*** *dual source vacuum deposition,* ***b)*** *flash evaporation and* ***c)*** *sequential evaporation methods*

Flash evaporation (Fig. 4b) is a deposition methods where only one material source is used. A pre-synthesized perovskite in the form of powders or thin film is deposited on a metal foil and connected to two electrodes in a high vacuum chamber. A high current is applied to the metal causing instantaneous (few seconds) evaporation of the material that is transferred on the substrate maintaining the initial stoichiometry and composition.[38] This technique will be discussed in details in chapter n.2.

The third vacuum-based approach is a sequential method in which the perovskite is formed by subsequent deposition of the inorganic and organic precursors (Fig. 4c). Similarly to the sequential solution deposition, the as-deposited film is usually annealed to ensure complete conversion of the precursors to perovskite.[39]

Solution and vacuum-based deposition techniques can be combined in order to obtain films with the desired thickness and morphology. Vacuum deposited lead halide layers can be converted to perovskite by spin-coating of the organic precursor solution, as well as solution deposited PbX_2 films can be exposed to methylammonium vapors and converted to perovskite.[23, 40, 41]

There is no an ideal deposition technique for the preparation of perovskite thin-films. Several factors (like the perovskite formulation, the desired film thickness or the type of substrates or underlying layers) influence the choice of the most suitable method. In this thesis flash evaporation (Chapter 2), dual-source

evaporation (Chapter 3) and single-step spin-coating (Chapter 4), will be employed, and the details of each process will be further discussed in the corresponding chapters.

1.3 Working principles and figures of merit of solar cells

In a perovskite solar cell the perovskite film absorbs light, creating holes and electrons pairs which separate and are selectively extracted by the hole and the electron extraction materials and collected at the electrodes. Under photo-excitation, bound-excitons or free carriers can be created, depending on the coulombic interaction between electrons and holes (defined as the exciton binding energy, E_g). Perovskites generally show low exciton binding energies (comparable to the thermal energy at room temperature), resulting in the formation of free electrons and holes after illumination. For efficient photovoltaic applications the mobility of the photo-generated charges ($\mu_{n,p}$) should be high, in order to ensure their extraction before their recombination. The mobility can be expressed with the following equation:

$$\mu_{n,p} = \frac{e\,\tau_{n,p}}{m^*_{n,p}}$$

Equation 2

Where e is the electron charge, $m^*_{n,p}$ the effective mass of the charges and $\tau_{n,p}$ the carrier lifetime. Perovskites present low effective masses (0.1-0.15m_0, with m_0 the free electron mass)[42] that can be compared to those of GaAs and Si. The carrier lifetimes are also long, in the order of hundreds of ns (like GaA, even if higher values have been reported).[43] In principle the combination of these parameters should lead to high mobilities, however the experimentally determined mobilities are relative modest,[44, 45] approximately two orders of magnitude lower compared to inorganic semiconductors. It has been suggested that the carrier mobility is limited by the scattering phenomena due to lattice vibrations or defects.[46] While defects could induce a trap density potentially detrimental for the device, the

presence, nature and distribution of traps is still under investigation. It has been shown that in polycrystalline $MAPbI_3$ both shallow and deep traps are present,[47-49] even though it remains difficult to assign a general density or profile of traps in perovskites. In fact, the density and nature of the traps can be influenced by several factors, like morphological changes or processing variations. Representative values of these parameters are reported in Table 1.

Material	**μ ($cm^2V^{-1}s^{-1}$)**	**$\tau_{n,p}$ (μs)**	**$m^*_{n,p}$ (m_0)**	**Trap density (cm^{-3})**
$CH_3NH_3PbI_3$ polycrystalline film	1–10	0.01–1	0.10–0.15	10^{15}–10^{16}
$CH_3NH_3PbI_3$ single crystal	24–105	0.5–1	—	(1–3)×10^{10}
$CH_3NH_3PbBr_3$ polycrystalline film	30	0.05–0.16	0.13	—
$CH_3NH_3PbBr_3$ single crystal	24–115	0.3–1	—	(0.6–3)×10^{10}
Si	1450	1000	0.19	10^8-10^{15}
GaAs	8000	0.01–1	0.063	

Tab. 1 *Values of mobility (μ), lifetime (τ), effective mass (m^*) and trap density of $MAPbI_3$, $MAPbBr_3$, Si and GaAs. Table adapted from reference 46.*

The charge carrier recombination depends on several factors, but it has been shown that under normal solar cell operating conditions, trap-assisted recombination is the dominant recombination path.[50] In planar solar cells (the solar cell architecture that will be treated in this work) long electron and hole diffusion lengths (the average length that charges can travel before recombining) are highly desirable for the fabrication of efficient devices.[51,52] Importantly, all these parameters are strongly affected by the change in the morphology and by the composition of the perovskite absorber.

The performances of solar cells are evaluated by measuring the J-V characteristics of the cell under illumination with a calibrated light-source. The current density can be described by the classical Schockley diodes equation (Equation 3) accounting for the photo-generated current J_L, as expressed below:

$$J = J_0 \left[\exp\left(\frac{qV}{\eta kT}\right) - 1\right] - J_L$$

Equation 3

From the J-V curve, the figures of merit for a solar cells can be extracted:

- Short circuit current density (J_{SC}, mA cm^{-2})

  It is the current density at short circuit conditions (zero applied voltage). The short circuit current can be described with the following expression:

$$J_{SC} = q \int_0^{\infty} EQE_{PV}(E)\, \phi_{AM1.5}(E)\, dE$$

Equation 4

  Where EQE_{PV} is the photovoltaic external quantum efficiency (the number of extracted charges over the number of absorbed photons) and $\varphi_{AM1.5}$ is the photon flux hitting the devices. The short circuit current depends on a number of factors not related with the active materials, like the incident light spectrum and power or the device active area. The short circuit current diminishes as the bandgap of the photoactive material increases, due to the lower absorption of the solar spectrum.

- Open-circuit voltage (V_{OC}, V)

  It is the voltage at zero current, and it represents the maximum available voltage from a solar cell. Its expression is presented below:

$$V_{OC} = \frac{kT}{q} \ln\left(\frac{J_{SC}}{J_0}\right)$$

Equation 5

  The V_{OC} inversely depends on the saturation current of the device, a constant parameter which depends on the absorber and on the diode quality. In the radiative limit, if non-radiative recombination is minimized (in favor of

radiative recombination), the higher is the V_{OC} (see Chapter 4). In contrast with J_{SC}, the open circuit voltage increases as the bandgap of the material increases, due to the increased potential energy of the photo-generated carriers.

- Fill factor (*FF*, %)

  It is defined as the ratio of the maximum theoretical power from the solar cell (maximum power point) and the product of V_{OC} and J_{SC}. In a simpler way, the fill factor measures the "squareness" of the J-V curve as the ratio of the rectangle defined by V_{OC} and J_{SC}, and the largest rectangle that fit inside the IV curve (Fig. 5). The *FF* quantifies the efficiency of the transport and extraction of the charges in a solar cell, hence is not influenced only by the active material, but also by the device design and architecture.

- Power conversion efficiency (*PCE*, %)

  The efficiency of a solar cell is determined as the fraction of incident power (P_{in}) which is converted to electricity, and can be expressed as:

$$PCE = \frac{FF \cdot V_{OC} \cdot J_{SC}}{P_{in}} \cdot 100$$

Equation 6

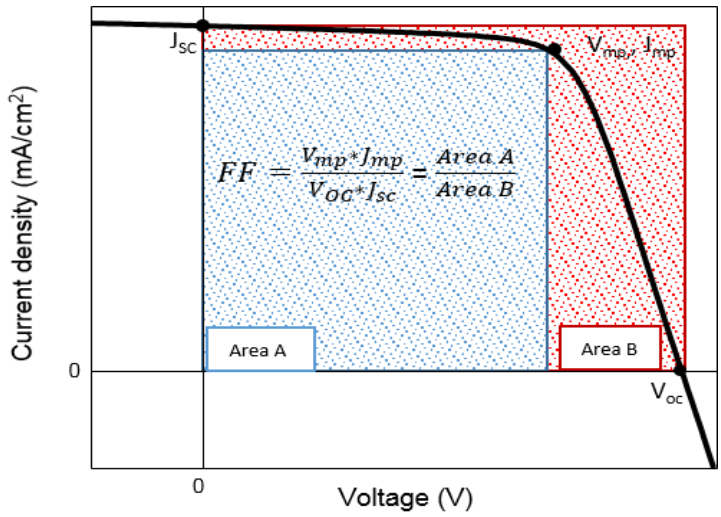

Fig. 5 *Representative J-V curve under illumination for a perovskite solar cell.*

A J-V scan measured in the dark is also useful, providing information about the quality of the diode. Another important parameter in a solar cell is the external quantum efficiency (EQE_{PV}), defined as the ratio between the number of carriers collected by the device and the number of absorbed photons at a given energy. In an ideal cell, where no losses occur and all the absorbed photons are converted to charges which are efficiently extracted, the *EQE* would be unity at energies equal or higher than the material bandgap. In a real solar cell, the *EQE* is limited by charge recombination, parasitic absorbance and reflection phenomena.

1.4 Working principles and figures of merits of organic light-emitting diodes

Organic light-emitting diodes (OLEDs) are multilayer devices in which a luminescent material is sandwiched between organic semiconducting layers that selectively inject electrons and holes in the active material. The recombination of the injected charge carriers in the emissive material is the process of electroluminescence. When positively and negatively doped semiconducting materials are put in contact, a p-n junction is formed. Several models have been used to describe the behavior of different junctions, however a specific model for

hybrid perovskite diodes has not yet been developed. Perovskites are intermediate materials between inorganic and organic semiconductors, showing features belonging to both materials classes which limit the application of traditional models used for inorganic semiconductors. An approximation of a perovskite diode, as described by several authors, is the p-i-n junction, where perovskite acts as intrinsic material in between oppositely doped regions.[53]

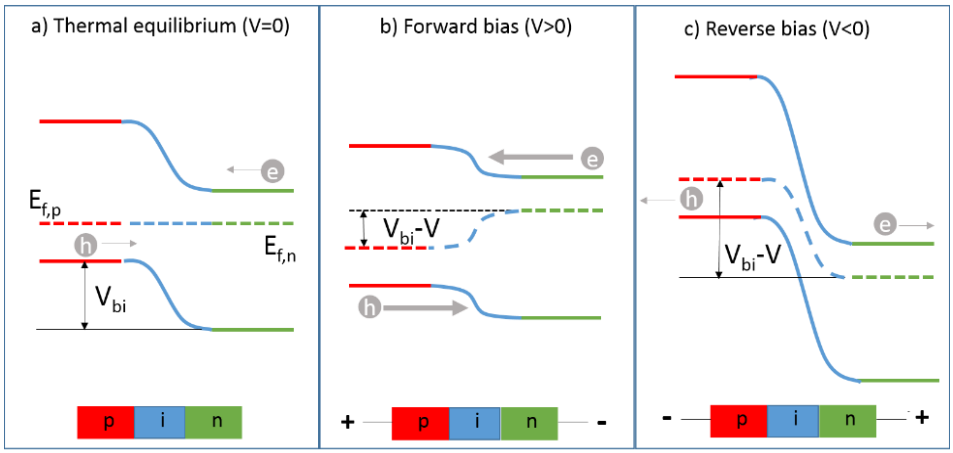

Fig. 6 *Energy profile of a p-i-n junction with* ***a)*** *no voltage applied,* ***b)*** *forward voltage applied and* ***c)*** *application of reverse voltage.*

When the external electrode are short-circuited, the Fermi levels of the materials align, and the potential (built-in potential, V_{bi}) drops over the intrinsic region due to the lack of charges (Fig. 6a). If a forward bias is applied (Fig. 6b), the current density vs. voltage (J-V) characteristics are characterized by three regimes (Fig. 7). In the first regime only the leakage current (1), linearly dependent on the voltage, is observed. When a small positive voltage, lower than the V_{bi}, is applied to the diode, electrons and holes diffuse towards the intrinsic region attracted by the opposite carriers concentration, creating the diffusion current regime (2). The diffusion limited current shows exponential dependence on the voltage and can be expressed by the classical Shockley diode equation

$$J = J_0 \left[\exp\left(\frac{qV}{\eta kT}\right) - 1\right]$$

Equation 7

Where J_0 is the saturation current, q the elemental electron charge, k the Boltsmann's constant, T the temperature and η the ideality factor. The latter is an important parameter that contains information on the type of recombination occurring in the device. If voltages higher than V_{bi} are applied, then electrons and holes are injected in the active material, creating a drift current (3). In traditional OLEDs the current in the drift regime is space-charged limited. The low mobility of the organic materials translates in an accumulation of charges that limits the current at high voltages. However the mobility of the perovskite is higher compared to organic semiconductors, reducing the space charge limitation. Finally, if a reverse bias is applied (Fig. 6c), no current flows through the junction and depletion of carriers occurs.

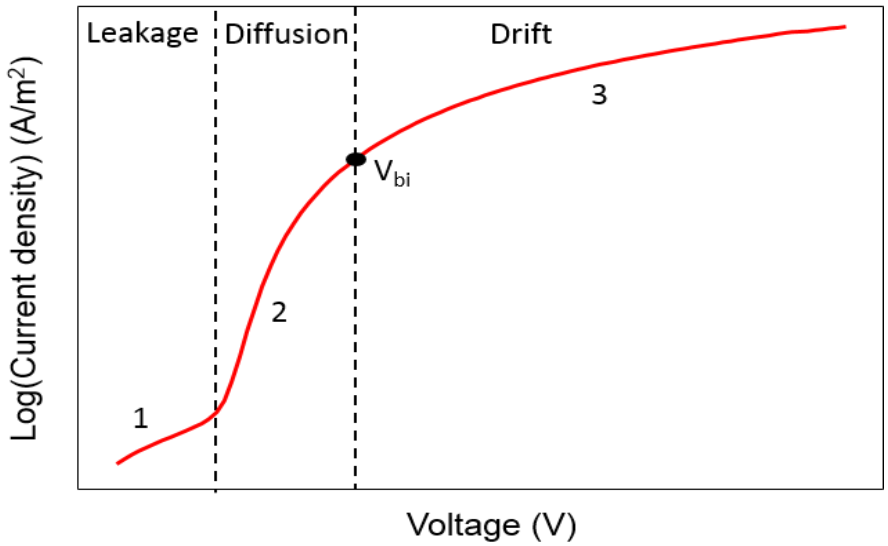

Fig. 7 *Diode regimes in a forward current density-voltage curve.*

Commonly used figures of merit for LEDs include:

- Luminance (cd/m^2)

  It represents the intensity (expressed in candelas) of light emitted by the device per unit of surface in a given direction, and takes into account the human eye sensitivity curve.

- Current density (A/m^2)

  It corresponds to the electrical current per unit area of the device.

- Current efficiency (cd/A)

  It is one of the way to express the efficiency of an OLED, as the ratio of the luminance with the correspondent current density.

- Power efficiency (lm/W)

  It is the ratio of luminous flux to power, hence it takes into account not only the current density but also the applied voltage of the diode. One lumen is defined as the luminous flux emitted by an isotropic source that emits 1 candela for each solid angle of 1 steradian (Lm=Cd*sr)

- External quantum efficiency (EQE_{EL}, %)

  This expression defines the number of emitted photons over the number of injected electrons. A deeper insight of this figure of merit will be given in the introduction of Chapter 4.

1.5 Device architectures

The first reports on the photovoltaic properties of hybrid perovskites were based on a liquid-electrolyte dye-sensitized solar cell, where the molecular sensitizer was substituted by $MAPbI_3$ and $MAPbBr_3$ nanocrystals.[54, 55] In these pivotal works, perovskites were placed on the surface of mesoporous TiO_2, and only used as light harvester, while the separation and transport of the charges relied on the electron and hole transport materials (TiO_2 and the liquid electrolyte, respectively). When the excellent charge transport properties of perovskite were discovered, mesoscopic n-i-p junctions with perovskite were developed (Fig. 8a). In this architecture, which is the most widely reported in literature, the perovskite is deposited on a thick mesoporous metal oxide layer, acting at the same time as absorber and holes transporter.[56, 57] Later studies revealed how perovskites can

efficiently transport both electrons and holes, leading to the development of planar device architectures.[12] In this configuration the perovskite not only photo-generates charges, but also transports them to the corresponding transport layers, that selectively extract holes and electrons.[35] The most representative structure is a n-i-p planar architecture (Fig. 8b) where the front contact consists in a fluorine doped tin oxide (FTO) film coated with a compact TiO_2 layer, and the hole transport material (HTM) is an organic semiconductor (generally spiro-OMeTAD). On a later stage, p-i-n planar structures were also developed (Fig. 8c), where the hole extraction occurs at the transparent conducting oxide (indium tin oxide, ITO), usually coated with PEDOT:PSS (Poly(3,4-ethylenedioxythiophene)-poly(styrenesulfonate)), while the electron transport is ensured by a layer of fullerene derivative. Being perovskite an ambipolar semiconductor, mesoscopic p-i-n devices were also developed, in which the hole transport relies on mesoporous NiO (Fig. 8d), and electron transport on perovskites.[58]

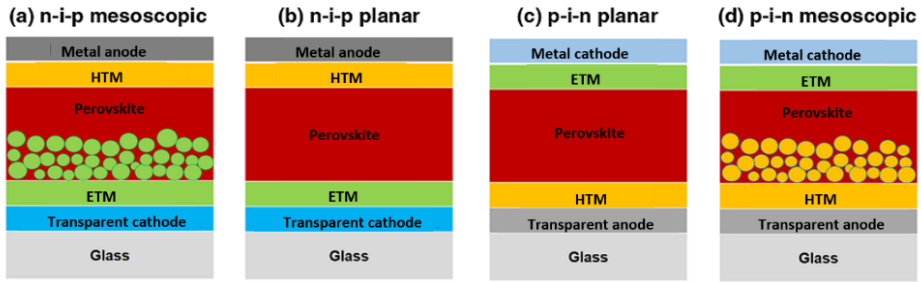

Fig. 8 *Classical architectures of perovskite solar cells and perovskite light-emitting devices. Adapted from reference 59.*

Perovskite light-emitting diodes (PeLED) are usually prepared in a planar configuration, since the applied potential must result in a homogenous field distribution through the device. The transport materials (especially the electron transport material ETM) employed in PeLEDs are however different from the ones used in solar cells. In the latter the photo-generated carriers have to be extracted from the perovskite to the electrodes, with no energy barriers between the perovskite conduction/valence band, and the lowest unoccupied/highest

occupied molecular orbital (LUMO/HOMO) of the ETM/HTM. Finally, to ensure efficient electron extraction, ohmic contact between the ETM and the cathode must be insured (Fig. 9a).

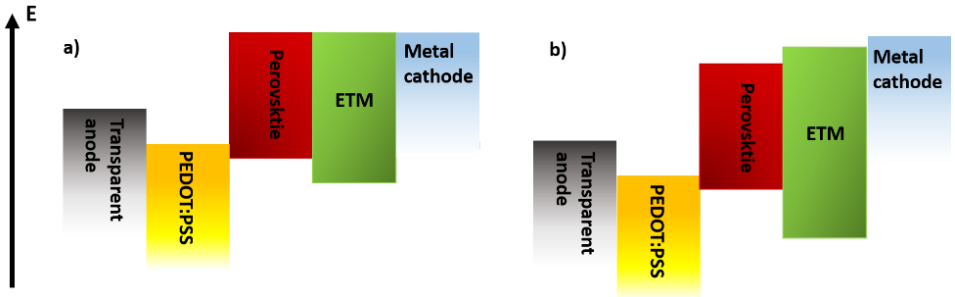

Fig. 9 *Schematic flat band energy diagrams for* ***a)*** *perovskite solar cells and* ***b)*** *perovskite light-emitting devices with p-i-n planar architecture.*

In light-emitting diodes, instead, electrons and holes have to be injected and confined in the perovskite layer. Low work function cathodes (such as Ba or Ca) are used to inject electrons into the low energy LUMO of the ETM (Fig. 9b). The electron transport material has also the role of hole blocking material, thanks to the typically deep HOMO level. The use of low work function metals might affect the device stability, requiring rigorous encapsulation. The preparation of inverted n-i-p planar junctions,[60, 61] encouraged by the high efficiency of the corresponding perovskite solar cells, can partially alleviate this stability issue relying on metal oxide ETMs and high work function, stable metal anodes.

1.6 Aim of the thesis

The aim of this thesis is to develop methods and materials suitable for the applications of hybrid perovskite thin films in optoelectronic devices, such as solar cells and light-emitting diodes. Emphasis will be given to the relationship between the nature of the perovskite compounds, the processing methods, and the optoelectronic properties of the materials. In particular, the work has been structured as follows:

- Develop perovskite solar cells from flash evaporation. – A simple vacuum deposition technique is developed and applied to the fabrication of thin-film solar cells.

- Develop diodes based on metal halide perovskites that can operate as efficient solar cells and light-emitting diodes. – Dual-source evaporated perovskite films are implemented in opto-electronic devices that will be tested as solar cells and light emitting devices.

- Develop highly luminescent perovskite films. – A promising approach to reduce the non-radiative recombination in hybrid perovskites is the synthesis of nanoparticles. Here we attempt to increase the PLQY using a hybrid approach.

Each chapter will consist in a broader introduction of the topic, followed by a detailed description of the methodology used, and completed with a discussion of the experimental data.

Chapter 2.

Perovskite solar cells prepared by flash evaporation.

2.1 Introduction

As mentioned in Chapter 1, initially three dimensional perovskites were employed in dye sensitized solar cell, DSSC, in which $MAPbI_3$ and $MAPbBr_3$ were used as TiO_2 sensitizers, showing conversion efficiency higher than 3%.[54] The $MAPbI_3$ strongly absorbs in the visible region, and its calculated bandgap energy is 1.7 eV, while from optical characterization it results to be closer to 1.6 eV.[62] The energy mismatch is attributed to the presence of excitons.[63] The presence of excitons in $MAPbI_3$ is still object of debate, but many works have reported very low exciton binding energies, *e.g.* below 50 meV[64-66] (with minimum of 5 meV reported).[67] This means that at room temperature all excitons would be readily dissociated, and most photo-generated charges would be present as free carriers. In addition, it has been shown that the morphology of the perovskite strongly influences its excitonic character, which can be reduced through dedicated synthesis.[68] Together with low excitons binding energy, the high absorption coefficient of $MAPbI_3$ ($>10^5$ cm^{-1})[63] provides a high carrier generation even with very thin films (< 500 nm). These characteristics make $MAPbI_3$ highly desirable for efficient photovoltaic devices. High quality semiconducting perovskites can be easily synthesized through several methods, in the form of polycrystalline films or single crystals.[24, 69, 70] The ease of fabrication has favored the adoption of lab-scale solution processing techniques, which have yielded to the highest performing devices.[71-73] Vacuum physical deposition have also been demonstrated for the preparation of perovskite films in efficient photovoltaic applications.[34, 74] The potentially simplest method to deposit perovskite film in vacuum is the single source evaporation, in which a pre-formed perovskite is directly sublimed on the desired substrates. However, since the precursors of hybrid perovskites have largely different evaporation properties, a gradual increase of temperature would not be suitable. A more appropriate technique is flash evaporation, first developed in the late 40's for the deposition of binary alloys with very precise metallic ratio.[75, 76] Fine grains of pre-formed compounds are continually fed into a thermal heater at temperature

high enough to evaporate the least volatile component. In this way, each grain evaporates rapidly and completely, and the vapor produced closely approximates in composition that of the starting material. A variation of this method, single-source thermal ablation, has been used to deposit hybrid layered, 2D perovskites.[77-79] The material to be deposited (a pre-synthesized crystalline perovskite powder) is placed on a metal heater and brought to vacuum, and then a high current is passed through the heater causing the material to rapidly evaporate and condense onto a substrate. This technique allows to simply fabricate multi-layer structures of different organic–inorganic materials. In this chapter the first demonstration of the implementation of this technique in the preparation of photovoltaic devices is presented.

2.2 Materials and methods

Lead bromide ($PbBr_2$, > 98% Sigma Aldrich), dimethylformamide (DMF, anhydrous, 99.8 %, Sigma Aldrich), PEDOT:PSS (Clevios P VP AI4083), poly(N,N'-bis(4-butylphenyl)-N,N'-bis(phenyl)benzidine) (polyTPD, American Dye Source) (6,6)-phenyl C61-butyric acid methyl ester (PCBM, > 99%, Solenne), are commercially available and were used without further purification. Methylammonium iodide (CH_3NH_3I, MAI) was synthesized by the reaction of 30 mL of methylamine (40% in methanol, TCI) with 32.3 mL of hydroiodic acid (57 wt.% in water, Aldrich) in a 250 mL round-bottom flask at 0 °C for 2 h under stirring. The precipitate was recovered by carefully removing the solvents at 50 °C in a rotary evaporator. The yellowish raw MAI was washed three times with diethyl ether by stirring the solution for 30 min, and then finally recrystallized from a mixture of diethyl ether and ethanol. After filtration, the solid was dried at 60 °C in a vacuum oven for 24 h. A 50 wt.% perovskite precursor solution was prepared by dissolving PbI_2 and MAI in DMF, with a molar ratio PbI_2:MAI of 1:3. The perovskite solar cells were prepared as follow. 80 nm thick of PEDOT:PSS was spin-coated onto the ITO and used as the hole injection layer

(HIL). After annealing at 150 °C for 15 minutes, a 20 nm-thick polyTPD hole transport layer (HTL) was deposited on top of PEDOT:PSS from chlorobenzene (1 wt.%) and annealed at 180 °C for 30 s. The substrates were subsequently transferred to the vacuum chamber where a 200 nm thick film of $MAPbI_3$ was deposited by flash evaporation. The stack was completed by spin-coating a 80 nm-thick PCBM thin film and with the thermal vacuum deposition of a bilayer cathode composed by Ba and Ag (10 and 100 nm, respectively). EQE measurements of the solar cells were performed using a white light halogen lamp in combination with band pass filters (MiniSun simulator by ECN, the Netherlands). The device current density-voltage (J-V) characteristics were measured using a Keithley 2400 source measure unit with and without illumination. The light source was a 10500 solar simulator by Abet Technologies. Before each measurement, the exact light intensity was adjusted using a calibrated Si reference solar cell.

2.3 Discussion

The choice of the appropriate perovskite´s form (powder, crystals, film) to be placed on the tantalum heating foil is of great importance in the flash evaporation process. The sublimation occurs in few seconds through the application of a high current through the heater. The rapid heating results in a strong temperature gradient with the immediate production of gases at the contact between the perovskite and the tantalum foil. This impedes a homogeneous heat distribution through the perovskite, and may cause the above cold material to fall off the metal boat, overall hindering the formation of high quality films. Hence, it is important to have a uniform heat exchange between the tantalum foils and the perovskite to ensure a fast and continuous evaporation. It has been observed that the best control over the thickness and homogeneity of the final film can be obtained when the metal heater is coated with a perovskite layer (Fig. 10a).

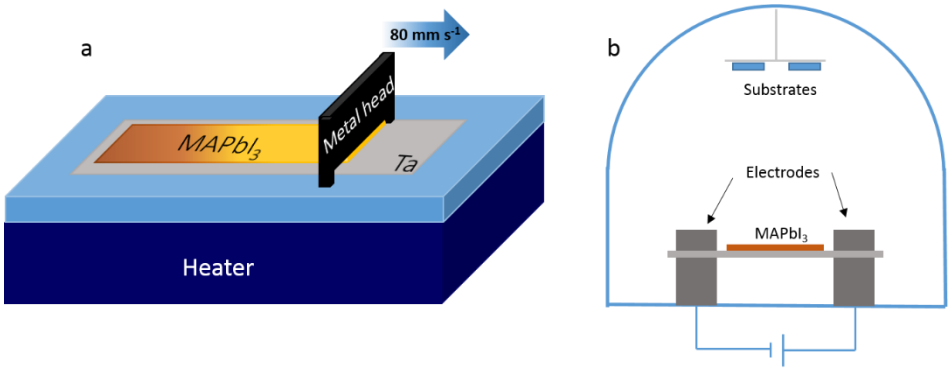

Fig. 10 *Representation of the meniscus coating process (**a**) and the evaporation chamber for the flash evaporation (**b**).*

Meniscus coating is a suitable technique for this purpose, since it allows to deposit thick and homogeneous films with only a small volume of perovskite precursor. For the coating, the tantalum foil (dimensions 70 x 15 x 0.05 mm) was fixed to the base plate, and 80 µL of $MAPbI_3$ precursor solution were placed in between the tantalum foil and a thin flat metal block using capillary effect to pin the solution in place. The distance between the metal block on the tantalum foil was 1.15 mm. By displacing the metal block (coating-head) at a speed of 80 mm s^{-1}, the solution is uniformly spread on the metal, immediately forming a dark and compact perovskite layer. This is possible because during the deposition the tantalum foil is heated at 80 °C. Once the perovskite film is formed (i.e. the layer changes its color from yellow to dark brown), it was further annealed at 125 °C for 5 minutes in order to remove the excess solvent. The perovskite-coated tantalum foil was subsequently clamped in between two electrodes connected to a high current source in a high vacuum chamber (Fig. 10b). After positioning the substrates on the dedicate holders mounted at a vertical distance of 10 cm from the evaporation source, the evaporation chamber was evacuated to a pressure of 10^{-4} mbar. Then, a large current (approximately 90 A) is passed through the tantalum foil, causing the instantaneous evaporation of the $MAPbI_3$ that condensates on the desired substrate. During the heating process the chamber is isolated from the vacuum pump. The final film thickness is directly proportional to the amount of perovskite initially deposited on the metal heater (250 nm in

these conditions, Fig. 11a). The layers formed with this process are characterized by a uniform and homogenous surface, as revealed by atomic force microscopy (AFM, Fig. 11b). The film presents a flat surface with a root mean square (RMS) roughness of 17.6 nm, calculated over an area of 25 μm^2. The X-ray diffraction of the evaporated film confirms the presence of the tetragonal $MAPbI_3$ phase, characterized by the signals at 14.1°, 28.4° and 31.8° (Fig. 11c). Also the optical absorption (Fig. 11d) of the evaporated films presents the expected features of $MAPbI_3$, with a steep absorption onset starting at 760-800 nm, consistent with the material band gap (about 1.6 eV).

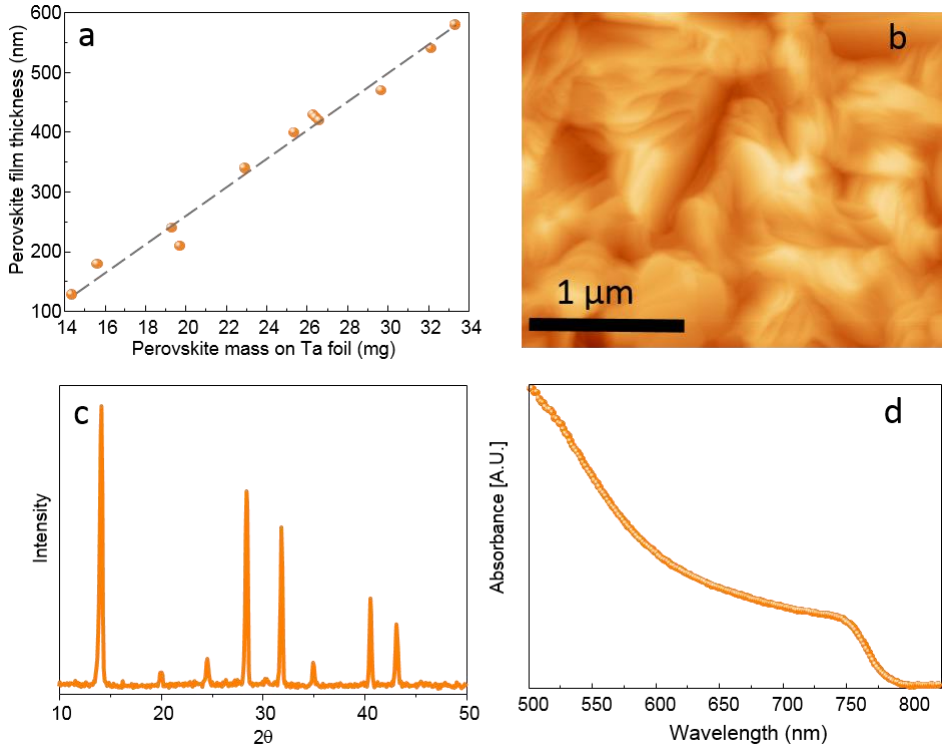

Fig. 11 a) *Correlation between Ta foil loading and evaporated film thickness.* ***b)*** *AFM,* ***c)*** *XRD and* ***d)*** *absorption of flash evaporated MAPI film.*

These results demonstrate how flash evaporation allows the formation of highly crystalline perovskite films, with a uniform and smooth surface which is strongly desirable for the preparation of thin films solar cells. After optimization of the perovskite flash deposition, photovoltaic devices were prepared as described in

the experimental section. $MAPbI_3$ was deposited on top of polyTPD, which selectively extract holes to the ITO contact. The devices were finished with PCBM and Ba/Ag, and were tested in an inert environment under 1 sun illumination. The characterization is reported in Fig. 12.

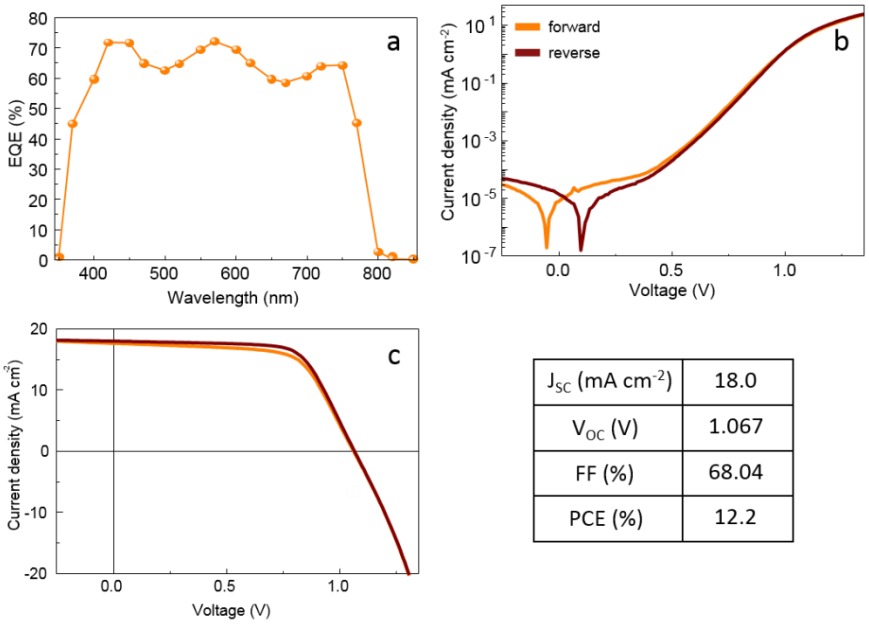

J_{SC} (mA cm^{-2})	18.0
V_{OC} (V)	1.067
FF (%)	68.04
PCE (%)	12.2

Fig. 12 a) *Photovoltaic external quantum efficiency,* ***b)*** *current density versus voltage in the dark and* ***c)*** *current density versus voltage under illumination of the flash evaporated perovskite solar cell. The table reports the figure of merit of the solar cell.*

The external quantum efficiency spectrum represents the fraction of the extracted charges over the incident photons at different wavelengths. In these devices it shows a sharp increase at 800 nm (Fig. 12a), in good agreement with the absorption onset observed in the absorbance spectrum. As the $MAPbI_3$ strongly absorbs in the visible spectrum, the corresponding EQE is as high as 73% (at 570 nm and 420 nm). In Fig. 12a the dark J-V characteristics of the cell is reported. The device shows good diode behavior, with low leakage current which confirms the good quality of the flash evaporated perovskite films. A small hysteresis in the J-V curve, which is likely to be due to a charge accumulation at one of the two contact interfaces, can be observed. Under illumination, the hysteresis is

again very limited, as commonly observed in vacuum deposited perovskite solar cells. The short circuit current density is high, especially considering the rather thin perovskite absorber (200 nm). The high open circuit voltage is also indicative of very low recombination within the device. The fill factor reflects a good charge extraction in the solar cell, leading to a remarkable power conversion efficiency of 12.2%.

2.4 Conclusions

In this chapter the preparation of efficient perovskites solar cells by flash evaporation has been reported. The development of a suitable protocol to apply the perovskite material on the metal heater is of great importance for the preparation of homogenous and compact perovskite films, a requirement for the fabrication of thin film devices. Meniscus coating of the tantalum foil provides uniform perovskite layers that are fully transferred on the substrates by application of high current. The perovskite solar cells prepared by this technique show good photovoltaic performances. The possibility to deposit the perovskite on every surface allowed the use of an electron blocking layer able to reduce the charge recombination, increasing the power conversion efficiency. This perovskite deposition method and its application to perovskite photovoltaics has been recently patented.

ChemComm

COMMUNICATION

View Article Online
View Journal | View Issue

Cite this: *Chem. Commun.*, 2015, 51, 7376

Received 5th February 2015,
Accepted 24th March 2015

DOI: 10.1039/c5cc01103e

www.rsc.org/chemcomm

Perovskite solar cells prepared by flash evaporation

Giulia Longo, Lidón Gil-Escrig, Maarten J. Degen, Michele Sessolo and Henk J. Bolink*

A simple vacuum deposition method for the preparation of high quality hybrid organic–inorganic methylammonium lead iodide perovskite thin films is reported. When sandwiched in between organic charge transporting layers, such films lead to solar cells with a power conversion efficiency of 12.2%.

Organic–inorganic (hybrid) halide perovskites consisting of aliphatic or aromatic ammonium cations and divalent metals have been the focus of several studies due to their interesting optoelectronic properties, high charge mobility and ease of deposition even through solution-based methods.[1,2] More recently, three dimensional hybrid perovskites have been successfully employed as light harvesters in thin film solar cells.[3,4] Thanks to a large scientific effort by a number of research groups, the device performance has seen a spectacular rise and, in only five years, a record power conversion efficiency (PCE) as high as 20.1% has been reported.[5–14] Early studies focused mainly on the optimization of the solar cell architecture through interface engineering, *i.e.* choice of proper hole transport materials (HTMs),[4,9,15,16] and electron transport materials (ETMs).[3,8,12,17,18] Most recent investigations, however, have demonstrated that the control over the perovskite crystallization plays a main role in the achievement of high PCE devices.[19,20] Homogeneous perovskite films with large crystal size are desirable since they would allow to increase the layer thickness, thus increasing the sunlight absorption, without hindering the charge transport and collection. Many different strategies have been proposed so far for the solution-processing of hybrid perovskites.[21–26] Besides the deeper understanding on the structure–properties relation in methylammonium lead halide perovskite cells, these studies also highlighted the complexity and interplay of parameters involved in the solution deposition of such materials. Taking into account that perovskite solar cells are potential candidate for complementing silicon or copper indium gallium selenide (CIGS) cells in tandem devices, the development of a reliable and thin-film compatible deposition technique is a primary task. Within this perspective, dual source vapour deposition has been proposed as an attractive alternative in the preparation of $CH_3NH_3PbI_3$ thin films for photovoltaics.[7,12] Perovskites layers were obtained by simultaneous controlled co-evaporation of the lead halide (either $PbCl_2$ or PbI_2) and the methylammonium iodide CH_3NH_3I (MAI) in high vacuum chambers. Such vapour-deposited films are very flat and homogeneous and, when employed in solar cells architecture, lead to PCEs as high as 16.5%.[27] Co-evaporation enables a fine control over the stoichiometry and thickness of the perovskite films, and takes advantage of the intrinsic high purity of sublimated compounds. Moreover, the technique allows for the preparation of multi-layer stacks, and is fully compatible with standard semiconductor processing. On the other side, the process is relatively time-consuming and it requires accurate periodical calibrations to properly control the deposition rate and precursors ratio. An alternative physical method for the deposition of compound semiconductors is flash evaporation.[28,29] The material to be deposited is placed on a metal heater and brought to vacuum, and then a large current is passed through the heater causing the material to rapidly evaporate and condense onto a substrate. Layered, 2D perovskite metal halide doped with aliphatic or aromatic ammonium cations were deposited with this method, resulting in optically active, polycrystalline thin films.[30] The desired hybrid film is formed at temperatures high enough for the inorganic compound to evaporate, without causing the decomposition of the organic component.[31]

In this communication, we report the flash evaporation of 3D organic–inorganic hybrid perovskites and their use in efficient, planar photovoltaic devices. We show that uniform and smooth polycrystalline $CH_3NH_3PbI_3$ thin films of the desired thickness can be obtained by careful tuning of the deposition parameters. The as-deposited material was characterized by optical and morphological methods, revealing a high

Instituto de Ciencia Molecular, Universidad de Valencia, c/Catedrático J. Beltrán, 2, 46980 Paterna, Spain. E-mail: henk.bolink@uv.es; Fax: +34-963543273; Tel: +34-963544416

degree of homogeneity as well as a low surface roughness, which is desirable for its implementation into optoelectronic devices. The photovoltaic properties of flash evaporated $CH_3NH_3PbI_3$ thin films were evaluated in planar heterojunction solar cells employing organic charge transport layers. High PCE up to 12% were obtained, demonstrating the potential of flash evaporation as an alternative method for the production of efficient perovskite solar cells. While the flash evaporation technique allows for the deposition of hybrid perovskite films even from their powders as the precursor, we found that a better control over the thickness and homogeneity of the final layer is obtained if the metal heater is coated with the material to be deposited.

The MAI was synthetized according to a previously published method[32] and dried at 60 °C in vacuum for 24 hours. A 50 wt% perovskite precursor solution is prepared by dissolving PbI_2 (Sigma Aldrich) and MAI in DMF, with a molar ratio PbI_2 : MAI of about 1 : 3. The solution is subsequently deposited onto the metal heater (a tantalum foil of 70 × 15 × 0.05 mm) by meniscus coating (Fig. 1a).[33] The layer is created by placing 80 µl of precursor solution under the metal blade (1.2 mm high) and by spreading it over the tantalum foil at a speed of 80 mm s^{-1}. During deposition the foil is heated at 80 °C and once the perovskite layer forms (*i.e.* the layer turns from yellow to dark brown, Fig. 1b), it is heated at 125 °C for 5 minutes in order to remove the excess solvent. The tantalum foil is subsequently transferred into a high vacuum chamber and clamped in between two electrodes connected to a high current source (Fig. 1c). The substrates to be coated are placed on a sample holder mounted at a vertical distance of 10 cm from the evaporation source. After establishing a stationary vacuum of approximately 0.1 mbar, a large current (approximately 30 A) is passed through the tantalum foil, causing the complete and virtually instantaneous evaporation of the $CH_3NH_3PbI_3$. The resulting film thickness is controlled by the amount of perovskite initially deposited on the metal heater. The grazing incident X-ray diffraction (GIXRD) pattern of an as-deposited 200 nm thick film is reported in Fig. 2a. The spectrum suggests a high degree of crystallinity, with the peaks at 14.1°, 28.4° and 31.8° confirming the formation of the tetragonal structure of the $MAPbI_3$ perovskite. The surface topography of the film was also investigated by atomic force microscopy (AFM, Fig. 2b). The film shows homogenous aggregation and is relatively flat, with a root mean square (RMS) roughness, calculated over an area of 25 μm^2, of 17.6 nm. These data demonstrate that a 3D hybrid organic–inorganic perovskite can be evaporated and reassembled onto a desired substrate with a high degree of crystallinity and homogeneous morphology. These characteristics are of particular interest for optoelectronic applications such as thin film photovoltaic devices. Single junction solar cell were prepared by integration of the perovskite films in a multilayer stack of organic semiconducting layers. Indium tin oxide (ITO) coated glass slides were used as bottom transparent electrode.

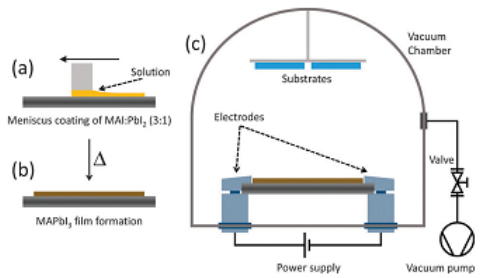

Fig. 1 Process flow for the deposition of hybrid organic–inorganic perovskite thin films *via* flash evaporation. (a) The precursor solution is spread onto a tantalum foil *via* meniscus coating and (b) annealed to obtain a polycrystalline $CH_3NH_3PbI_3$ film. The coated tantalum sheet is then transferred to a vacuum chamber (c) where the hybrid perovskite is evaporated onto the desired substrate.

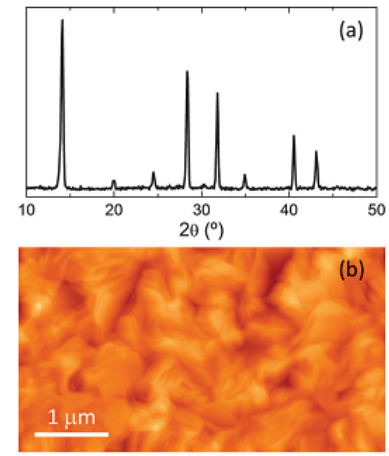

Fig. 2 (a) GIXRD pattern and (b) AFM topography of a $CH_3NH_3PbI_3$ thin film deposited by flash evaporation.

An 80 nm thick of poly(3,4-ethylenedioxythiophene) doped with poly(styrenesulfonate) (PEDOT:PSS, Heraeus Clevios™ P VP AI 4083) was spin-coated onto the ITO and used as the hole injection layer (HIL). After annealing it at 150 °C for 15 minutes, a 20 nm thick poly(*N*,*N*′-bis(4-butylphenyl)-*N*,*N*′-bis(phenyl)benzidine) (polyTPD) HTL was deposited on top from chlorobenzene (1 wt%) and annealed at 180 °C for 30 s. The polymer stack was subsequently transferred to the vacuum chamber and a 200 nm thick film of $MAPbI_3$ perovskite was deposited by flash evaporation. The stack was completed by spin-coating an 80 nm thick (6,6)-phenyl C_{61}-butyric acid methyl ester (PCBM) thin film and with the thermal vacuum deposition of a bilayer cathode composed of Ba and Ag (10 and 100 nm, respectively). The device characterization was performed in a nitrogen glove box, using a mini-sun simulator designed by ECN and calibrated with a Si reference cell. The device EQE as well as the perovskite

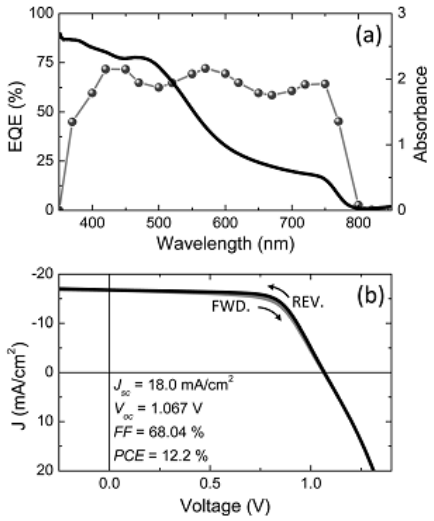

Fig. 3 (a) EQE (symbols) and optical absorption (line) in the UV-visible region for a planar perovskite solar cell and its active layer, respectively, deposited by flash evaporation. (b) *J*–*V* curve in forward (FWD.) and reverse (REV.) bias for a device under illumination with the structure ITO/PEDOT:PSS/polyTPD/$MAPbI_3$/PCBM/Ba/Ag. The scan rate in both bias direction was 0.1 V s^{-1}.

film UV-visible absorption spectrum are reported in Fig. 3a. The optical absorption shows the typical profile of the $MAPbI_3$ perovskite, with a broad absorption over the whole visible spectrum and onset at about 800 nm, corresponding to an optical band gap of 1.55 eV. The EQE rises at the same wavelength, reaching a maximum value of 73% in the green (570 nm) and in the blue (420–450 nm) region of the spectrum. The current density–voltage (*J*–*V*) characteristic of the solar cell is reported in Fig. 3b. The *J*–*V* curve is almost independent on the scan direction, in contrary to what often observed for solution-processed perovskite devices. The short-circuit current density (J_{SC}), open-circuit voltage (V_{OC}) and fill factor (FF) for a typical device, are 18.0 mA cm^{-2}, 1.07 V and 68%, respectively, leading to a remarkable power conversion efficiency of 12.2%. This result is of great importance for the future development of photovoltaic devices based on hybrid organic–inorganic perovskite materials, especially in view of their integration with existing thin film photovoltaic technologies. The deposition process is scalable, additive and extremely fast (in the order of few seconds), which is desirable for the implementation of this materials in industrial applications.

In summary, 3D methylammonium lead iodide perovskites have been prepared by flash evaporation. Homogeneous and highly crystalline thin films can be obtained with unique control over the material composition and film thickness. The as-deposited films have been tested in planar solar cells employing organic charge transport layers, demonstrating power conversion efficiencies exceeding 12%. This method allows for a straight-forward preparation of multi-layer structures of different organic–inorganic materials, which are foreseen as the big challenge in hybrid perovskite devices. Moreover, the simplicity of the process is particularly suited for the preparation of tandem solar cells, where the perovskite device could be used as a top transparent device in silicon or CIGS photovoltaic modules.

Notes and references

1 C. R. Kagan, D. B. Mitzi and C. D. Dimitrakopoulos, *Science*, 1999, **286**, 945–947.
2 D. B. Mitzi, C. A. Feild, W. T. A. Harrison and A. M. Guloy, *Nature*, 1994, **369**, 467–469.
3 A. Kojima, K. Teshima, Y. Shirai and T. Miyasaka, *J. Am. Chem. Soc.*, 2009, **131**, 6050–6051.
4 M. M. Lee, J. Teuscher, T. Miyasaka, T. N. Murakami and H. J. Snaith, *Science*, 2012, **338**, 643–647.
5 H. J. Snaith, *J. Phys. Chem. Lett.*, 2013, **4**, 3623–3630.
6 N. G. Park, *J. Phys. Chem. Lett.*, 2013, **4**, 2423–2429.
7 M. Liu, M. B. Johnston and H. J. Snaith, *Nature*, 2013, **501**, 395–398.
8 H. Zhou, Q. Chen, G. Li, S. Luo, T. B. Song, H. S. Duan, Z. Hong, J. You, Y. Liu and Y. Yang, *Science*, 2014, **345**, 542–546.
9 P. Gao, M. Grätzel and M. K. Nazeeruddin, *Energy Environ. Sci.*, 2014, **7**, 2448–2463.
10 S. Kazim, M. K. Nazeeruddin, M. Grätzel and S. Ahmad, *Angew. Chem., Int. Ed.*, 2014, **53**, 2812–2824.
11 P. P. Boix, K. Nonomura, N. Mathews and S. G. Mhaisalkar, *Mater. Today*, 2014, **17**, 16–23.
12 O. Malinkiewicz, A. Yella, Y. H. Lee, G. M. Espallargas, M. Graetzel, M. K. Nazeeruddin and H. J. Bolink, *Nat. Photonics*, 2014, **8**, 128–132.
13 M. Gratzel, *Nat. Mater.*, 2014, **13**, 838–842.
14 M. A. Green, K. Emery, Y. Hishikawa, W. Warta and E. D. Dunlop, *Prog. Photovolt.: Res. Appl.*, 2015, **23**, 1–9.
15 P. Qin, S. Tanaka, S. Ito, N. Tetreault, K. Manabe, H. Nishino, M. K. Nazeeruddin and M. Grätzel, *Nat. Commun.*, 2014, **5**, 3834.
16 J. Y. Jeng, K. C. Chen, T. Y. Chiang, P. Y. Lin, T. D. Tsai, Y. C. Chang, T. F. Guo, P. Chen, T. C. Wen and Y. J. Hsu, *Adv. Mater.*, 2014, **26**, 4107–4113.
17 A. Mei, X. Li, L. Liu, Z. Ku, T. Liu, Y. Rong, M. Xu, M. Hu, J. Chen, Y. Yang, M. Grätzel and H. Han, *Science*, 2014, **345**, 295–298.
18 J. Y. Jeng, Y. F. Chiang, M. H. Lee, S. R. Peng, T. F. Guo, P. Chen and T. C. Wen, *Adv. Mater.*, 2013, **25**, 3727–3732.
19 W. Nie, H. Tsai, R. Asadpour, J.-C. Blancon, A. J. Neukirch, G. Gupta, J. J. Crochet, M. Chhowalla, S. Tretiak, M. A. Alam, H.-L. Wang and A. D. Mohite, *Science*, 2015, **347**, 522–525.
20 D. Shi, V. Adinolfi, R. Comin, M. Yuan, E. Alarousu, A. Buin, Y. Chen, S. Hoogland, A. Rothenberger, K. Katsiev, Y. Losovyj, X. Zhang, P. A. Dowben, O. F. Mohammed, E. H. Sargent and O. M. Bakr, *Science*, 2015, **347**, 519–522.
21 J. Burschka, N. Pellet, S. J. Moon, R. Humphry-Baker, P. Gao, M. K. Nazeeruddin and M. Grätzel, *Nature*, 2013, **499**, 316–319.
22 Q. Chen, H. Zhou, Z. Hong, S. Luo, H. S. Duan, H. H. Wang, Y. Liu, G. Li and Y. Yang, *J. Am. Chem. Soc.*, 2014, **136**, 622–625.
23 A. Dualeh, N. Tétreault, T. Moehl, P. Gao, M. K. Nazeeruddin and M. Grätzel, *Adv. Funct. Mater.*, 2014, **24**, 3250–3258.
24 G. E. Eperon, V. M. Burlakov, P. Docampo, A. Goriely and H. J. Snaith, *Adv. Funct. Mater.*, 2014, **24**, 151–157.
25 Z. Xiao, Q. Dong, C. Bi, Y. Shao, Y. Yuan and J. Huang, *Adv. Mater.*, 2014, **26**, 6503–6509.
26 N. J. Jeon, J. H. Noh, Y. C. Kim, W. S. Yang, S. Ryu and S. I. Seok, *Nat. Mater.*, 2014, **13**, 897–903.
27 Q. Lin, A. Armin, R. C. R. Nagiri, P. L. Burn and P. Meredith, *Nat. Photonics*, 2015, **9**, 106–112.
28 L. Harris and B. M. Siegel, *J. Appl. Phys.*, 1948, **19**, 739–741.
29 J. L. Richards, P. B. Hart and L. M. Gallone, *J. Appl. Phys.*, 1963, **34**, 3418–3420.
30 D. B. Mitzi, M. T. Prikas and K. Chondroudis, *Chem. Mater.*, 1999, **11**, 542–544.
31 K. Chondroudis, D. B. Mitzi and P. Brock, *Chem. Mater.*, 1999, **12**, 169–175.
32 L. Etgar, P. Gao, Z. Xue, Q. Peng, A. K. Chandiran, B. Liu, M. K. Nazeeruddin and M. Grätzel, *J. Am. Chem. Soc.*, 2012, **134**, 17396–17399.
33 C. S. Herrick, *Ind. Eng. Chem. Prod. Res. Dev.*, 1980, **19**, 314–316.

Chapter 3.

Efficient photovoltaic and electroluminescent perovskite devices.

3.1 Introduction

Solar cells and light-emitting diodes are complementary devices, transforming photons into electrons or vice versa. Importantly, the electronic transitions that control the radiative recombination are also responsible for the absorption process. At short circuit, the driving force for charge separation is high allowing most of the photo-generated charges to escape the absorber layer and flow into the external circuit. On the other hand, at open circuit voltage no current can flow, implying that all the generated carriers must eventually recombine. Hence the best solar cell should operate in the radiative limit, where the absorbed photon flux equals the emitted flux, under open circuit conditions.[80] In other words, the radiative recombination, which involves energy states related to the absorption, should be the only recombination process occurring in the device, since non-radiative recombination paths would reduce the V_{OC} and limit the solar cell efficiency. This optical reciprocity has been shown to apply for many photovoltaic systems (inorganic solar cells,[81] dye sensitized solar cells,[82] organic solar cells[83]) and including perovskites.[84, 85] The reciprocity relation allows to predict the photo-voltage by measuring the external quantum efficiency for EL (EQE_{EL}), which is therefore an additional figure of merit to evaluate the performance of perovskite solar cells. In addition, the development of devices that can act both as solar cells and light-emitting diodes would be appealing for the design of innovative technologies, like smart windows behaving as energy converters during the day and as light-emitting sources during the night. In this chapter, a $MAPbI_3$ solar cell will be characterized as a LED, simply by monitoring the current density and electroluminescence intensity in forward bias. In light-emitting devices, the current driving method can exhibit a big influence over the electroluminescence efficiency.[86] Usually organic light-emitting diodes are characterized by the application of a voltage (or a constant current), and by measuring the electroluminescence intensity. However, the application of high currents can damage the emitting materials, reducing the overall efficiency. A possible solution is the use of a pulsed driving mode. This driving method

combines the application of very high currents in the "ON" part of the pulse with a release of the heat excess during the "OFF" part of the pulse. Hence it allows to increase the current density and hence the electroluminescence intensity without damaging the active layer.

In this chapter a multifunctional device showing both efficient photovoltaic performance and good electroluminescence is presented. The active layer consists of a perovskite film prepared by dual source vacuum deposition, and both continuous and pulsed driving modes will be employed for the evaluation of the electroluminescence.

3.2 Materials and methods

Lead iodide (PbI_2, > 98% Sigma Aldrich), methylammonium iodide (Dyesol), PEDOT:PSS (Clevios P VP AI4083), poly(N,N'-bis(4-butylphenyl)-N,N'-bis(phenyl)benzidine) (polyTPD, American Dye Source) (6,6)-phenyl C61-butyric acid methyl ester (PCBM, > 99%, Solenne), are commercially available products and were used without further purification. PEDOT:PSS was spin coated on top of clean ITO substrates resulting in a 80 nm thick layer, annealed at 120 °C for 15 minutes. On top of this layer a thin film of polyTPD was deposited from a chlorobenzene solution using a meniscus coater at a coating speed of 2.5 mm s^{-1}. Subsequently the substrates were transferred to a vacuum chamber integrated into a nitrogen filled glovebox and evacuated to a pressure of 1×10^{-6} mbar. Temperature controlled evaporation sources filled with ceramic crucibles were employed to sublime the CH_3NH_3I and the PbI_2. Co-evaporation of the methylammonium and lead iodides was performed heating the crucibles at 90 °C and 250 °C, respectively. The thickness of the perovskite film was monitored using a quartz sensor in the vicinity of the substrate holder. The chlorobenzene solution of PCBM was meniscus coated on top of the perovskite film at a coating speed of 10 mm s^{-1} in ambient conditions. The device was completed by the thermal evaporation of the top metal electrode (10 nm Ba

followed by 100 nm Ag) under a base pressure of 2×10^{-6} mbar. The thickness of the films was determined with an Ambios XP-1 profilometer. The devices were then encapsulated with a glass coverslip using a UV-curable epoxy sealant (Ossila E131 Encapsulation Epoxy), with 5 minutes of UV exposure. GIXRD measurements were performed at room temperature in the 2θ range 5–50° on an Empyrean PAN-analytical powder diffractometer, using Cu Kα1 radiation. Pawley refinements were performed using the TOPAS software and revealed an excellent fit to a one-phase model with a tetragonal cell (a = 8.80(2) Å, c = 12.57(2) Å) and space group I4/mcm. Simulation of the crystal structure of $CH_3NH_3PbI_3$ perovskite was performed using as starting model the isostructural Sn analogue (CCDC ref. code: ZZZBWS02) modifying the cell parameters to those obtained in the Pawley refinement. Characterization of the photovoltaic performance was obtained using two methods. EQE measurements were performed using a white light halogen lamp in combination with bandpass filters (MiniSun simulator by ECN, the Netherlands). Current density-voltage (J-V) characteristics were measured using a Keithley 2400 source measure unit with and without illumination. The light source was a 10500 solar simulator by Abet Technologies. Before each measurement, the light intensity was adjusted using a calibrated Si solar cell. Current density and electroluminescence were measured by using a Keithley 2400 source meter and a photodiode coupled to the Keithley 6485 pico-amperometer calibrated. The irradiance and EQE were determined using an integrated sphere coupled to an UDT instruments S370 Optometer. An Avantes luminance spectrometer was used to measure the electroluminescent spectrum. The pulsed current driving was controlled using a Test System designed by BoTEST (Botest OLT OLED Lifetime-Test System). Transient luminance signals were obtained by applying a pulsed current and measuring the photocurrent generated by a photometry-precision Si-photodiode (Hamamatsu ST3368BK) coupled to a four channel Tektronix Oscilloscope (TDS2024B).

3.3 Discussion

In order to design a solar cell that can also behave as a light-emitting diode, some modifications to the device architecture should be performed. In Chapter 1 the p-i-n planar solar cell structure was presented. The front contact is composed by an ITO transparent electrode coated with a hole injection layer (PEDOT:PSS), while the top electron transport material is a fullerene derivative capped with a high work-function metal. The latter interface, however, is characterized by a large energy barrier between the Au work function and the LUMO of the fullerene, hindering an efficient electron injection in the diode. For this reason, a low work function cathode formed by a thin layer of barium capped with silver is used in this work, ensuring both good extraction and injection of electrons. In addition, an electron blocking layer (polyTPD) was added to the structure, in order to confine the electrons in the perovskite layers increasing the electroluminescence efficiency. Meniscus coating was employed to deposit the polyTPD and the PCBM layer to ensure high quality pin-hole free films.[87] The device architecture and the flat band energy diagram are presented in Fig. 13.

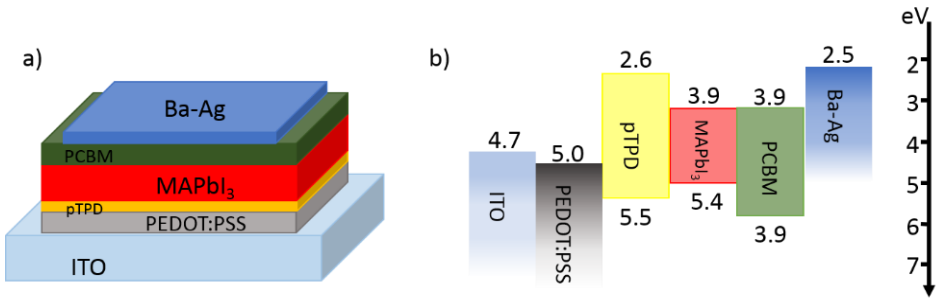

Fig. 13 a) *Schematic representation of the device architecture and of* ***b)*** *the flat band energy diagram of the materials employed in the device.*

In order to analyze the crystallinity and the optical features of the evaporated perovskite, thin films (with the same thickness as employed in the solar cell, 320 nm) were deposited on glass. In Fig. 14 the X-ray diffractogram and the absorption spectrum of the film are reported.

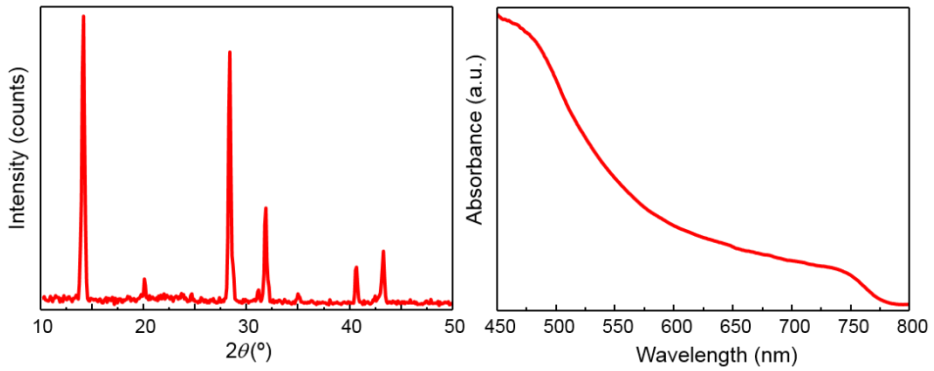

Fig. 14 *X-Ray diffraction pattern (left) and absorption spectrum (right) of the evaporated $MAPbI_3$ films.*

The obtained diffraction pattern reveals a tetragonal structure and space group I4/mcm. The characteristic peaks of $MAPbI_3$ positioned at 14.2°, 28.4° and 31.9° are clearly discernable in the diffractogram, and no signals from PbI_2 (especially the peak at 12.7°) are visible, confirming the high crystallinity and the full conversion to the perovskite phase obtained by dual-source evaporation. The Scherrer equation revealed an average crystal size of 35 nm, in accordance with other $MAPbI_3$ films prepared with the same technique.[37] The rather sharp absorption onset positioned at 760 nm, also confirms the $MAPbI_3$ formation. The lack of excitonic features in the absorption is due to the small size of the crystal grains, as described by Grancini *et al.*,[20, 64] in agreement with the crystallites average size estimated by the diffraction pattern.

The device will be operated both as solar cells and as light-emitting diodes. First the photovoltaic performance will be discussed.

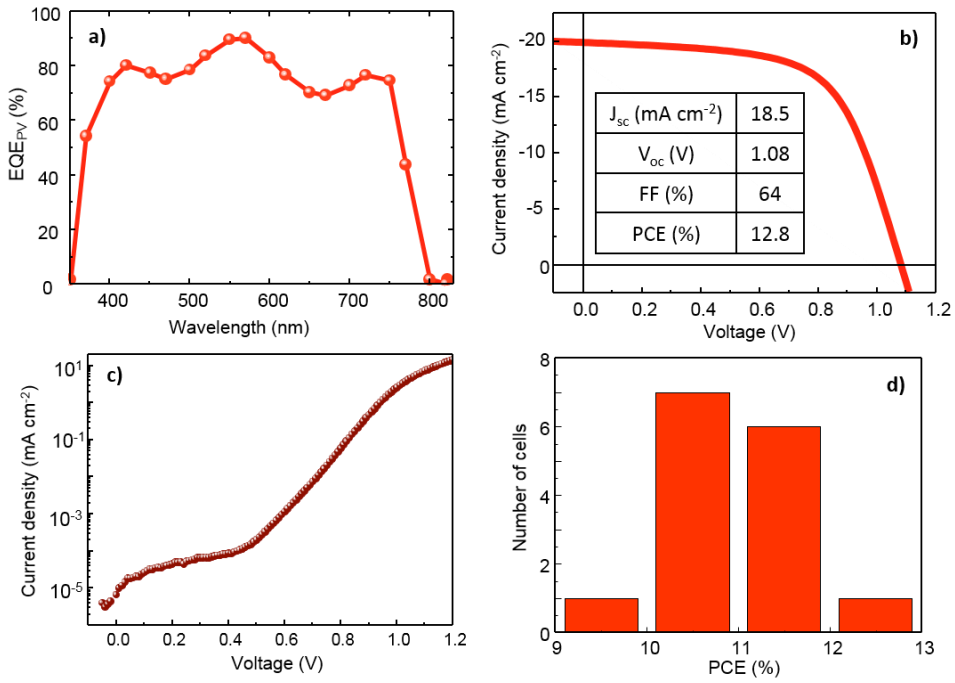

Fig. 15 a) *Photovoltaic external quantum efficiency and b) current density versus voltage of the solar cell under illumination. In the inset, the figures of merits are reported.* ***c)*** *Current density versus voltage of the device in the dark.* ***d)*** *Statistics of the power conversion efficiency for different solar cells.*

The external quantum efficiency (Fig. 15a) is high in the visible region of the spectrum, reaching a maximum of 90% at 570 nm. The current density-voltage characteristics under 1 sun illumination revealed high short circuit current density and open circuit voltage, indicating that the majority of the charge carriers recombine radiatively. The best performing cell presents a short circuit current of 18.5 mA cm^{-2}, an open circuit voltage of 1.08 V and a high fill factor (characteristic of the evaporated perovskite solar cells), resulting in a power conversion efficiency of 12.8 %. The spread of the performances over several cells (Fig. 15d) is narrow, confirming the reliability of the device stack used here. The good quality of the diode is also confirmed by the dark J-V curve (Fig. 15c), which presents low leakage current and well defined diode working regimes.

Following the photovoltaic characterization, the same device configuration was tested as a light-emitting diode. Under the application of a forward voltage bias

beyond the build-in potential, the current density passing through the device and the electroluminescence (irradiance) of the perovskite was registered. In Fig 16 the corresponding measurements are presented.

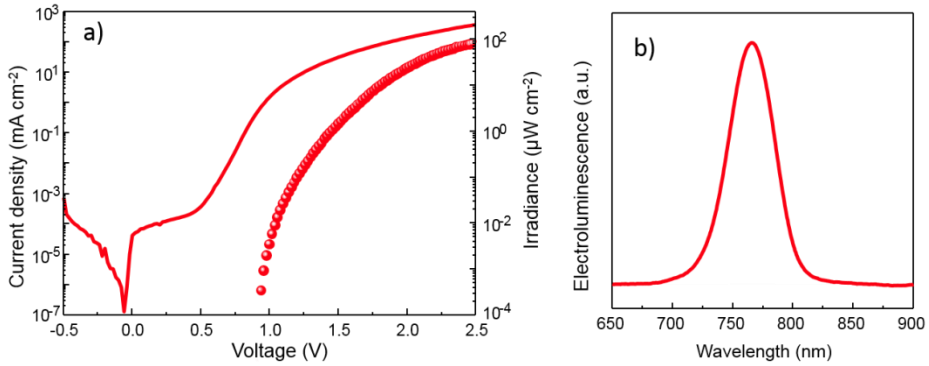

Fig. 16 a) *Current density (solid line) and irradiance (symbols) versus applied bias for the perovskite diode.* ***b)*** *Electroluminescence spectrum of the same device.*

The current density-voltage scan shows the classical diode behavior, characterized by a very low leakage current (index of the high quality film without large defects or pinholes). The current starts to rise due to charge diffusion, until charges are injected and drift current dominates. As the carrier injection begins, the irradiance of the devices rapidly rises reaching 84 μW cm^{-2} at 2.5 V, with the electroluminescence spectrum centered at 765 nm, in agreement with the perovskite bandgap. Even if intense electroluminescence is obtained at the low applied voltage, which is indicative of the good charge transport through the device, the maximum EQE_{EL} is 0.014 %, in agreement with previous results[80] but consistently lower compared to other infrared LEDs.[88, 89] Unlike in many OLEDs, the EQE_{EL} of perovskite LEDs is directly proportional to the current density. A similar behavior was observed for the photoluminescence quantum yield of perovskites at increasing excitation intensity.[90] This phenomenon can be explained with the filling of the traps (otherwise quenching the radiative recombination) as the excitation intensity is increased. A similar behavior was observed for the $MAPbI_3$ films presented in this work, which do not show any photoluminescence signal when excited with a low intensity source.

Photoluminescence signals could only be detected from these films when they were excited by a continuous wave laser. This suggests that the presence of trap states could also limit the electroluminescence output. While measuring at high current density might result in a further increase of the EQE_{EL}, it can also be detrimental for the devices, due to the generated heat that can damage $MAPbI_3$. As mentioned before, an alternative that allows the application of high currents without heating up the diode is the use of a pulsed driving mode. In this work a periodic squared waveform was used, with duty cycles of 50% and frequency of 100 Hz, corresponding to a current pulse of 5 ms alternated with equivalent off cycles that permit the release of the generated heat to the substrate that operates as a heat sink (Fig. 17a). The irradiance was measured in an integrated sphere with a Si-photodiode coupled to an oscilloscope. The irradiance (Fig. 17b) was estimated integrating the emitted photons over a period of 100 ms. Up to a current density of 375 mA cm^{-2} the devices were operated in DC, beyond that the current was applied as a squared waveform.

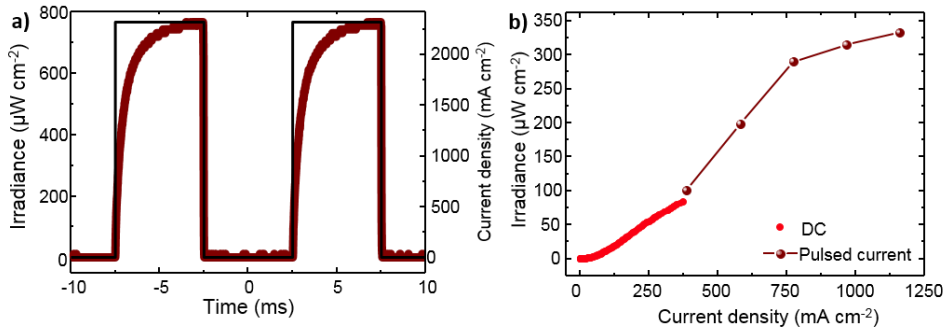

Fig. 17 a) *Detail of the luminance (red curve) and the current density (black curve) when the device is operating in pulsed driving mode.* ***b)*** *Irradiance versus current density for a dc- and pulsed current driving mode.*

Average current densities up to 1150 mA cm^{-2}, (corresponding to 2300 mA cm^{-2} in the peak) were applied, obtaining average irradiance up to 330 μW cm^{-2}. This maximum average value corresponds to a peak irradiance of 770 μW cm^{-2}, with a rising time of approximatively 4 ms, as depicted in Fig. 17a.

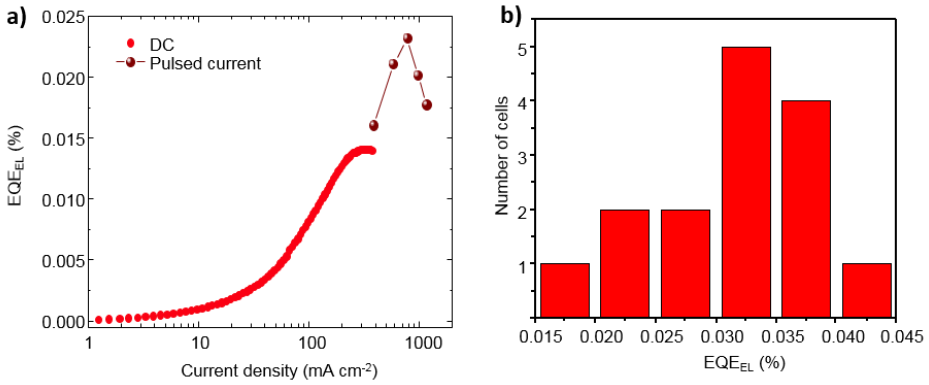

Fig. 18 a) *External quantum efficiency versus current densities for DC- and pulsed driving mode.* ***b)*** *Distribution of the electroluminescence quantum efficiency of the different cells*

Importantly, the average EQE_{EL} calculated over several devices is 0.03%, twice as high than the efficiency obtained in DC driving mode. This result confirms that the dependence of the radiative efficiency on the excitation density is an intrinsic property of $MAPbI_3$, since it can be observed bot in photo- and electroluminescence. It also implies that the design rules adopted in OLEDs must be modified taking into account the non-excitonic character of luminescence in these materials.

3.4 Conclusions

In conclusion it has been shown that perovskites, traditionally applied to photovoltaics, have also potential as light-emitting materials. The electroluminescence of the $MAPbI_3$ was clearly observed at moderate applied bias, and it increased for increasing current densities. This behavior is opposite compared to what observed for OLEDs, due to the different photophysics of perovskites and organic emitters. In OLEDs the emission is governed by exciton recombination, which is reduced at high current densities due to exciton-exciton annihilation. Whereas in the here studied perovskites emission occurs by free carrier recombination in a direct band-to-band process. In this situation a high current density results in trap filling with the consequent enhancement of the

electroluminescence. In this chapter has been showed how, if a pulsed current driving mode is used, higher currents can be applied without degrading the active material, leading to a substantial increase of the external quantum efficiency.

ChemComm

COMMUNICATION

View Article Online
View Journal | View Issue

Cite this: *Chem. Commun.*, 2015, 51, 569

Received 23rd September 2014,
Accepted 11th November 2014

DOI: 10.1039/c4cc07518h

www.rsc.org/chemcomm

Efficient photovoltaic and electroluminescent perovskite devices†

Lidón Gil-Escrig,‡ Giulia Longo,‡ Antonio Pertegás, Cristina Roldán-Carmona, A. Soriano, Michele Sessolo and Henk J. Bolink*

Planar diode structures employing hybrid organic–inorganic methylammonium lead iodide perovskites lead to multifunctional devices exhibiting both a high photovoltaic efficiency and good electroluminescence. The electroluminescence strongly improves at higher current density applied using a pulsed driving method.

Hybrid organic–inorganic methylammonium lead iodide perovskites ($CH_3NH_3PbI_3$) have recently been used to prepare very efficient solar cells.[1–11] Previously, these materials have been used to prepare light-emitting diodes (LEDs).[12,13] Electroluminescence was first shown at very low temperatures,[14] and later by incorporating an organic emitter also at room temperature.[12] These devices, however, were not obtained with the same material used in recent efficient solar cells, *i.e.* the methylammonium lead iodide which adopts the 3D perovskite structure. The LEDs were fabricated using 2D layered lead iodide and chloride perovskites containing longer alkylammonium salts. Recently, it was demonstrated that also the 3D $CH_3NH_3PbI_3$ perovskite exhibits strong photoluminescence quantum yield (PLQY) up to 70% at high excitation intensity,[15] and were incorporated into LEDs.[16] Hence, this opens up the possibility to prepare a multi-functional device that shows simultaneously efficient photocurrent generation and electroluminescence.[17] Such devices were shown previously, albeit with rather low photovoltaic efficiency (<1%).[18–20]

Two main types of architectures for $CH_3NH_3PbI_3$ based photovoltaic devices have been demonstrated so far, either using mesoporous metal oxide scaffolds or planar structures.[3,4,21] In the latter either a metal oxide or an organic hole blocking layer is employed, resulting in the transparent bottom electrode being the electron or hole collector, respectively. Recently, we showed a device architecture in which the perovskite layer is sandwiched in between an organic hole and electron blocking layer leading to photovoltaic efficiencies close to 15%.[5,22] Such a structure is frequently used in organic light-emitting diodes (OLEDs) to confine electrons and holes in the light-emitting layer.[23] In a similar device layout and using $CH_3NH_3PbBr_3$ perovskite nanoparticles bright green electroluminescence was observed.[24] Thin films based on these perovskite nanoparticles exhibited PLQY's above 20% at low excitation intensity. Therefore, the planar architecture with the hole and electron blocking layers is also expected to lead to efficient light-emission in view of the high PLQY's observed in thin films of $CH_3NH_3PbI_3$. However, a high work function electrode, Au, was used in the solar cell configuration. Even though it works well to extract electrons, it is not ideal for their injection into to the lowest unoccupied molecular orbital (LUMO) of the electron transporting layer. Therefore, we have adapted the architecture by employing a thicker electron transporting–hole blocking layer and a low workfunction top electrode. Using this architecture the device exhibits simultaneously a high photovoltaic efficiency and good electroluminescence.

The device layout is shown in Fig. 1a and consists of a 80 nm poly(3,4-ethylenedioxythiophene):poly(styrene sulfonic acid) (PEDOT:PSS) layer and a thin layer (20 nm) of poly[*N*,*N*′-bis(4-butylphenyl)-*N*,*N*′-bis(phenyl)benzidine] (polyTPD) as the electron blocking layer. On top of this, the $CH_3NH_3PbI_3$ was thermally evaporated to a thickness of 320 nm, using a protocol described previously,[5] followed by a hole blocking layer of [6,6]-phenyl C_{61}-butyric acid methylester (PCBM) (100 nm).[25] The device was

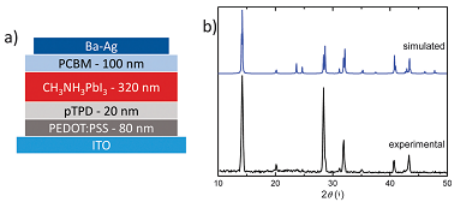

Fig. 1 (a) Device layout. (b) Simulated and experimental grazing incidence X-ray diffraction (GIXRD) pattern for a $CH_3NH_3PbI_3$ perovskite thin film.

Instituto de Ciencia Molecular, Universidad de Valencia, c/Catedrático J. Beltrán, 2, 46980 Paterna, Spain. E-mail: henk.bolink@uv.es

† Electronic supplementary information (ESI) available: Distribution of the power conversion efficiencies and EQE_{EL} for a series of devices, EQE *vs.* current density and materials and methods. See DOI: 10.1039/c4cc07518h

‡ These authors contributed equally to this work.

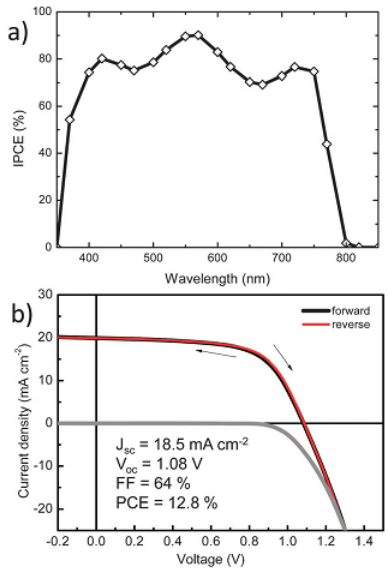

Fig. 2 (a) Typical IPCE spectrum for the solar cells. (b) *J–V* curves in the dark (gray line) and under 1 sun illumination using forward and reverse scan directions (black and red line, respectively).

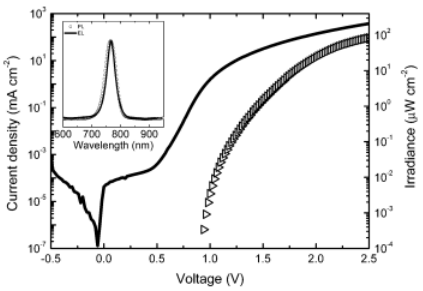

Fig. 3 Current density (line) and radiance (open triangles) *versus* applied voltage. Inset: electroluminescence (EL) spectrum (solid line) emitted by the device and photoluminescence (PL) spectrum (open circles) recorded using a 405 nm CW laser as the excitation source.

completed by the evaporation of a Ba (10 nm) top electrode covered with Ag (100 nm). Both the polyTPD and the PCBM layers were deposited using a meniscus coating process to ensure high quality films.[26] The X-ray diffraction pattern of the $CH_3NH_3PbI_3$ layer is shown in Fig. 1b demonstrating a good match with the calculated one and ensuring the formation of the perovskite structure.

First, the photovoltaic effect of these devices was examined. The incident photon to electron conversion efficiency (IPCE, Fig. 2a) was determined as a function of wavelength and the current density *versus* voltage characteristics (*J–V*, Fig. 2b) were determined in dark and under 1 sun illumination. The key performance data are similar to those obtained previously for similar devices yet with an Au top (electron collecting) electrode.[5,22] The spread of performances for a series of devices is depicted in Fig. S1 (ESI†).

In the next step we used this same device configuration and evaluated the radiative recombination (emission) and the current density *versus* applied voltage of various devices. A sensitive Si-photodiode coupled to an integrating sphere was used to obtain the irradiance of the device. The emission spectrum is shown in Fig. 3, with a maximum at 765 nm. The irradiance rapidly increases around an applied voltage of 0.9 V and reaches values of 84 μW cm^{-2} at 2.5 V (Fig. 3). The low voltage required for electroluminescence is indicative of very good charge transport properties in this device stack. The *J–V* curves (Fig. 3) shows the typical diode characteristics with a sharp current rise related to the diffusion current. A flat-band or build-in potential (V_{bi}) of 1 V was estimated with the deviation from the diffusion limited regime.[27]

This implies that the open circuit voltage V_{oc} is slightly above the V_{bi}. Yet, the S-shape curve which is frequently observed in such cases for organic photovoltaic devices, is here not seen.[28] Apparently, in these perovskite devices the diffusion current is sufficiently high.

The external quantum efficiency (EQE_{EL}) of the device reaches a maximum of approximately 0.04% (Fig. S2, ESI†). This is similar to the EQE_{EL} previously reported by us for the devices using a gold top electrode (0.012%).[29] The spread of performances of the EQE_{EL} for different devices is shown in Fig. S3 (ESI†). Such efficiencies are approximately 2 orders of magnitude lower than the most efficient thin film near infrared emitting devices.[30,31] The PLQY of a similar perovskite material, the so-called mixed halogen perovskites $CH_3NH_3PbI_{3-x}Cl_x$, is strongly dependent on the excitation intensity in the range from 25 to 2000 mW cm^{-2}.[15] In our devices the $CH_3NH_3PbI_3$ is prepared from only the iodide precursors and we were unable to detect a photoluminescence signal using a quantum yield measurement system (C9920-02, Hamamatsu Photonics) with a Xe lamp as the excitation source and a multichannel spectrometer (Hamamatsu PMA-11) as the optical detector. Using the same setup for a film containing $CH_3NH_3PbBr_3$ perovskite nanoparticles we observed a PLQY of 23%.[24] Only when the $CH_3NH_3PbI_3$ is excited with a CW laser (at 405 nm) a photoluminescence signal could be observed.[29] In the multifunctional device employing $CH_3NH_3PbI_3$ the electroluminescence increases with increasing current density (Fig. 4a). Holes and electrons are confined to the perovskite layer due to the efficient electron and hole blocking materials adjacent to it. This therefore leads to a strong increase in excitons formation and thus electroluminescence in that layer. Hence, a similar behavior as was observed for the $CH_3NH_3PbI_{3-x}Cl_x$ perovskite might take place. In order to increase the excitation intensity, the devices were driven with pulsed current using a periodic square waveform, with duty cycle of 50% at a frequency of 100 Hz. This allows for much higher current densities while avoiding rapid degradation as the device is allowed to relax (dissipate excess heat) in the off state. Average current densities up to 1150 mA cm^{-2} (Fig. 4a), corresponding to 2300 mA cm^{-2} in the on phase of the pulse (Fig. 4b), were obtained. The resulting irradiance increases steadily,

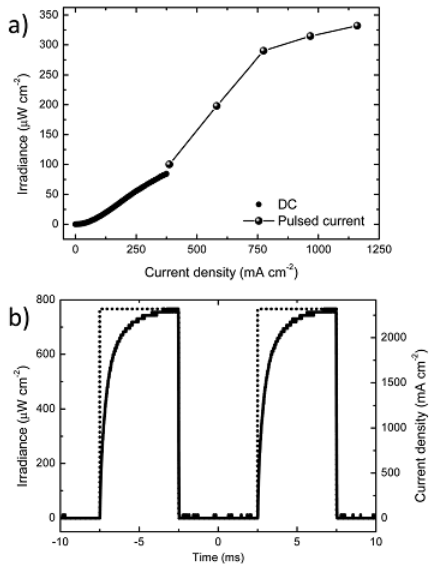

Fig. 4 (a) Irradiance *versus* current density for a dc- (symbols) and a pulsed current-driven (line and symbols) device. Two regimes define the different operation modes: up to a current density of 375 mA cm^{-2} the device was operated in dc mode, beyond that the current was applied as a square waveform, with a duty cycle of 50% at a frequency of 100 Hz. (b) Detail of the irradiance when the device is operated in the pulsed current mode.

exceeding 330 μW cm^{-2} at the maximum current density. The radiance meter integrates the emitted photons over a period of 100 ms and as such records the average emission. Hence, the light output was also measured using a Si-photodiode coupled to an oscilloscope enabling the visualization of the on–off cycles in correspondence to the applied current pulses (Fig. 4b). Intense electroluminescence up to 770 μW cm^{-2} is reached in the pulse peak with a rising time (time to reach 90% of the maximum signal) of approximately 4 ms. This slow response can be ascribed either to a low exciton formation rate or to a slow depletion of the exciton quenching sites, or both.

In summary, a simple thin film device consisting of a hybrid organic–inorganic perovskite as the absorbing and emitting layer, sandwiched in between organic electron and hole blocking layers, can be used to efficiently generate electricity and light depending on the operation conditions. The photovoltaic power conversion efficiency of 12.8% is among the highest recorded for similar thin film devices. The electroluminescence observed when driving the device in pulsed current mode reaches interesting values and the external quantum yield is only two orders of magnitude below the best performing near infrared planar LED. This is remarkable in view of the very low PLQY of the active material used, and implies a prospect towards applications for these devices when strategies are employed to increase the PLQY.

We acknowledge Dr Kristofer Tvingstedt from the Julius Maximilians University of Würzburg for the CW laser excited PL measurements and Jorge Ferrando for the pulsed EL measurements. This work has been supported by the European Union 7th framework program LUMINET (grant 316906), the Spanish Ministry of Economy and Competitiveness (MINECO) (MAT2011-24594) and the Generalitat Valenciana (Prometeo/2012/053). A.P. acknowledges MINECO for an FPI grant.

Notes and references

1 M. M. Lee, J. Teuscher, T. Miyasaka, T. N. Murakami and H. J. Snaith, *Science*, 2012, **338**, 643–647.
2 J. M. Ball, M. M. Lee, A. Hey and H. J. Snaith, *Energy Environ. Sci.*, 2013, **6**, 1739–1743.
3 J. Burschka, N. Pellet, S.-J. Moon, R. Humphry-Baker, P. Gao, M. K. Nazeeruddin and M. Gratzel, *Nature*, 2013, **499**, 316–319.
4 M. Liu, M. B. Johnston and H. J. Snaith, *Nature*, 2013, **501**, 395–398.
5 O. Malinkiewicz, A. Yella, Y. H. Lee, G. M. Espallargas, M. Graetzel, M. K. Nazeeruddin and H. J. Bolink, *Nat. Photonics*, 2014, **8**, 128–132.
6 D. Liu and T. L. Kelly, *Nat. Photonics*, 2014, **8**, 133–138.
7 N. J. Jeon, H. G. Lee, Y. C. Kim, J. Seo, J. H. Noh, J. Lee and S. I. Seok, *J. Am. Chem. Soc.*, 2014, **136**, 7837–7840.
8 Q. Chen, H. P. Zhou, Z. R. Hong, S. Luo, H. S. Duan, H. H. Wang, Y. S. Liu, G. Li and Y. Yang, *J. Am. Chem. Soc.*, 2014, **136**, 622–625.
9 H. S. Kim, J. W. Lee, N. Yantara, P. P. Boix, S. A. Kulkarni, S. Mhaisalkar, M. Gratzel and N. G. Park, *Nano Lett.*, 2013, **13**, 2412–2417.
10 W.-J. Yin, T. Shi and Y. Yan, *Adv. Mater.*, 2014, **26**, 4653–4658.
11 M. A. Green, A. Ho-Baillie and H. J. Snaith, *Nat. Photonics*, 2014, **8**, 506–514.
12 K. Chondroudis and D. B. Mitzi, *Chem. Mater.*, 1999, **11**, 3028–3030.
13 T. Hattori, T. Taira, M. Era, T. Tsutsui and S. Saito, *Chem. Phys. Lett.*, 1996, **254**, 103–108.
14 M. Era, S. Morimoto, T. Tsutsui and S. Saito, *Appl. Phys. Lett.*, 1994, **65**, 676.
15 F. Deschler, M. Price, S. Pathak, L. E. Klintberg, D.-D. Jarausch, R. Higler, S. Hüttner, T. Leijtens, S. D. Stranks, H. J. Snaith, M. Atatüre, R. T. Phillips and R. H. Friend, *J. Phys. Chem. Lett.*, 2014, **5**, 1421–1426.
16 Z.-K. Tan, R. S. Moghaddam, M. L. Lai, P. Docampo, R. Higler, F. Deschler, M. Price, A. Sadhanala, L. M. Pazos, D. Credgington, F. Hanusch, T. Bein, H. J. Snaith and R. H. Friend, *Nat. Nanotechnol.*, 2014, **9**, 687–692.
17 A. K. Pandey and J. M. Nunzi, *Adv. Mater.*, 2007, **19**, 3613–3617.
18 G. Yu, C. Zhang and A. J. Heeger, *Appl. Phys. Lett.*, 1994, **64**, 1540–1542.
19 W. Rieß, S. Karg, V. Dyakonov, M. Meier and M. Schwoerer, *J. Lumin.*, 1994, **60–61**, 906–911.
20 D. A. Bernards, S. Flores-Torres, H. D. Abruña and G. G. Malliaras, *Science*, 2006, **313**, 1416–1419.
21 H. J. Snaith, *J. Phys. Chem. Lett.*, 2013, **4**, 3623–3630.
22 O. Malinkiewicz, C. Roldán-Carmona, A. Soriano, E. Bandiello, L. Camacho, M. K. Nazeeruddin and H. J. Bolink, *Adv. Energy Mater.*, 2014, 1400345.
23 H. Sasabe and J. Kido, *J. Mater. Chem. C*, 2013, **1**, 1699–1707.
24 L. C. Schmidt, A. Pertegas, S. Gonzalez-Carrero, O. Malinkiewicz, S. Agouram, G. Minguez Espallargas, H. J. Bolink, R. E. Galian and J. Perez-Prieto, *J. Am. Chem. Soc.*, 2014, **136**, 850–853.
25 G. Yu, J. Gao, J. C. Hummelen, F. Wudl and A. J. Heeger, *Science*, 1995, **270**, 1789–1791.
26 O. Malinkiewicz, M. Lenes, H. Brine and H. J. Bolink, *RSC Adv.*, 2012, **2**, 3335–3339.
27 P. de Bruyn, A. H. P. van Rest, G. A. H. Wetzelaer, D. M. de Leeuw and P. W. M. Blom, *Phys. Rev. Lett.*, 2013, **111**, 186801.
28 C. Uhrich, D. Wynands, S. Olthof, M. K. Riede, K. Leo, S. Sonntag, B. Maennig and M. Pfeiffer, *J. Appl. Phys.*, 2008, **104**, 043107.
29 K. Tvingstedt, O. Malinkiewicz, A. Baumann, C. Deibel, H. J. Snaith, V. Dyakonov and H. J. Bolink, *Sci. Rep.*, 2014, **4**, 6071.
30 C. Borek, K. Hanson, P. I. Djurovich, M. E. Thompson, K. Aznavour, R. Bau, Y. R. Sun, S. R. Forrest, J. Brooks, L. Michalski and J. Brown, *Angew. Chem., Int. Ed.*, 2007, **46**, 1109–1112.
31 A. Pertegas, N. M. Shavaleev, D. Tordera, E. Orti, M. K. Nazeeruddin and H. J. Bolink, *J. Mater. Chem. C*, 2014, **2**, 1605–1611.

Chapter 4.

Highly luminescent perovskite–aluminum oxide composites.

4.1 Introduction

Three dimensional hybrid perovskites like methylammonium lead bromide ($MAPbBr_3$) have been recently shown as suitable material for light-emitting applications.[29] One of the most important parameters for evaluating the efficiency of a LED is the external quantum efficiency of the electroluminescence, indicating the number of photons leaving the device per injected carriers. It can be expressed as a product of different factors, representing the efficiency of different process occurring in the devices:

$$EQE = \frac{n^\circ\ photons\ out}{n^\circ\ injected\ electrons} = \eta_{rad} * \eta_{ext} * \eta_{inj}$$

Equation 8

η_{inj} represents the charge injection efficiency and is hence determined by the charge injection/transport in the device. The implementation of ohmic contacts and the use of multilayer structures with optimized energy levels ensure high injection efficiency. η_{ext} is the outcoupling efficiency, the fraction of generated photons actually leaving the device, and can be modified by geometrical factors of the LEDs. η_{rad} corresponds to the radiative efficiency of the active material, and it is directly determined by the photoluminescence quantum yield (PLQY) of the perovskite film. Consequently, the enhancement of the PLQY is key to obtain efficient electroluminescent devices. The PLQY of $MAPbBr_3$ is typically low at low excitation fluence, and increases only with increasing excitation density for example by using high intensity monochromatic light source like a laser. As for the $MAPbI_3$ perovskite discussed in the previous chapter, this fluence-dependence is due to the high trap concentration which increases the non-radiative recombination reducing the PLQY.[90] From a device point of view, high photoluminescence at low excitation intensity is strongly desirable since in principle it would lead to devices with low power consumption. The photophysics of methylammonium lead trihalides perovskites is strongly influenced by the morphology of the film, and a control over the latter allows to reduce the trap concentration, favoring radiative recombination.[20] In analogy to inorganic

semiconductor quantum dots, the preparation of perovskite nanoparticles has been shown to be effective to increase the photoluminescence of $MAPbBr_3$, with PLQY exceeding 90%.[91-93] However, when nanoparticles are processed in thin-film, they tend to aggregate reducing the PLQY due to augmented charge transfer and hence higher probability of trapping.[94] An alternative for the confinement of the crystal growth, avoiding particles aggregation, is the combination of perovskites with dielectric materials like organic molecules[29, 95] or polymers.[96, 97] The addition of amorphous materials favors the formation of uniform and smooth layers, which is desirable for the preparation of high quality diodes. The size of the perovskite grains can be controlled by the quantity of the inert material added to the composite, providing an easy tool to tune the perovskite grain dimensions and, consequently, its optoelectronic properties. In some cases, however, the dielectric nature and the amount of additives hinder the charge transport through the perovskite layer, resulting in poorly performing devices. The infiltration of the perovskite into a porous metal oxide scaffold could be a solution that provides both small crystal dimension and connectivity among the perovskite grains. It has been shown that the deposition of $MAPbBr_3$ on top of an Al_2O_3 mesoporous matrix improve the photoluminescence, even if a quantitative evaluation of the phenomena was not presented.[98] In that work the porous metal oxide was prepared through sintering process at high temperature, limiting the use of plastic substrates and in general of temperature-sensitive materials. In this chapter, an alternative method consisting in the simultaneous formation of the oxide scaffold and the perovskite, is reported. Highly luminescent $MAPbBr_3$-Al_2O_3 composites using alumina nanoparticles (NPs) have been prepared. These films have been deposited in air and show enhanced environmental stability. Particular attention has been given to the perovskite precursor stoichiometry, which has been selected through a preliminary study that is described in detail in the following paragraphs.

4.2 Materials and methods

Methylammonium bromide (MABr, Dyesol), lead bromide ($PbBr_2$, > 98% Sigma Aldrich), dimethylformamide (DMF, anhydrous, 99.8%, Sigma Aldrich), PEDOT:PSS (Clevios P VP AI4083), Nafions (Nafions perfluorinated resin solution, 5 wt.% in lower aliphatic alcohols and water, Aldrich), 1,3-Bis[3,5-di(pyridin-3-yl)phenyl]benzene (BmPyPhB, Lumtec) were used as-received without further purification.

For the preliminary compositional study, solutions of stoichiometric (MABr/PbBr = 1/1) and non-stoichiometric (MABr/PbBr = 3/1) precursors at 70 mg/mL were prepared in DMF using stock solutions of the organic and inorganic components. The stoichiometric (F1) and non-stoichiometric (F3) solutions were deposited by single step spin coating and were annealed at 90 °C for 15 min. All the processes were performed in a nitrogen filled glove box. For the preparation of the perovskite-alumina composites, different percentage in weight of a 20 wt.% water dispersion of alumina nanoparticles (30, 50 and 75 wt.%) were added to the non-stoichiometric perovskite solution described above. The layer was prepared by depositing the precursor solution by spin coating followed by 1 hour of thermal treatment at 90 °C. In this case the film deposition and its annealing were performed in air.

For solid state nuclear magnetic resonance (NMR) and x-ray diffraction (XRD) analysis, powder samples were prepared by precipitation of a 40 wt.% solution of stoichiometric (P1) and nonstoichiometric precursors (P3), upon addition of chlorobenzene as precipitating agent. The polycrystalline materials obtained were dried at 70 °C for 48 h. Part of the P3 powder was further annealed at 115 °C for 24 h. The ^{13}C magic angle spinning (MAS) spectra were acquired on a Bruker Avance 300 MHz, with sample spinning at 10 kHz using a ^{1}H-decoupling experiment. A long recycle-delay of 60 s was used to ensure a reliable quantitative measurement. The ^{13}C NMR chemical shift is referenced to an alanine $–CH_3–$ at 20.5 ppm. Solutions at 40 wt.% were also employed to prepare

the optoelectronic devices reported in this work. For the hole injection layer, a blend of PEDOT:PSS and Nafion (a commercial available ionomer) was used as this has been reported to increase the electrode work function and hence improve hole injection.[99] A blend of the suspensions (PEDOT:PSS/Nafion 1 mL:1.20 mL) was spin-coated on top of an ITO patterned glass substrate, and then annealed at 150 °C for 15 min. The perovskite active layers were deposited in a nitrogen filled glovebox by spin coating the precursor solutions followed by annealing at 100 °C for 15 min. The electron transport (hole blocking) layer (BmPyPhB) and the top metal electrode (5 nm Ba capped with 100 nm Ag) were thermally evaporated in a high vacuum chamber with a base pressure of 10^{-6} mbar. Devices were not encapsulated and were characterized in the nitrogen filled glove box. The X-ray diffractograms of the $MAPbBr_3$-Al_2O_3 composites were performed on thin film using an Empyrean PANalytical powder diffractometer, using Cu Kα1 radiation. The SEM images were collected on thin-films deposited on ITO-coated glass substrates.

4.3 Discussion

As described in the introduction, the morphology and optoelectronic properties of perovskites are tightly linked. The perovskite precursor stoichiometry can strongly affect the perovskite crystallization, and while its influence has been studied for methylammonium lead iodide, less attention was dedicated to the bromide analogues.[100, 101] For this reason, a preliminary comparison of the properties of stoichiometric and non-stoichiometric perovskites (MA/Pb = 1 and 3, respectively) was performed. Interestingly, bromide lead halide perovskites showed a different behavior compared to reported iodide materials. While for $MAPbI_3$ the optical differences as a function of the precursor stoichiometry were observable only at the initial stage of crystallization and disappeared with annealing, in bromide perovskites the differences with varying MA/Pb ratios are retained also in the annealed films. Stoichiometric and non-stoichiometric

perovskite powders were analyzed with X-ray diffraction and solid state ^{13}C NMR to evaluate the change in organic content after the thermal treatment (Fig. 19).

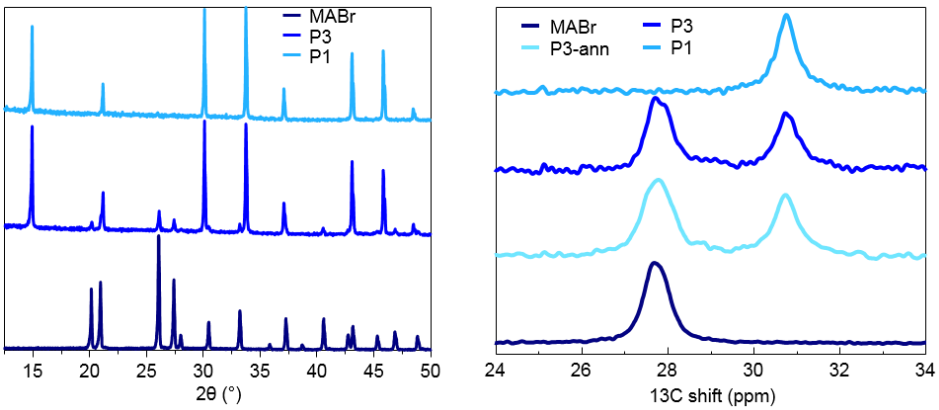

Fig. 19 *XRD patterns (left) and ^{13}C NMR spectra (right) of the non-stoichiometric and stoichiometric perovskite powders.*

The two diffractograms showed the expected diffraction pattern of the cubic $MAPbBr_3$ perovskite,[94] with the diffraction pattern for the non-stoichiometric P3 sample showing several additional peaks originating from unbound methylammonium cations. In Fig. 19 (left) the ^{13}C NMR spectra of the prepared perovskites can be observed. In the non-stoichiometric perovskite, methylammonium lead bromide generates two peaks, one at 27.9°, corresponding to the unbounded methylammonium (coinciding with the signal of reference MABr powders), and a second at 30.8°, related to bonded methylammonium bromide. The latter signal was the only one observed for the stoichiometric compound. The non-stoichiometric perovskite was further annealed at 115 °C for 24 hours to observe the evolution of the organic content when exposed to high temperatures. Interestingly, no differences in the NMR spectra were observed after thermal treatment (Fig. 19), confirming that the methylammonium bromide excess is retained in the structure even after annealing. The most prominent effect of the precursor stoichiometry on $MAPbBr_3$ is a severe change in the film morphology, as shown in Fig. 20.

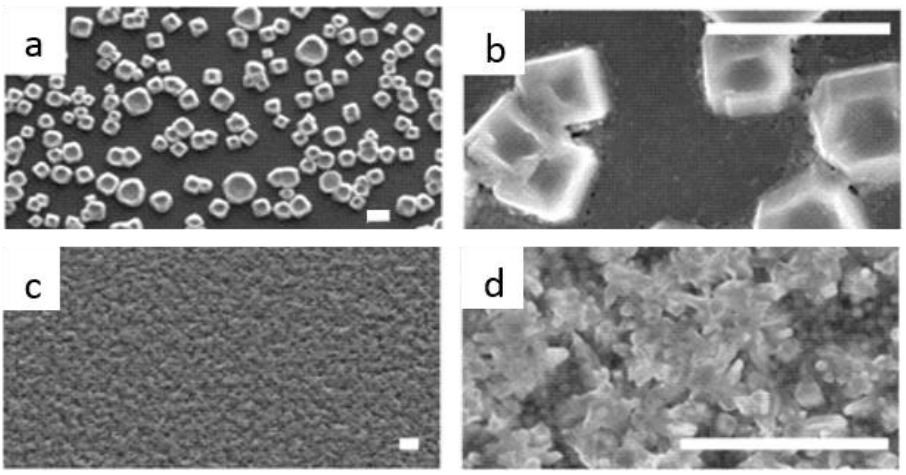

Fig. 20 *SEM images of stoichiometric (a-b) and non-stoichiometric (c-d) perovskite films at low (a-c) and high (b-d) magnification. In all the images the scale bar is 10 µm.*

The stoichiometric perovskite is characterized by the formation of large and isolated crystals with pseudo-cubic shape. The crystals, with micrometric sizes are distributed on the surface and not interconnected, resulting in a poor surface coverage and low inter-grain connectivity. On the other hand, uniform and compact perovskite films are formed with the non-stoichiometric solution. Such morphological differences are reflected in the optical properties of the perovskite films, as can been observed in Fig. 21.

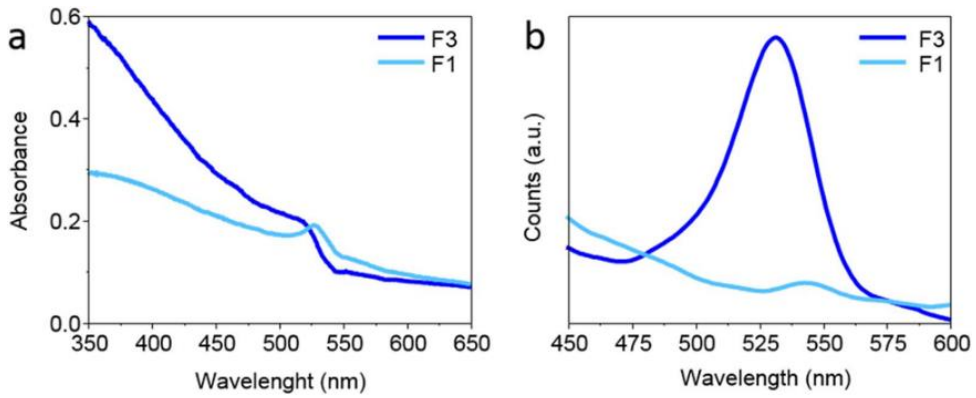

Fig. 21 *Absorption (**a**) and photoluminescence (**b**) spectra of the stoichiometric (F1) and non-stoichiometric (F3) perovskite films.*

The lower absorbance at higher energy observed for the stoichiometric film (F1) can be ascribed, at least partially, to the lower surface coverage of the perovskite, as revealed by SEM (Fig. 20). Interestingly, while the absorption onset for the stoichiometric sample is positioned at 537 nm, the non-stoichiometric perovskite film presents the onset at 530 nm. Hence the absorption onset is also influenced by the stoichiometry, and the perovskite bandgap is slightly enlarged as the organic content increases. The photoluminescence spectra were collected in an integrating sphere equipped with a low intensity excitation source (a Xe lamp coupled to a monochromator), at wavelength of 365 nm. While sample F3 showed clear photoluminescence centered at 527 nm, no emission was observed for the F1 film. To study the optoelectronic properties of the stoichiometric and non-stoichiometric perovskites, LEDs have been prepared depositing the $MAPbBr_3$ active layers from the same solutions used to prepare the polycrystalline powders. The multilayer device structure used was ITO/PEDOT:PSS-Nafion (100 nm)/$MAPbBr_3$/BmPyPhB (40 nm)/Ba (5 nm)-Ag (100 nm). The thickness of the active layer was about 900 nm. In Fig. 22 the current density (J) and luminance (L) versus voltage (V) characteristics are reported.

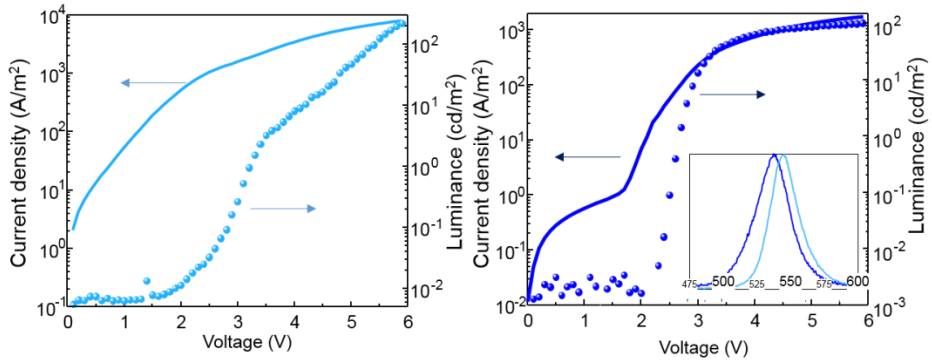

Fig. 22 *IVL characteristics of the stoichiometric perovskite LED (LED1, left) and non-stoichiometric perovskite device (LED3, right). In the inset graph, the normalized electroluminescence of the two diodes is reported.*

The device behavior observed varying the perovskite stoichiometry is directly correlated with the differences in the film morphology. LED1, the device with

the stoichiometric perovskite, suffers of a high leakage current due to the poor surface coverage of the perovskite film. The direct contact between the underlying PEDOT and the electron transport layer provides a low resistance path where the charges can easily flow even at low voltages. The current density increases monotonically at higher biases, as opposed to LED3 for which the diode behavior is precisely defined. Both devices show electroluminescence with maxima at 537 nm and 545 nm, for the non-stoichiometric and the stoichiometric perovskite, respectively, in accordance with the absorbance onset shift. It is noteworthy that even though only the sample with an excess methylammonium displayed photoluminescence, both the devices show electroluminescence. Most likely, the large amount of MABr present in the non-stoichiometric perovskite is able to passivate defect states which otherwise quench the photoluminescence in the stoichiometric crystals. In LEDs, trap states can be filled due to the large density of charge carriers injected, leading to intense electroluminescence even from the stoichiometric perovskite.

This initial study revealed that the excess of methylammonium bromide is beneficial for the formation of uniform and compact films that show photoluminescence even at low excitation fluence. Therefore, non-stoichiometric compounds with MA/Pb ratio of 3 have been used when developing the alumina-perovskite blends. Three composite materials with increasing alumina content were prepared, 30 wt.%, 50 wt.% and 75 wt.%. The solutions were deposited by single step spin-coating on glass or ITO for the optical and structural characterization. In Fig. 23 their absorption and photoluminescence spectra are reported.

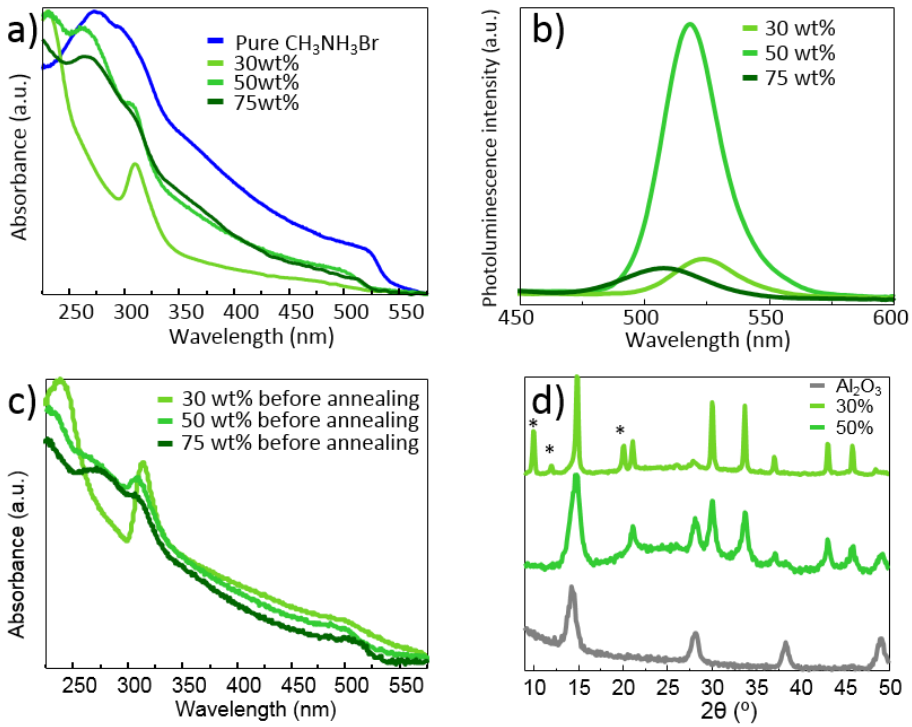

Fig. 23 a) *Absorption and* ***b)*** *photoluminescence spectra of the annealed perovskite and composite films.* ***c)*** *Absorbance of the MAPbBr₃-Al₂O₃ films before thermal annealing.* ***d)*** *X-Ray diffraction patterns of alumina and perovskite-alumina films.*

The samples with a high content of Al_2O_3 NPs (50 and 75 wt.%) show a blue-shifted absorption onset compared to the pure $MAPbBr_3$, suggesting that smaller perovskite grains are formed due to the spatial constrains induced by the formation of a porous NPs scaffolds.[94] The samples with a low NPs content (30 wt.%) are not fully converted to the perovskite structure with this annealing time and temperature, as evidenced by the spectral feature at 310 nm which corresponds to lead bromide complexes.[102] By increasing the alumina NPs content, the peak at 310 nm fades while the absorption onset at 525 nm, corresponding to the band-to-band transition of the perovskite, appears. These observations suggest that the presence of alumina NPs favors the perovskite formation, even if its precise role in the process has not been clarified yet. Interestingly, if the absorption spectra are registered before the thermal treatment (Fig. 23c) of the perovskite/Al_2O_3 films with high inorganic NPs content they

spontaneously form the crystalline perovskite phase even at room temperature. In the 50 and 75 wt.% composites, the pronounced absorption onset, characteristic of the $MAPbBr_3$, is present. However the 50 wt.% spectrum also shows the signal of unreacted lead bromide (that disappears with thermal treatment), supporting the idea that higher concentrations of alumina fosters the perovskite crystallization. In addition the alumina shows also a perovskite stabilization effect. In fact, while perovskite compounds are sensitive to air and moisture, the blends presented here are deposited in air and lead to the formation of highly crystalline perovskites, as shown by the X-Ray diffraction (Fig. 23d). The characteristic diffraction peaks of $MAPbBr_3$, positioned at 14.9°, 30.1° and 33.8° are clearly visible in the two diffractograms of the composite materials, even if signals coming from unreacted lead and methylammonium bromide (marked with stars) are still observable for the 30 wt.% sample, in agreement with the absorption spectrum. As the amount of alumina increases, the diffractogram baseline rises, indicating the presence of amorphous compounds induced by the larger amount of oxide nanoparticles. Interestingly, the diffraction peaks broadens substantially, implying the formation of smaller perovskite grains. In the 75 wt.% composite material, the diffractograms is dominated by the signals of the aluminum oxide, and for this reason is not reported. The photoluminescence characteristics of the thin films were studied using a Xe lamp coupled to a monochromator as the excitation source (< 0.4 mW/cm^2) and a spectrometer coupled to an integrated sphere (Hamamatsu C9920-02 with a Hamamatsu PMA-11 optical detector) in order to quantitatively determine the PLQY. Pure perovskite and low NPs content film show low photoluminescence, with PLQY values closer to the measurement error of the setup (< 5%). When higher alumina concentration (50 wt.%) is used, the expected green emission of the $MAPbBr_3$ perovskite is detected, while it is quenched for alumina concentration of 75 wt.%. The PLQY reaches a maximum of 26 % for a NP concentration of 50 wt.%, and it can be further enhanced up to 39 % if the annealing time is increased from 1 to 3 hours. These values are particularly striking when taking into account the simple material preparation and its

processing in air from water-based dispersions. Together with the increase in the PLQY with higher Al_2O_3 NP content, a slight but continuous blue-shift of the emission energy occurs. This behavior is generally associated with the distortion of the inorganic perovskite framework that translates in a change of the bandgap.[103] In order to correlate the enhancement of the perovskite photoluminescence with a morphological change, scanning and transmission electron microscopy was carried out on the samples. The results are reported in Fig. 24.

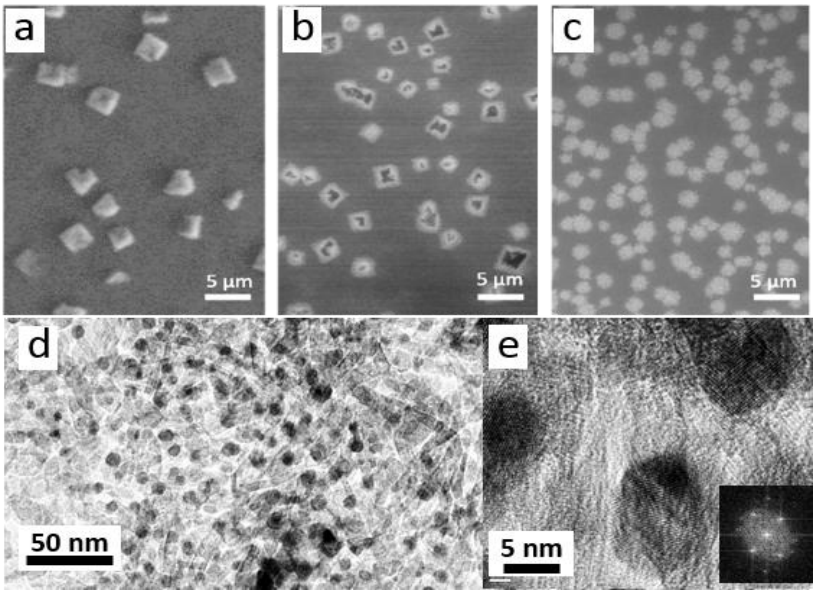

Fig. 24 *SEM pictures of the* ***a)*** *30 wt.%,* ***b)*** *50 wt.%,* ***c)*** *75 wt.% perovskite composite films.* ***d)*** *TEM image of 50 wt.% Al_2O_3 NPs content.* ***e)*** *HR-TEM image of few isolated perovskite NPs with the corresponding FFT.*

The surface of the samples with 30, 50 and 75 wt.% Al_2O_3 NP (Fig. 24 a, b and c, respectively), is characterized by the presence of relatively large crystals (diameter of 2-4 µm) protruded from a smooth surface. Atomic force microscopy shows that the crystals protrude about 200 nm above the sample surface. At low alumina concentration (30 wt.%) the perovskite aggregation is favored, hence large crystals form which likely reduce the PLQY. With increasing Al_2O_3 content, the formation of the crystals seems to be hindered, finally fading into

round aggregates at the highest measured concentration, which could justify the low PLQY observed (Fig. 24c). The observed blue-shift and the high PLQY of the 50 wt.% sample are, however, most likely originating from the presence of small crystals and not from the large structures observed in the SEM pictures. To investigate the presence of smaller perovskite phases, transmission electron microscopy (TEM) was performed on powders obtained from scratched films. The TEM analysis (Fig. 24d) shows rod-like Al_2O_3 NPs assemblies forming a dense mesoporous layer, containing a high concentration of isotropic nanoparticles with a considerably different contrast. The high resolution TEM (HR-TEM, Fig. 24e) shows that the observed nanoparticles are highly crystalline, and the fast Fourier transform (FFT) of single selected nanocrystal confirms the presence of the cubic $MAPbBr_3$ phase. The morphological characterization confirmed that the observed blue-shift of the absorption onset and of the photoluminescence is related with a reduction of the crystals size, and that the large PLQY is likely due to an increase of the exciton binding energy of the nanocrystals compared to the bulk perovskite.[104] In order to shed light on these mechanism, time resolved photoluminescence was performed in Fig. 25.

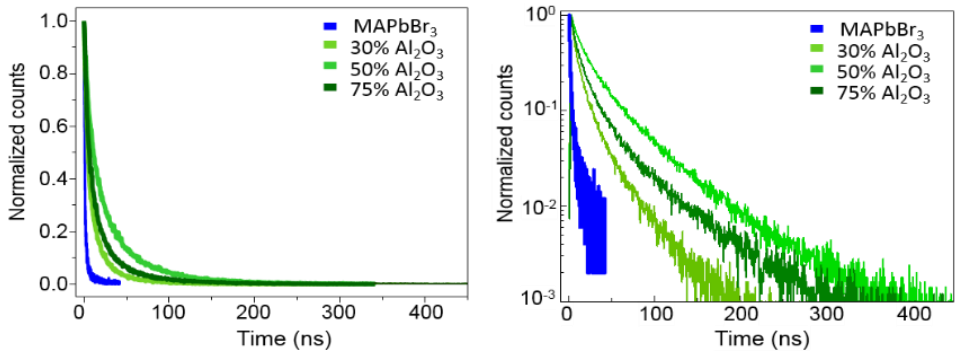

Fig. 25 *Time resolved photoluminescence (linear scale on the left and logarithmic scale on the right) measurements taken at the maximum emission wavelength, with an excitation wavelength of 380 nm.*

The lifetime of the perovskite-alumina composites are considerably longer compared to the pure $MAPbBr_3$, in accordance with the increase in

photoluminescence quantum yield. The average lifetime was calculated using a three-exponential function fitting to the decay curves, and was used to estimate the radiative and non-radiative recombination rate constants (k_R and k_{NR}, respectively). The PLQY, the average lifetime τ_{AVE} and the two rate constants are related through the following equations:

$$PLQY = k_R \tau_{AVE}$$

Equation 9

$$\tau_{AVE} = \frac{1}{k_R + k_{NR}}$$

Equation 10

The parameters calculated from measurements of the PLQY and lifetime are listed in the table below.

Sample	PLQY	τ_{ave} (ns)	k_R (10^6 s^{-1})	k_{NR} (10^6 s^{-1})
$MAPbBr_3$	0.030	2.69	11.1	360
30 wt.%	0.108	16.4	6.58	54.3
50 wt.%	0.256	39.1	6.20	19.4
75 wt.%	0.092	29.7	3.1	30.6

Tab. 2 *Measured PLQY and average photoluminescence lifetime and the calculated radiative and non radiative rate constants for the set of alumina-perovskite samples.*

The PL decay analysis confirms that the non-radiative recombination path (which is extremely high in the pure perovskite) is sensitively reduced by the addition of the aluminum oxide. Importantly, the radiative rate constant follows the trend observed for the PLQY, becoming larger in the sample containing the 50 wt.% of alumina. The reduction of the non-radiative recombination with the addition of Al_2O_3 suggests that the alumina NPs not only reduce the size of the perovskite crystals, but also passivate trap states which otherwise limit the photoluminescence in bulk methylammonium lead bromide perovskite.

4.4 Conclusions

In this work the effect of the precursor stoichiometry and of the addition of aluminum oxide nanoparticles on the morphology and optical properties of perovskite thin-films were investigated. It was demonstrated that an excess of methylammonium bromide is beneficial in terms of both film formation and luminescence properties. Uniform and compact layers, showing intense photo- and electroluminescence, were obtained with a three-fold excess of MABr with respect to $PbBr_2$. The unbound organic cation most likely passivates trap states enhancing the radiative recombination, leading to bright photoluminescence even at low excitation fluence. The non-stoichiometric compound was then employed in the preparation of perovskite-alumina composite thin-films. These materials showed a strong dependence of their optical properties depending on the amount of alumina. The highest PLQY (39 %) was obtained for films containing 50 wt.% of alumina nanoparticles. The morphological analysis showed the coexistence of different perovskite structures, in particular of large crystals emerging from the surface and nanoparticles embedded in the metal oxide scaffold. The formation of perovskite nanostructures is responsible for the enhanced PLQY and increased photoluminescence lifetimes.

Journal of Luminescence 189 (2017) 120–125

Contents lists available at ScienceDirect

Journal of Luminescence

journal homepage: www.elsevier.com/locate/jlumin

Effect of the precursor's stoichiometry on the optoelectronic properties of methylammonium lead bromide perovskites

Giulia Longo [a], Alan Wong [b], Michele Sessolo [a,*], Henk J. Bolink [a]

[a] Instituto de Ciencia Molecular, Universidad de Valencia, C/ Catedrático José Beltrán, 2, 46980 Paterna, Spain
[b] NIMBE, CEA, CNRS, Université Paris-Saclay, CEA Saclay, Gif-sur-Yvette, 91191 Paris, France

ARTICLE INFO

Article history:
Received 14 April 2016
Accepted 22 March 2017
Available online 23 March 2017

ABSTRACT

Methylammonium lead bromide ($MAPbBr_3$) perovskites have been widely studied in applications such as lasers and light-emitting diodes, thanks to their favorable bandgap, efficient charge transport, and the possibility of processing by simple solution methods. The film morphology has a large impact on the optical and electronic properties of the material; hence the deposition methods and the type of precursors used are crucial in the preparation of efficient optoelectronic devices. Here we studied the effect of the precursor's stoichiometry of solution processed $MAPbBr_3$ thin films on their optical and electronic properties. We found a drastic effect of the stoichiometry on the resulting thin film morphology, and suggest the use of excess MA cations to enhance the photo- and electroluminescence of hybrid perovskites.

1. Introduction

Organic inorganic (hybrid) perovskites are known since the beginning of the last century [1–6], but their unique optical and electronic properties have been unveiled mostly during the last thirty years. One of the advantages of hybrid perovskite over inorganic semiconductors is the possibility to obtain high quality semiconducting films by simple solution or sublimation methods. Initially, most works focused on layered (or 2D) perovskites due to the interesting properties arising from the high exciton binding energy, in the order of hundreds of meV [7–10]. Later on, three dimensional (3D) perovskites have also emerged [11,12], but it is in the last five years when hybrid 3D perovskites have been widely investigated, mainly due to the promising photovoltaic performances of methylammonium lead iodide $MAPbI_3$ [13–17]. During this short period, the power conversion efficiency of perovskite solar cells rapidly increased up to 22% (close to Silicon photovoltaic performances), thanks to a continuous optimization of the perovskite absorber and of the device structure [18]. The analogous bromide compound, the $MAPbBr_3$ perovskite, has been recently investigated because of its favorable optical properties (green emission, intense photoluminescence) and its potential for the development of light-emitting diodes (LEDs) and lasers [19–22]. Since the first report of room temperature electroluminescence from 3D perovskite LEDs [19], several works have addressed the issues related with the achievement of efficient LEDs with hybrid perovskites. Most of the efforts has been directed towards the optimization of the charge transport layers, either organic or inorganic, in order to efficiently inject and confine carriers in the perovskite film [23,24]. Within this perspective, the challenge is to efficiently inject holes into the low-lying valence band of the $MAPbBr_3$ (−5.9 eV), which strongly limits the choice of the hole transport layers. One of the most promising strategies is the use of a Nafion®-modified PEDOT:PSS layer, substantially increasing the work function of the anode (up to −6.0 eV) [25]. Another property differentiating perovskites from organic semiconductors, is the relatively small exciton binding energy, implying that mostly free carriers are present at room temperature [26]. Since recombination between free carriers is a bimolecular process, the LED operation is less efficient compared to organics where the recombination is purely excitonic. As a consequence, the photoluminescence quantum yield (PLQY) is found to be proportional to the excitation intensity [21], meaning that high current densities are needed for electroluminescence, hence reducing the device power conversion efficiency. High PLQY can be achieved by limiting the growth of the perovskite crystals, enhancing the probability of radiative recombination [27,28]. Recently, highly efficient perovskite LEDs have been demonstrated by overcoming all the device and material limitations discussed above, i.e. charge injection, recombination and morphology [29]. The morphology of perovskite thin films has been found to be of crucial importance for the performance of optoelectronic devices, since it severely affects the perovskite electrical and optical properties. In order to tune the morphology of perovskite thin-films, different deposition techniques have been developed [14,28,30–33]. Importantly, the

* Corresponding author.
E-mail address: michele.sessolo@uv.es (M. Sessolo).

http://dx.doi.org/10.1016/j.jlumin.2017.03.048
0022-2313/

nature and stoichiometry of the precursor materials has a large effect on the final film composition and morphology [34].

Here, we report on the influence of the precursor's stoichiometry on the optoelectronic properties of $MAPbBr_3$ perovskite thin films. Thin films were prepared by solution processing of stoichiometric and non-stoichiometric precursors solutions with a single-step deposition (direct spin-coating of the solution followed by thermal annealing). The morphology and optical properties of the layers were investigated and the perovskite thin films were incorporated in multilayer LEDs employing organic semiconductors as charge transport layers.

2. Experimental methods

Methylammonium bromide (MABr, Dyesol), lead bromide ($PbBr_2$, ≥98% Sigma Aldrich), dimethylformamide (DMF, anhydrous, 99.8%, Sigma Aldrich), PEDOT:PSS (Clevios P VP AI4083), Nafion® (Nafion® perfluorinated resin solution, 5 wt. % in lower aliphatic alcohols and water, Aldrich), 1,3-Bis[3,5-di(pyridin-3-yl) phenyl]benzene (BmPyPhB, Lumtec) were used as-received without further purification.

2.1. Thin film preparation for optical characterization

Solution of stoichiometric ($MABr/PbBr_2=1$) and non-stoichiometric ($MABr/PbBr_2=3$) precursors at 70 mg/ml were prepared in DMF using stock solutions of the organic and inorganic components. These solutions were used to deposit the thin-film by spin-coating on glass substrates. The stoichiometric (F1) and non-stoichiometric (F3) films were annealed at 90 °C for 15 min. All the processes were performed in a nitrogen filled glove box.

2.2. Powders precipitations and device preparation

For solid state nuclear magnetic resonance (NMR) and x-ray diffraction (XRD) analysis, powder samples were prepared by precipitation of a 40 wt% solution of stoichiometric (P1) and non-stoichiometric precursors (P3), upon addition of chlorobenzene as precipitating agent. The polycrystalline materials obtained were dried at 70 °C for 48 h. Part of the P3 powder was further annealed at 115 °C for 24 h. The ^{13}C magic angle spinning (MAS) spectra were acquired on a Bruker Avance 300 MHz, with sample spinning at 10 kHz using a ^1H-decoupling experiment. A long recycle-delay of 60 s was used to ensure a reliable quantitative measurement. The ^{13}C chemical shift is referenced to an alanine $-CH_3-$ at 20.5 ppm.

Solutions at 40 wt% were also employed to prepare the optoelectronic devices reported in this work. For the hole injection layer, a blend of PEDOT:PSS and Nafion® was used as this is known to increase the electrode work function and hence improve hole injection.[35] A blend of the suspensions (PEDOT:PSS/Nafion® 1 mL:1.20 mL) was spin-coated on top of an ITO patterned glass substrate, and then annealed at 150 °C for 15 min. The perovskite active layers were deposited in a nitrogen filled glovebox by spin-coating the precursors solutions followed by annealing at 100 °C for 15 min. The electron transport (hole blocking) layer (BmPyPhB) and the top metal electrode (5 nm Ba capped with 100 nm Ag) were thermally evaporated in a high vacuum chamber with a base pressure of 10^{-6} mbar. Devices were not encapsulated and were characterized in the nitrogen filled glove box.

3. Results

The absorption and the photoluminescence spectra of $MAPbBr_3$ perovskite thin films on glass substrates for the two sets of samples (F1, MA/Pb=1 and F3, MA/Pb=3) are reported in Fig. 1.

The absorption spectra for the two samples presented similar features, with a steep absorption onset at 537 nm for the stoichiometric (F1) and 530 nm for the non-stoichiometric (F3) perovskite films, consistent with the $MAPbBr_3$ perovskite bandgap. The F3 sample showed a higher absorbance in the visible range. The photoluminescence spectra were collected with an integrating sphere equipped with a low intensity excitation source (Xe lamp) and a monochromator, using an excitation wavelength of 365 nm. While sample F3 showed weak but clear photoluminescence centered at 527 nm, no emission was observed for the F1 film.

In order to correlate the difference in the optical properties of the two perovskite samples with the material composition, solid state ^{13}C NMR analysis were performed on polycrystalline perovskite powders (Fig. 2), obtained by precipitation of concentrated solutions and annealed at 70 °C for 48 h.

The stoichiometric perovskite sample (P1) showed a single peak at 30.8 ppm, while an additional peak at 27.9 ppm was observed for the non-stoichiometric perovskite (P3). For comparison, the NMR spectra of the pure MABr precursor was also collected, showing a single signal at 27.9 ppm. Hence, the peak at higher chemical shift corresponds to the MA cation coordinated to the lead bromide (in the $MAPbBr_3$) in the perovskite structure, and the peak at lower chemical shift indicates the presence of a large amount of free MABr in the P3 sample. Fig. 2b reports the NMR spectrum of the non-stoichiometric perovskite sample with and without an additional thermal treatment at 115 °C for 24 h in air. Interestingly, in both samples the peak related to the free MABr is present and its

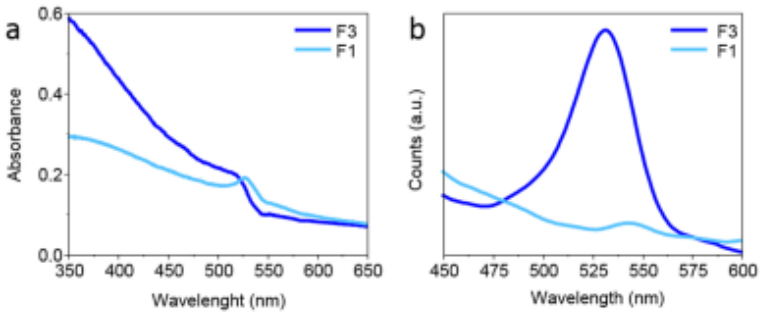

Fig. 1. (a) Absorption and (b) photoluminescence spectra of stoichiometric (F1) and non-stoichiometric (F3) $MAPbBr_3$ perovskite thin films.

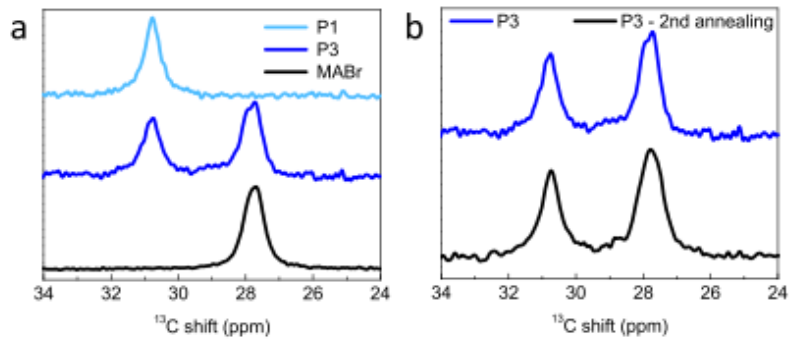

Fig. 2. (a) NMR spectra of non-stoichiometric (P3) and stoichiometric (P1) perovskite powders. (b) NMR spectra of the P3 sample before and after thermal annealing at 115 °C for 24 h.

intensity was not affected by the different thermal treatment. In both NMR spectra, the area ratio between the free and the bounded MABr is 1.38 (and not 2, as expected from the initial stoichiometry), suggesting that the total amount of unbound MABr decreases about 30% during the thermal treatment. Such loss is independent on the annealing temperature and time used in these experiments. The presence of MA cations was further investigated measuring the powder XRD, as depicted in Fig. 3.

The two diffractograms showed the expected diffraction pattern of the cubic $MAPbBr_3$ perovskite [36]. However, the diffraction pattern for the non-stoichiometric P3 sample revealed several additional peaks (highlighted in Fig. 3) originating from unbound methylammonium cations, further confirming the presence of a large amount of free organic cations even after thermal treatment (see Fig. S1 for reference MABr powder XRD).

To study the optoelectronic properties of the stoichiometric and non-stoichiometric perovskites, we prepared LEDs depositing the $MAPbBr_3$ active layers from the same solutions used to prepare the polycrystalline powders. The multilayer device structure used was ITO/PEDOT:PSS-Nafion® (100 nm)/$MAPbBr_3$/BmPyPhB (40 nm)/Ba (5 nm)-Ag (100 nm). The thickness of the active layer was about 900 nm. In Fig. 4 the current density (J) and luminance (L) versus voltage (V) characteristics are reported.

The J-V curve of the device prepared using the stoichiometric perovskite (LED1) showed high leakage current (a sign of not perfect diode morphology) at low applied bias, and no typical J-V diode characteristic. The current density passing through the device monotonically increases until about 8000 A/m^2 at 6 V. Electroluminescence was observed for voltages > 2.5 V, but the high current density strongly limited the device efficacy to 0.02 cd/A. On the other hand, the LED prepared using non-stoichiometric perovskite active layer (LED3) showed a typical J-V diode characteristic, with low leakage current and a sharp current density increase at about 1.8 V. Importantly, electroluminescence was observed at voltages as low as 2.2 V, and the luminance increased rapidly saturating at about 100 cd/m^2 at 6 V. The electroluminescence spectra of the two devices are reported in Fig. 4c. The emission wavelength for LED1 was centered at 545 nm, while the spectra for LED3 was slightly blue-shifted at 537 nm, in accordance with the small optical absorption mismatch (Fig. 1a). It is interesting to note that, despite the fact that the sample F1 does not show any photoluminescence, electroluminescence can be observed.

The electrical characteristics of the devices (especially the difference in the leakage current and diode behavior) suggests that the perovskite film morphology might play an important role in the charge transport and recombination. Consequently, SEM images of the films were collected, as depicted in Fig. 5.

The films present notable differences in the morphology as a function of the precursor ratio. Stoichiometric perovskite tends to form separate crystals with pseudo-cubic shapes and an average size of 5–10 μm. Importantly, these structures are not interconnected, as shown by the EDX mapping (Fig. 5b) where only the substrate (ITO/PEDOT:PSS) is present in between the perovskite crystals. The non-stoichiometric films, instead, are very uniform and compact, composed by fine crystals with no preferential orientation or defined grain boundaries. Interestingly we observed that the perovskite film morphology is rather independent on the nature of the substrate used (See Fig. S2 in the Supporting information). (See Supporting information Fig. S2).

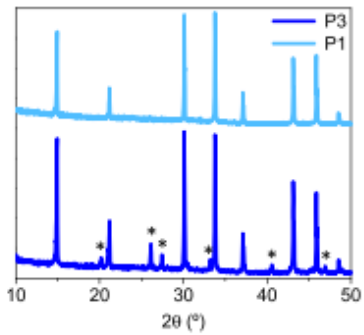

Fig. 3. XRD diffractograms for the stoichiometric (P1) and the non-stoichiometric (P3) perovskites powders.

4. Discussion

The compositional study of the perovskite films and powders revealed that the thermal treatment performed on the non-stoichiometric samples only removes about 30% of the initial amount of MABr. Even a prolonged annealing at higher temperature did not decrease the excess of organic cation in the non-stoichiometric perovskite. Hence, the discrepancies in the optical behavior and in the morphology are directly connected to the presence of the free MABr content in the non-

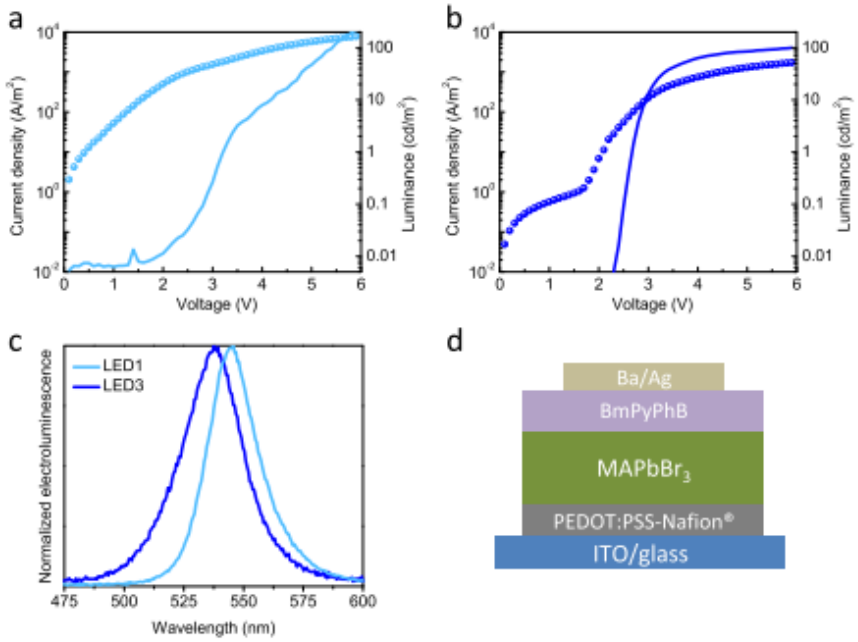

Fig. 4. (a) Current density (J, symbols) and luminance (lines) versus applied bias for (a) LED1, obtained with stoichiometric perovskite and for (b) LED3, employing non-stoichiometric perovskite active layer. (c) Electroluminescence spectra for the two devices and (d) device structure.

stoichiometric sample. The lower absorbance at lower wavelength observed for the stoichiometric films, can be ascribed to the lower coverage of the perovskite (as revealed by SEM). On the other hand, the absorption onset is also influenced by the stoichiometry, suggesting that the perovskite bandgap is slightly enlarged as the organic content increases. Similar studies were performed with methylammonium lead iodide, however a different behavior was observed [37,38]. Differences in the optical properties among $MAPbI_3$ perovskite obtained with different organic content were observed only without (or with very short) annealing. This implies that the MAI was efficiently removed during thermal treatment. In our case the MABr excess is maintained in the final material independently on the thermal treatment used, as observed by solid state NMR and XRD. We found the MABr excess to be beneficial for the film formation, since high surface coverage and low roughness are obtained. The morphology of the perovskite layer is of particular importance for applications in LEDs, where a uniform morphology results in an even distribution of the applied field. In fact, the high leakage current density measured for LED1 reflects the irregular structure observed by electronic microscopy. Since large voids are present in the perovskite films, a direct contact between the charge transport layers causes the high current density and low efficiency. In LED3 the current follows the different regimes characteristic of a diode thanks to the compact and flat semiconducting perovskite film sandwiched between the charge transport layers. For LED3, the fast increase of the current density is accompanied by a fast rise of the electroluminescence, meaning that the processes of charge injection, transport and recombination are better balanced compared to LED1. It is worth to note that despite the fact that electroluminescence was observed from both perovskite films, photoluminescence was obtained only from non-stoichiometric films. Most likely, the large amount of MABr present in the non-stoichiometric perovskite is able to passivate defect states which otherwise quench the luminescence in the stoichiometric crystals. In LEDs, trap states can be filled due to the large density of charge carriers injected, explaining why electroluminescence can be observed even from the stoichiometric perovskite. Other studies reported that the amount of methylammonium precursor can influence the semiconducting character of the perovskite, causing a more direct behavior of the bandgap that favors the band-to-band radiative recombination [39,40].

5. Conclusion

The results presented in this work highlight the large influence of the organic cation content in perovskite films for electroluminescent applications. The morphological study reveals that when an equimolar ratio of MABr and $PbBr_2$ is used, the perovskite films form as large, not-connected crystals. The excess of methylammonium bromide, on the other hand, favors the formation of a compact polycrystalline perovskite layer, with high surface coverage. The good quality of the layer is reflected by the good diode behavior obtained when the perovskite is used as active layer in an LED. The excess of methylammonium bromide also partially passivates the surface defects of the perovskite, leading to photoluminescence even with a low intensity excitation source. These homogeneous semiconducting films are particularly suitable for applications in thin-film optoelectronic devices such LEDs and solar cells.

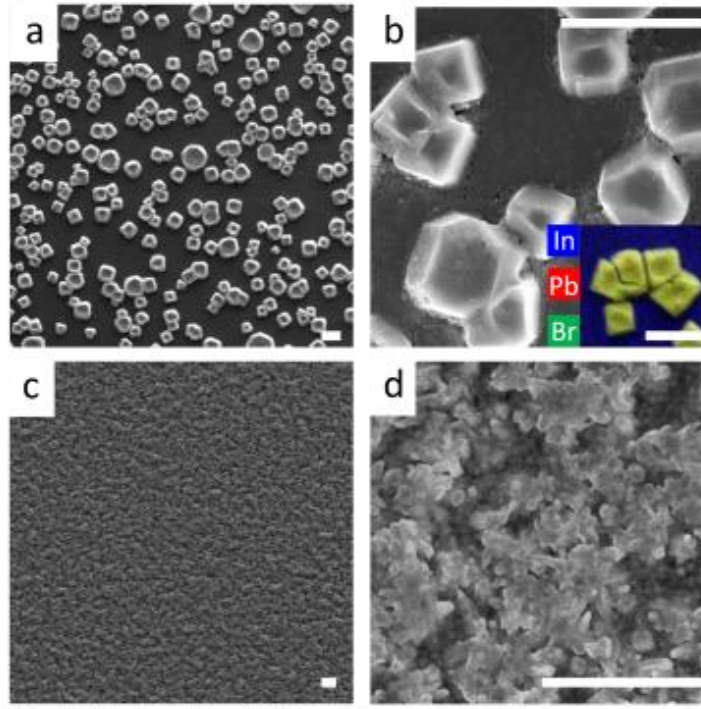

Fig. 5. SEM images of stoichiometric (a-b) and non-stoichiometric (c-d) perovskite layers. The inset in b) shows the energy dispersive X-ray analysis mapping of the stoichiometric sample. In all the images the scale bar is 10 μm.

Acknowledgments

The authors acknowledge financial support from the European Union 7th framework program project LUMINET (grant 316906), the Spanish Ministry of Economy and Competitiveness (MINECO) via the Unidad de Excelencia María de Maeztu MDM-2015-0538, MAT2014-55200-R, and PCIN-2015-255 and the Generalitat Valenciana (Prometeo/2016/135). A.W. is supported by a French National Research Agency under ANR-16-CE11-0023 (HRmicroMAS). M.S. thanks the MINECO for his post-doctoral (JdC) contract.

Appendix A. Supplementary material

Supplementary data associated with this article can be found in the online version at http://dx.doi.org/10.1016/j.jlumin.2017.03.048.

References

[1] H. Remy, G. Laves, Ber. Dtsch. Chem. Ges. (A B Ser.) 66 (1933) 401–407.
[2] D.B. Mitzi, C.A. Feild, W.T.A. Harrison, A.M. Guloy, Nature 369 (1994) 467–469.
[3] D.B. Mitzi, Chem. Mater. 8 (1996) 791–800.
[4] D.B. Mitzi, K. Chondroudis, C.R. Kagan, IBM J. Res. Dev. 45 (2001) 29–45.
[5] D.B. Mitzi, J. Mater. Chem. 14 (2004) 2355–2365.
[6] D.B. Mitzi, in: Prog. Inorg. Chem., John Wiley & Sons, Inc., 2007, pp. 1–121.
[7] T. Ishihara, J. Takahashi, T. Goto, Solid State Commun. 69 (1989) 933–936.
[8] T. Ishihara, J. Takahashi, T. Goto, Phys. Rev. B 42 (1990) 11099–11107.
[9] M. Era, S. Morimoto, T. Tsutsui, S. Saito, Appl. Phys. Lett. 65 (1994) 676–678.
[10] M. Era, S. Morimoto, T. Tsutsui, S. Saito, Synth. Met. 71 (1995) 2013–2014.
[11] N. Kitazawa, Y. Watanabe, Y. Nakamura, J. Mater. Sci. 37 (2002) 3585–3587.
[12] K. Tanaka, T. Takahashi, T. Ban, T. Kondo, K. Uchida, N. Miura, Solid State Commun. 127 (2003) 619–623.
[13] A. Kojima, K. Teshima, Y. Shirai, T. Miyasaka, J. Am. Chem. Soc. 131 (2009) 6050–6051.
[14] M.M. Lee, J. Teuscher, T. Miyasaka, T.N. Murakami, H.J. Snaith, Science 338 (2012) 643–647.
[15] M. Liu, M.B. Johnston, H.J. Snaith, Nature 501 (2013) 395–398.
[16] O. Malinkiewicz, A. Yella, Y.H. Lee, G.M. Espallargas, M. Graetzel, M. K. Nazeeruddin, H.J. Bolink, Nat. Photonics 8 (2014) 128–132.
[17] O. Malinkiewicz, C. Roldán-Carmona, A. Soriano, E. Bandiello, L. Camacho, M. K. Nazeeruddin, H.J. Bolink, Adv. Energy Mater. 4 (2014) 1400345.
[18] D. Bi, W. Tress, M.I. Dar, P. Gao, J. Luo, C. Renevier, K. Schenk, A. Abate, F. Giordano, J.-P. Correa Baena, J.-D. Decoppet, S.M. Zakeeruddin, M. K. Nazeeruddin, M. Grätzel, A. Hagfeldt, Sci. Adv. 2 (2016) e1501170.
[19] Z.-K. Tan, R.S. Moghaddam, M.L. Lai, P. Docampo, R. Higler, F. Deschler, M. Price, A. Sadhanala, L.M. Pazos, D. Credgington, F. Hanusch, T. Bein, H. J. Snaith, R.H. Friend, Nat. Nanotechnol. 9 (2014) 687–692.
[20] J.H. Noh, S.H. Im, J.H. Heo, T.N. Mandal, S.I. Seok, Nano Lett. 13 (2013) 1764–1769.
[21] F. Deschler, M. Price, S. Pathak, L.E. Klintberg, D.-D. Jarausch, R. Higler, S. Hüttner, T. Leijtens, S.D. Stranks, H.J. Snaith, M. Atatüre, R.T. Phillips, R. H. Friend, J. Phys. Chem. Lett. 5 (2014) 1421–1426.
[22] G. Xing, N. Mathews, S.S. Lim, N. Yantara, X. Liu, D. Sabba, M. Grätzel, S. Mhaisalkar, T.C. Sum, Nat. Mater. 13 (2014) 476–480.
[23] A. Sadhanala, S. Ahmad, B. Zhao, N. Giesbrecht, P.M. Pearce, F. Deschler, R.L. Z. Hoye, K.C. Gödel, T. Bein, P. Docampo, S.E. Dutton, M.F.L. De Volder, R. H. Friend, Nano Lett. 15 (2015) 6095–6101.
[24] J.C. Yu, D.B. Kim, G. Baek, B.R. Lee, E.D. Jung, S. Lee, J.H. Chu, D.-K. Lee, K.J. Choi, S. Cho, M.H. Song, Adv. Mater. 27 (2015) 3492–3500.
[25] Y.-H. Kim, H. Cho, J.H. Heo, T.-S. Kim, N. Myoung, C.-L. Lee, S.H. Im, T.-W. Lee, Adv. Mater. 27 (2015) 1248–1254.
[26] N. Sestu, M. Cadelano, V. Sarritzu, F. Chen, D. Marongiu, R. Piras, M. Mainas, F. Quochi, M. Saba, A. Mura, G. Bongiovanni, J. Phys. Chem. Lett. 6 (2015) 4566–4572.
[27] G. Li, Z.-K. Tan, D. Di, M.L. Lai, L. Jiang, J.H.-W. Lim, R.H. Friend, N.C. Greenham, Nano Lett. 15 (2015) 2640–2644.
[28] G. Longo, A. Pertegas, L. Martinez-Sarti, M. Sessolo, H.J. Bolink, J. Mater. Chem.

C 3 (2015) 11286–11289.
[29] H. Cho, S.-H. Jeong, M.-H. Park, Y.-H. Kim, C. Wolf, C.-L. Lee, J.H. Heo, A. Sadhanala, N. Myoung, S. Yoo, S.H. Im, R.H. Friend, T.-W. Lee, Science 350 (2015) 1222–1225.
[30] A. Abrusci, S.D. Stranks, P. Docampo, H.-L. Yip, A.K.Y. Jen, H.J. Snaith, Nano Lett. 13 (2013) 3124–3128.
[31] J. Burschka, N. Pellet, S.-J. Moon, R. Humphry-Baker, P. Gao, M.K. Nazeeruddin, M. Gratzel, Nature 499 (2013) 316–319.
[32] J.-W. Lee, N.-G. Park, MRS Bull. 40 (2015) 654–659.
[33] H. Zhou, Q. Chen, Y. Yang, MRS Bull. 40 (2015) 667–673.
[34] D. Forgacs, M. Sessolo, H.J. Bolink, J. Mater. Chem. A 3 (2015) 14121–14125.
[35] X. Zhang, H. Lin, H. Huang, C. Reckmeier, Y. Zhang, W.C.H. Choy, A.L. Rogach, Nano Lett. 16 (2016) 1415–1420.
[36] F. Zhu, L. Men, Y. Guo, Q. Zhu, U. Bhattacharjee, P.M. Goodwin, J.W. Petrich, E. A. Smith, J. Vela, ACS Nano 9 (2015) 2948–2959.
[37] J.S. Manser, B. Reid, P.V. Kamat, J. Phys. Chem. C 119 (2015) 17065–17073.
[38] N. Sakai, S. Pathak, H.-W. Chen, A.A. Haghighirad, S.D. Stranks, T. Miyasaka, H. J. Snaith, J. Mater. Chem. A 4 (2016) 4464–4471.
[39] X. Ke, J. Yan, A. Zhang, B. Zhang, Y. Chen, Appl. Phys. Lett. 107 (2015) 091904.
[40] C. Motta, F. El-Mellouhi, S. Kais, N. Tabet, F. Alharbi, S. Sanvito, Nat. Commun. 6 (2015) 7026.

Journal of
Materials Chemistry C

COMMUNICATION

View Article Online
View Journal | View Issue

Cite this: J. Mater. Chem. C, 2015, 3, 11286

Received 6th August 2015,
Accepted 12th October 2015

DOI: 10.1039/c5tc02447a

www.rsc.org/MaterialsC

Highly luminescent perovskite–aluminum oxide composites†

Giulia Longo, Antonio Pertegás, Laura Martínez-Sarti, Michele Sessolo* and Henk J. Bolink

In this communication we report on the preparation of $CH_3NH_3PbBr_3$ perovskite/Al_2O_3 nanoparticle composites in a thin film configuration and demonstrate their high photoluminescence quantum yield. The composite material is solution-processed at low temperature, using stable alumina nanoparticle dispersions. There is a large influence of the alumina nanoparticle concentration on the perovskite morphology and on its photoluminescence.

Recently, organic–inorganic (hybrid) metal halide perovskites have become the focus of renewed interest thanks to their remarkable performances in photovoltaics, as increasing power conversion efficiencies, now exceeding 20%, are being reported.[1–6] The most studied compound in photovoltaics is the methylammonium lead iodide $CH_3NH_3PbI_3$ perovskite, due to its strong bandgap absorption at about 1.6 eV. One of the interesting features of this class of semiconductors is that their optical properties can be modulated by simple substitution of their constituents.[7] The correspondent bromide compound $CH_3NH_3PbBr_3$ has a bandgap of about 2.3 eV, making it a good candidate for visible lasing and light-emission applications.[8,9] For both applications, the active material should show high photoluminescence quantum yield (PLQY), in order to efficiently convert the generated (either electrically or optically) charges into photons. Unfortunately, the photoluminescence (PL) of hybrid perovskites depends on the excitation intensity, being high at very high excitation intensity while very low when the excitation intensity decreases.[10] In electroluminescence, this means that high current densities are needed in order to produce significant light emission, which leads to a low power conversion efficiency of the devices.[8,11] A promising approach to reduce the non-radiative recombination in hybrid perovskites is the synthesis of nanoparticles. This has led to materials that show substantially enhanced photoluminescence, reaching PLQYs exceeding 90%.[12–15] The nanoparticle preparation, however, relies on complex chemical synthesis which might undermine the scalability of this approach. Moreover, the PLQY tends to substantially reduce when nanocrystals are processed as thin films, due to spontaneous aggregation of the perovskite.[16] It has also been shown how enhanced photoluminescence can be obtained by impregnation of a pre-formed mesoporous inorganic matrix (such as alumina) with the perovskite precursor solution, albeit a quantitative estimation of the PLQY has not been reported.[17,18] From a film forming/processing perspective, a more appealing approach is the deposition of composite films from blends of polymer or low molecular weight organic semiconductors, resulting in the formation of nano-/micro-domains of hybrid perovskites.[19,20] Here we present a hybrid approach for the preparation of high PLQY perovskite-based materials, which consists in the processing of blends of the perovskite precursor with stable alumina nanoparticle (NP) suspensions. Thin films were deposited at low temperature from solution, and a PLQY of up to 39% in the solid state was obtained. We show that the self-assembly of the alumina NPs constrains the growth of the perovskite to the nanoscale, resulting in the spontaneous formation of isotropic $CH_3NH_3PbBr_3$ nanocrystals.

The perovskite precursor solution was prepared by mixing $PbBr_2$ and CH_3NH_3Br in DMF in a 1 : 3 molar ratio. Subsequently, an aqueous dispersion of Al_2O_3 NPs with an average size of 10 nm was added to the perovskite precursor. Different amounts of Al_2O_3 NPs were used to evaluate the effect of the perovskite/NP ratio on the optical properties of the composite. Thin films of the composite materials were obtained by spin-coating the solution on glass or quartz substrates in air, followed by annealing on a hot plate at 90 °C for 1 hour. Processing of the composite films in air was possible due to their good stability to moisture. The origin of the relative moisture-insensitivity of $CH_3NH_3PbBr_3$:Al_2O_3 NP systems is not completely understood. In these films, however, most of the perovskite is surrounded by aluminum oxide, which is known to retard the degradation of hybrid perovskites.[21] On the other hand, pure $CH_3NH_3PbBr_3$ perovskite films were deposited and annealed in a nitrogen-filled glovebox, due to the limited stability of the compound in air.

Instituto de Ciencia Molecular (ICMOL), Universidad de Valencia, 46980 Paterna, Spain. E-mail: michele.sessolo@uv.es

† Electronic supplementary information (ESI) available: UV-Vis optical absorption of perovskite/Al_2O_3 NP films with high NP content (75 wt%). See DOI: 10.1039/c5tc02447a

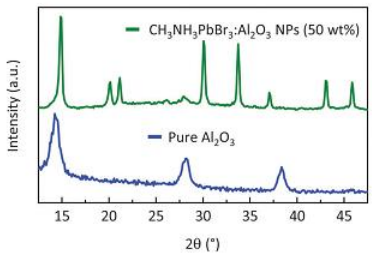

Fig. 1 GIXRD spectra of a mixed $CH_3NH_3PbBr_3/Al_2O_3$ thin film compared to the reference obtained from a pure Al_2O_3 NP layer.

The formation of crystalline perovskite was confirmed by grazing incidence X-ray diffraction (GIXRD) of the obtained thin films. In Fig. 1, the diffraction spectra of a composite film containing 50 wt% of alumina NPs are depicted. The spectra showed the diffraction pattern expected for $CH_3NH_3PbBr_3$, confirming the formation of the perovskite in the presence of a high concentration of alumina NPs.[22] The peak at 20.1° indicates that a small amount of the ammonium salt is still present in the composite film (see Fig. S1 in the ESI,† for the reference diffractogram of the pure CH_3NH_3Br and $CH_3NH_3PbBr_3$ compounds).

In Fig. 2a, the UV-Vis absorption spectra of a series of thin films with increasing Al_2O_3 NP content is depicted. The pure perovskite absorption spectra are shown as a reference. We observed that samples with low NP content (30 wt%) are not fully converted to the perovskite structure with this annealing time and temperature, as testified by the spectral feature at ~310 nm which corresponds to lead bromide complexes.[23] By increasing the alumina NP content, the peak at 310 nm fades while the absorption onset at ~525 nm, corresponding to the band-to-band transition of the perovskite, appears. These observations suggest that the presence of alumina NPs favors the perovskite formation. A similar enhanced crystallization has been observed for $CH_3NH_3PbI_3$ in mesoporous scaffolds.[2] Interestingly, perovskite/Al_2O_3 NP films with high NP content (75 wt%) spontaneously form the crystalline perovskite phase even at room temperature (Fig. S2, ESI†).

The photoluminescence characteristics of the Al_2O_3 NP thin films were studied using a Xe lamp coupled to a monochromator as the excitation source and a spectrometer coupled to an integrated sphere (Hamamatsu C9920-02 with a Hamamatsu PMA-11 optical detector) in order to quantitatively determine the PLQY. For the pure perovskite film and for films with a low NP content (<30 wt%), only weak photoluminescence could be observed, with PLQY values within the measurement error of the setup (<2%). This is partially due to the low excitation intensity used in the experiments (<0.4 mW cm^{-2}). On the other hand, with increasing NP loading, the typical green emission of the $CH_3NH_3PbBr_3$ perovskite started to rise (Fig. 2b). A strong dependence of the PLQY on the Al_2O_3 content is apparent which reaches a maximum of 26% for a NP concentration of 50 wt% (Fig. 2c). This PLQY is slightly higher than what was reported for thin films of colloidal $CH_3NH_3PbBr_3$ nanocrystals.[12] This is particularly striking when taking into account the simple material preparation and its processing in air from water-based dispersions. By increasing the annealing time at 90 °C to 3 hours, the PLQY of the $CH_3NH_3PbBr_3$:Al_2O_3 NP (50 wt%) composite thin films is

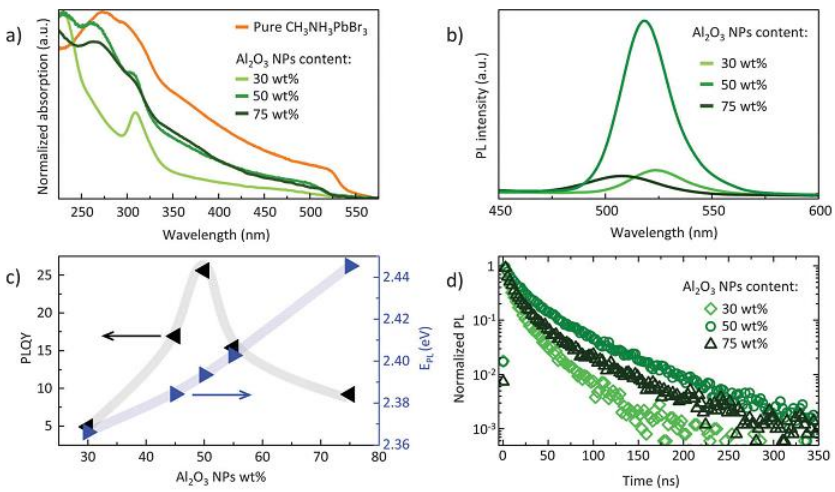

Fig. 2 Photophysical characterization of the composite $CH_3NH_3PbBr_3/Al_2O_3$ NP thin films with increasing NP concentration. (a) Normalized UV-Vis spectra of thin films, with the pure perovskite absorption reported as a reference and (b) correspondent photoluminescence spectra recorded by excitation at 380 nm. (c) Trend of the PLQY (black, left) and of the energy of the PL emission peak (blue, right) *vs.* Al_2O_3 NP loading. The broad lines in (c) are drawn as guide to the eye. (d) Time-resolved PL measurements taken at the peak emission wavelength of each sample, with a pump wavelength of 380 nm.

increased to 39%. Together with the increase in the PLQY with increasing Al_2O_3 NP content, a slight but continuous blue-shift of the emission energy occurs (Fig. 2d). This shift in emission wavelength was also observed in nano-sized $CH_3NH_3PbBr_3$ perovskite blended with organic semiconductors,[19] which was ascribed to quantum confinement effects. From GIXRD line broadening, a crystallite size of about 20 nm for the films containing 30 wt% Al_2O_3 NPs was derived. For such Al_2O_3 NP concentrations, the photoluminescence maxima is 2.37 eV, which agrees well with what reported for similar size perovskites.[19] Even considering the rough estimation of the size by GIXRD, here we tend to exclude quantum confinement effects, since the predicted Bohr radius for $CH_3NH_3PbBr_3$ (2.2 nm) is significantly smaller than the particle dimensions obtained in the Al_2O_3 NP–perovskite composite films.[24] Recently, D'Innocenzo *et al.* observed a similar (in magnitude) blue-shift of the photoluminescence peak when decreasing the crystallite size of $CH_3NH_3PbI_3$ thin films.[25] They associated the measured shift with a distortion of the I–Pb–I bond, which has been theoretically predicted and also experimentally observed by Raman spectroscopy.[26,27] Since such distortion would be especially significant in perovskites grown into a mesoporous scaffold, it might be responsible for the blue shift observed in our $CH_3NH_3PbBr_3/Al_2O_3$ NP blends. In order to gain further insights into the origin of the observed PLQY variation, the time-resolved PL was recorded for the same set of samples (Fig. 2d). We observed very fast PL decays with lifetimes τ_e (the time to reach 1/e of the initial intensity) of 9, 20 and 11 ns for the samples with NP content of 30, 50 and 75 wt%, respectively, in agreement with the presence of nano-sized perovskite crystallites.[25] A longer lifetime was recorded for the sample with higher PLQY (50 wt% NPs), suggesting a reduction of the nonradiative channels at this concentration.

For a structure–property correlation of the photoluminescence observed in the composite thin films, the material morphology was studied by scanning electron microscopy (SEM). The surface images of the samples with 30, 50 and 75 wt% Al_2O_3 NP content are reported in Fig. 3 (a, b, and c, respectively). Interestingly, we observed the presence of relatively large crystals (diameter of 2–4 μm) lying on a smooth surface. The profile of a single crystal was measured by atomic force microscopy (Fig. 3d), and found to protrude about 200 nm above the sample surface. A very similar morphology has been recently reported by Li *et al.* when solution processing films from $CH_3NH_3PbBr_3$ blends with an inert polymer.[20] In our films the system morphology is more complex since the background surface consists of an Al_2O_3 mesoporous scaffold observable at higher magnification (Fig. 3e). The composite material contains a large amount of $CH_3NH_3PbBr_3$ perovskite, as confirmed by energy dispersive X-ray analysis (EDXA, Fig. 3f). With increasing Al_2O_3 NP content, the formation of the crystals seems to be hindered (Fig. S4, ESI†), finally fading into round aggregates at the highest measured concentration (75 wt%, Fig. 3c). The observed perovskite super-structure on the alumina film is substantially different compared to the often referred to "capping layer" in the literature.[28] The capping layer is formed when a pure perovskite precursor solution is cast on top of a pre-formed mesoporous metal oxide film, resulting in excess,

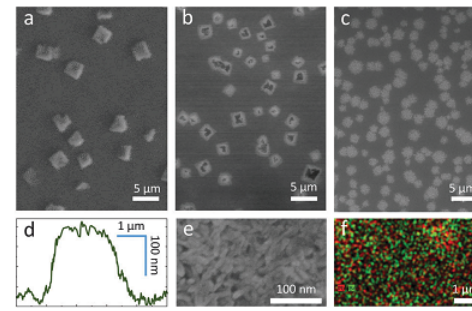

Fig. 3 SEM pictures of the mixed $CH_3NH_3PbBr_3/Al_2O_3$ NP thin films at 30, 50 and 75 wt% Al_2O_3 NP content (a, b, and c, respectively). (d) AFM profile of a single crystal from a sample containing 30 wt% Al_2O_3 NPs. (e) Higher magnification SEM image of the sample surface and (f) correspondent EDXA map for lead (red) and bromide (green).

superficial perovskite growth. While the photoluminescent properties of hybrid perovskites are expected to be morphology-dependent, the large structures observed in SEM images are unlikely the origin of the high photoluminescence observed. The observed blue-shift and the very short PL lifetime are more consistent when originating from perovskite crystals whose size is limited by the alumina NP scaffold. On the other hand, at low alumina concentration (<30 wt%) the perovskite aggregation within the alumina scaffold is obviously favored and this translates into PL quenching. In order to investigate the morphology of the $CH_3NH_3PbBr_3/Al_2O_3$ NP composite, transmission electron microscopy (TEM) was performed on powders obtained from scratched films. The TEM analysis (Fig. 4a) shows a morphology in accordance with that observed by SEM (Fig. 3e), where rod-like Al_2O_3 NPs assemble forming a dense mesoporous layer.

More interesting is the observation of a high concentration of isotropic nanoparticles with a considerably different contrast. The high resolution TEM (HR-TEM, Fig. 4b) shows that the observed

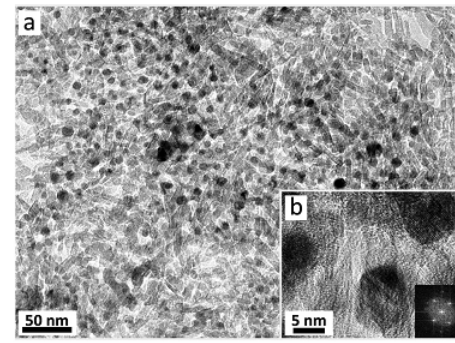

Fig. 4 (a) TEM picture of the mixed $CH_3NH_3PbBr_3/Al_2O_3$ NP thin films at 50 wt% Al_2O_3 NP content at different magnifications. The inset (b) is a HR-TEM image of few isolated NPs with the correspondent FFT.

nanoparticles are highly crystalline, and the fast Fourier transform (FFT) of a single nanocrystal confirms the presence of the cubic phase described for $CH_3NH_3PbBr_3$.[16] The electron microscopy hence confirms the formation of a nanostructured composite material where the growth of the hybrid perovskite is controlled and limited by the presence of the alumina NPs, as postulated by analyzing the photophysical properties.

Conclusions

In summary, high photoluminescence quantum yield $CH_3NH_3PbBr_3$ perovskite/alumina nanoparticle composite materials have been prepared. A strong enhancement of the photoluminescence as a consequence of the formation of perovskite nanocrystals is observed. The nanocrystal dimensions are governed by the size and concentration of the alumina nanoparticles. An optimum photoluminescence was found at 50 wt% of the alumina nanoparticles at which quantum yields up to 40% were recorded in thin solid films. Furthermore, these materials can be easily processed from solution at low temperature in air and are rather moisture insensitive, making them interesting candidates for future light-emitting and lasing applications.

Acknowledgements

This work was supported by the European Union 7th framework program LUMINET (grant 316906), the Spanish Ministry of Economy and Competitiveness (MINECO) (MAT2014-55200) and the Generalitat Valenciana (Prometeo/2012/053). The authors would like to thank Valerio D'Innocenzo for fruitful discussions on the optical lifetime measurements.

Notes and references

1 A. Kojima, K. Teshima, Y. Shirai and T. Miyasaka, *J. Am. Chem. Soc.*, 2009, **131**, 6050–6051.
2 M. M. Lee, J. Teuscher, T. Miyasaka, T. N. Murakami and H. J. Snaith, *Science*, 2012, **338**, 643–647.
3 J. Burschka, N. Pellet, S. J. Moon, R. Humphry-Baker, P. Gao, M. K. Nazeeruddin and M. Grätzel, *Nature*, 2013, **499**, 316–319.
4 N. J. Jeon, J. H. Noh, Y. C. Kim, W. S. Yang, S. Ryu and S. I. Seok, *Nat. Mater.*, 2014, **13**, 897–903.
5 H. Zhou, Q. Chen, G. Li, S. Luo, T. B. Song, H. S. Duan, Z. Hong, J. You, Y. Liu and Y. Yang, *Science*, 2014, **345**, 542–546.
6 N. J. Jeon, J. H. Noh, W. S. Yang, Y. C. Kim, S. Ryu, J. Seo and S. I. Seok, *Nature*, 2015, **517**, 476–480.
7 J. H. Noh, S. H. Im, J. H. Heo, T. N. Mandal and S. I. Seok, *Nano Lett.*, 2013, **13**, 1764–1769.
8 Z.-K. Tan, R. S. Moghaddam, M. L. Lai, P. Docampo, R. Higler, F. Deschler, M. Price, A. Sadhanala, L. M. Pazos, D. Credgington, F. Hanusch, T. Bein, H. J. Snaith and R. H. Friend, *Nat. Nanotechnol.*, 2014, **9**, 687–692.
9 Y.-H. Kim, H. Cho, J. H. Heo, T.-S. Kim, N. Myoung, C.-L. Lee, S. H. Im and T.-W. Lee, *Adv. Mater.*, 2015, **27**, 1248–1254.
10 F. Deschler, M. Price, S. Pathak, L. E. Klintberg, D.-D. Jarausch, R. Higler, S. Hüttner, T. Leijtens, S. D. Stranks, H. J. Snaith, M. Atatüre, R. T. Phillips and R. H. Friend, *J. Phys. Chem. Lett.*, 2014, **5**, 1421–1426.
11 L. Gil-Escrig, G. Longo, A. Pertegas, C. Roldan-Carmona, A. Soriano, M. Sessolo and H. J. Bolink, *Chem. Commun.*, 2015, **51**, 569–571.
12 L. C. Schmidt, A. Pertegás, S. González-Carrero, O. Malinkiewicz, S. Agouram, G. Mínguez Espallargas, H. J. Bolink, R. E. Galian and J. Pérez-Prieto, *J. Am. Chem. Soc.*, 2014, **136**, 850–853.
13 S. Gonzalez-Carrero, R. E. Galian and J. Perez-Prieto, *J. Mater. Chem. A*, 2015, **3**, 9187–9193.
14 F. Zhang, H. Zhong, C. Chen, X.-G. Wu, X. Hu, H. Huang, J. Han, B. Zou and Y. Dong, *ACS Nano*, 2015, **9**, 4533–4542.
15 H. Huang, A. S. Susha, S. V. Kershaw, T. F. Hung and A. L. Rogach, *J. Adv. Sci.*, 2015, **2**, 1500194.
16 F. Zhu, L. Men, Y. Guo, Q. Zhu, U. Bhattacharjee, P. M. Goodwin, J. W. Petrich, E. A. Smith and J. Vela, *ACS Nano*, 2015, **9**, 2948–2959.
17 A. Kojima, M. Ikegami, K. Teshima and T. Miyasaka, *Chem. Lett.*, 2012, **41**, 397–399.
18 M. Zhang, H. Yu, M. Lyu, Q. Wang, J.-H. Yun and L. Wang, *Chem. Commun.*, 2014, **50**, 11727–11730.
19 D. Di, K. P. Musselman, G. Li, A. Sadhanala, Y. Ievskaya, Q. Song, Z.-K. Tan, M. L. Lai, J. L. MacManus-Driscoll, N. C. Greenham and R. H. Friend, *J. Phys. Chem. Lett.*, 2015, **6**, 446–450.
20 G. Li, Z.-K. Tan, D. Di, M. L. Lai, L. Jiang, J. H.-W. Lim, R. H. Friend and N. C. Greenham, *Nano Lett.*, 2015, **15**, 2640–2644.
21 T. Leijtens, G. E. Eperon, S. Pathak, A. Abate, M. M. Lee and H. J. Snaith, *Nat. Commun.*, 2013, **4**, 2885.
22 E. Edri, S. Kirmayer, D. Cahen and G. Hodes, *J. Phys. Chem. Lett.*, 2013, **4**, 897–902.
23 K. G. Stamplecoskie, J. S. Manser and P. V. Kamat, *Energy Environ. Sci.*, 2015, **8**, 208–215.
24 K. Tanaka, T. Takahashi, T. Ban, T. Kondo, K. Uchida and N. Miura, *Solid State Commun.*, 2003, **127**, 619–623.
25 V. D'Innocenzo, A. R. Srimath Kandada, M. De Bastiani, M. Gandini and A. Petrozza, *J. Am. Chem. Soc.*, 2014, **136**, 17730–17733.
26 G. Grancini, S. Marras, M. Prato, C. Giannini, C. Quarti, F. De Angelis, M. De Bastiani, G. E. Eperon, H. J. Snaith, L. Manna and A. Petrozza, *J. Phys. Chem. Lett.*, 2014, **5**, 3836–3842.
27 C. Quarti, G. Grancini, E. Mosconi, P. Bruno, J. M. Ball, M. M. Lee, H. J. Snaith, A. Petrozza and F. D. Angelis, *J. Phys. Chem. Lett.*, 2014, **5**, 279–284.
28 M. De Bastiani, V. D'Innocenzo, S. D. Stranks, H. J. Snaith and A. Petrozza, *APL Mater.*, 2014, **2**, 081509.

Chapter 5.

General conclusions.

The aim of this thesis was to develop methods as well as materials for the preparation of perovskite optoelectronic devices. A wide number of techniques have been employed for the preparation of perovskite thin-films, which have been implemented both in solar cells and light-emitting diodes.

The flash evaporation, a novel method for the deposition of thin perovskite films suitable for solar cells have been presented in Chapter 2. The development of an optimized evaporation protocol is essential for the preparation of efficient devices. In particular, the evaporated film quality can be significantly influenced by the form of perovskite used as the precursor. It was found that if a thin perovskite layer is coated onto the metal foil (used as the heater), uniform heat exchange resulting in a homogeneous and fast film evaporation can be achieved. The best results were obtained when meniscus coating was employed to coat the metal heater. Under this condition, smooth and uniform perovskite films are readily deposited. When incorporated in multilayer solar cells, flash-evaporated perovskites lead to power conversion efficiency exceeding 12%, with an active layer thickness of only 250 nm.

In Chapter 3, the relationship between photovoltaic and electroluminescence phenomena in perovskite devices have been discussed. In particular, it has been demonstrated that efficient $MAPbI_3$ diodes prepared by dual source vacuum deposition, mainly studied for photovoltaic applications, also show intense electroluminescence when measured in forward bias. It has been observed that the electroluminescence efficiency of perovskite diodes is proportional to the current density injected in the device, as opposite to most OLEDs. In OLEDs the electroluminescence efficiency typically diminishes as the current density is increased, due to exciton-exciton annihilation. In perovskites, the low exciton binding energy leads to the formation of free carriers, hence the radiative band-to-band recombination is enhanced when trap states are filled at high current regimes. In order to increase the electroluminescence efficiency without thermal damage of the device at high currents, a pulsed driving mode was employed,

which allows to obtain twice as high efficiency compared to the device biased in direct current.

The results presented in Chapter 3 suggest that perovskites are characterized by a high concentration of traps that hinders radiative recombination hence limiting the electroluminescence efficiency. For this reason, the enhancement of the photoluminescence quantum yield (PLQY) is desirable for the preparation of efficient light-emitting diodes. In order to address this issue, the effect of the perovskite precursor stoichiometry and the addition of Al_2O_3 nanoparticles to the morphological and optical properties of $MAPbBr_3$ has been investigated. Through a preliminary study it was demonstrated that an excess of MABr helps the formation of compact and uniform films, enhancing the PLQY most likely due to passivating effect of the excess precursor. Thanks to the high film quality, the correspondent light-emitting diodes showed intense electroluminescence and low leakage current, further confirming the potential of perovskites as light-emitting materials. When Al_2O_3 nanoparticles were added to non-stoichiometric perovskites, the grain size of the material was strongly reduced, resulting in an enhancement of the PLQY up to 39 %. The luminescence characteristics are strongly dependent on the amount of alumina blended with the $MAPbBr_3$, with the most intense effect obtained for 50 wt.% loading in aluminum oxide. The incorporation of alumina also increases the PL lifetimes and the radiative rate constant, reducing the non-radiative path due to the passivation of traps states.

Chapter 6.

Resumen en Castellano.

Capítulo 6.1.

Introducción y objetivos de la tesis

6.1.1 Perovskitas híbridas

El nombre "perovskita", derivado del mineralogista ruso Lev Perovski, es usado para indicar todos los compuestos que presentan estructura cristalina generalizable en AMX_3. Una subclase específica de esta familia son las perovskitas híbridas, en las cuales el catión A es orgánico, M es un metal de transición divalente (Pb^{2+}) y X es un haluro. La estructura de las perovskitas híbridas de plomo consiste en un retículo de octaedros de haluro de plomo (PbX_6) unidos por los vértices, intercalados con los cationes orgánicos. Si el catión es bastante pequeño para caber en la cavidad determinada por cuatro octaedros plomo-halógeno (lo cual ocurre sólo si A es metilamonio o formamidinio), se forman estructuras tridimensionales (3D) estables. Si el catión orgánico es más grande, la estructura tridimensional colapsa en una bidimensional, donde láminas de tetraedros de plomo-halógenos (PbX_4) se alternan con capas de moléculas orgánicas. Aunque las estructuras 2D presenten interesantes características optoelectrónicas, en esta tesis se tratarán sólo perovskitas 3D.

Las perovskitas tridimensionales, en particular las de metilamonio ($MAPbX_3$), son materiales muy interesantes para aplicaciones optoelectrónicas por las siguientes razones:

- Fácil control del ancho de banda de los materiales.
  El fondo de la banda de conducción de las perovskitas híbridas está en su mayoría formado por los orbitales *p* de los átomos de plomo, mientras que la banda de valencia está caracterizada por los orbitales *p* de los átomos de halógenos. Por tanto, la substitución del anión corresponde a una modulación del band gap que se ensancha con halógenos más ligeros.

- Alto coeficiente de absorción.

  La fuerte absorción de luz por parte de la perovskita permite una alta generación de corriente con capas muy delgadas (≤ 500 nm) en células solares.

- Baja energía de enlace de los excitones.

  Esta característica permite una fácil y eficiente separación de los electrones y los huecos, fenómeno fundamental para aplicaciones fotovoltaicas. La energía de enlace puede ser aumentada cambiando el halógeno o a través de cambios morfológicos, permitiendo la aplicación de las perovskitas en dispositivos emisores de luz.

- Alta longitud de difusión y elevadas movilidades de cargas.

  Estas características de las perovskitas híbridas de metilamonio son de fundamental importancia para maximizar la extracción/inyección de carga desde/en la capa activa de perovskita, ya que permiten a los electrones y los huecos foto-generados ser extraídos antes de que recombinen.

- Precursores químicos baratos y simple preparación de los materiales

  Los haluros de metilamonio y de plomo son compuestos cuyo coste es muy bajo. Además, las perovskitas pueden ser preparadas fácilmente tanto desde disolución, como por técnicas en vacío.

6.1.2 Técnicas de deposición

Una de las ventajas de las perovskitas, comparadas con otros materiales semiconductores, consiste en la posibilidad de emplear diferentes técnicas de deposición para obtener capas de alta calidad.

Las técnicas de formación de capas de perovskitas se pueden dividir en dos clases: técnicas de disolución y técnicas de vacío. La siguiente lista presenta todas las posibles variantes de técnicas de formación.

Métodos basados en disolución:

- Deposición en un sólo paso (Fig. 3a)
- Deposición en un sólo paso con anti-disolventes (Fig. 3b)
- Deposición secuencial por rotación (*spin-coating*, Fig. 3c)
- Deposición secuencial por baño (*dip-coating*, Fig. 3d)

Métodos de vacío

- Co-evaporación (Fig. 4a)
- Evaporación *flash* (Fig. 4b)
- Evaporación secuencial (Fig. 4c)

La calidad de la capa delgada depende no sólo de la técnica empleada, sino también del tipo compuesto y del substrato. Por tanto, no se puede definir a priori una técnica ideal para la deposición de capas delgadas, y la elección del método de deposición tendrá que ser optimizada según las aplicaciones finales.

6.1.3 Principio de funcionamiento de células solares

En una célula solar el material fotoactivo absorbe la luz generando pares de electrones y huecos, que son extraídos hacia los electrodos por los materiales transportadores de tipo *n* y *p* respectivamente. Para que este proceso sea eficiente, los materiales activos tienen que presentar baja energía de enlace excitónica, alta movilidad y longitud de difusión de cargas, y pocos defectos que puedan actuar como trampas.

Para las células solares se identifican unos parámetros útiles al momento de evaluar su funcionamiento:

- Corriente de cortocircuito (J_{sc}, mA cm^{-2}, representa la corriente generada a 0 voltios, depende de la cantidad de fotones absorbidos, de la eficiencia de separación de carga, y de la eficiencia de extracción).

- Voltaje de circuito abierto (V_{oc}, V, es el máximo voltaje generado por una célula solar con corriente igual a 0).

- Factor de forma o Fill factor (*FF*, %, se define como la relación entre el punto de máxima potencia dividido entre el V_{oc} y la J_{sc}. Gráficamente representa la "cuadratura" de la curva de densidad de corriente contra el voltaje).

- Eficiencia de conversión energética (*PCE*, % expresada por el cociente del punto de máxima potencia de la célula y la potencia irradiada sobre el dispositivo).

- Eficiencia quántica externa (*EQE*, %, representa el número de electrones extraídos mediante los contactos por el número fotones incidentes sobre el dispositivo).

6.1.4 Principio de funcionamiento de diodos de emisión de luz

Los diodos orgánicos emisores de luz (OLEDs, del inglés *organic light-emitting diodes*) son dispositivos multicapas donde una capa de material luminiscente está intercalada entre capas de semiconductores orgánicos. Estos transportan selectivamente electrones y huecos confinándolos en el material activo donde recombinan radiativamente. Los LEDs de perovskita pueden ser representados a través de una unión p-i-n. En estas condiciones, tres regímenes de funcionamiento se pueden identificar en la curva de corriente-voltaje (J-V) del dispositivo: corriente de fuga (1), corriente de difusión (2) y régimen de corriente de flujo (3, Fig. 7).

Para comparar el rendimiento de diferentes dispositivos, se definen las siguientes características:

- Luminancia (cd m^{-2}, representa la intensidad en candelas de luz emitida por unidad de superficie del dispositivo).

- Densidad de corriente (A m^{-2}, corresponde a la intensidad de corriente por unidad de superficie del dispositivo).

- Eficiencia de corriente (cd A^{-1}, representa la cantidad de luz emitida por unidad eléctrica inyectada en el dispositivo).

- Eficiencia de potencia (lm W^{-1}, expresa la eficiencia, pero teniendo en cuenta también el voltaje aplicado al diodo).

- Eficiencia cuántica externa EQE (%, representa el número de fotones emitidos por electrones inyectados).

6.1.5 Objetivos de la tesis

El objetivo de esta tesis es el desarrollo de métodos y materiales apropiados para la preparación de capas delgadas de perovskitas híbridas, y su implementación en dispositivos optoelectrónicos. Se dedicará particular atención a las relaciones entre la naturaleza del material, el método de deposición y las propiedades optoelectrónicas.

El trabajo está organizado como sigue:

- *Células solares de perovskitas preparadas por evaporación flash.*
  Se desarrolla un simple método de evaporación por la preparación de células solares.

- *Dispositivos de perovskita con alta eficiencia fotovoltaica y electroluminiscente.*
  En este capítulo se presentan dispositivos optoelectrónicos de perovskitas preparados mediante co-evaporación que, además de presentar alta eficiencia fotovoltaica, lucen también electroluminiscencia.

- *Compuestos de perovskita-óxido de aluminio altamente luminiscentes.*
  En este capítulo se presenta un método prometedor para el aumento del rendimiento cuántico de fotoluminiscencia.

Cada capítulo se compone por una introducción del tema, seguida por una descripción detallada de las metodologías y por una discusión de los datos experimentales obtenidos.

Capítulo 6.2.

Células solares de perovskita preparadas por evaporación flash

6.2.1 Introducción

Como se ha presentado en el capítulo 1, las perovskitas, y en particular $MAPbI_3$, tienen una energía de enlace de los excitones fotogenerados muy baja, lo cual se traduce en generación de cargas libres a temperatura ambiente. Además, están caracterizadas por un alto coeficiente de absorción que permite crear altas foto-corrientes con capas relativamente delgadas (<500nm). La facilidad de preparación de estos materiales permite la utilización de muchos métodos de deposición, entre los cuales se encuentran técnicas de vacío que ya han sido utilizadas para la preparación de células solares de perovskitas muy eficientes. Un método potencialmente simple y rápido para la preparación de capas delgadas de $MAPbI_3$ es la evaporación con fuente única (conocida también como evaporación *flash*), donde se sublima la perovskita pre-formada en lugar de sus precursores. El material se pone encima de una hoja metálica puesta a su vez en una cámara de vacío. Haciendo pasar una alta corriente a través del metal, la perovskita evapora en pocos segundos. En este capítulo se presenta la primera utilización de esta técnica para la preparación de dispositivos fotovoltaicos.

6.2.2. Metodología

Todos los materiales empleados en este trabajo están disponibles comercialmente y se han empleado sin purificación posterior a su adquisición. El yoduro de metilamonio (MAI) se sintetizó haciendo reaccionar 30 mL de metilamina (40% en peso en metanol) con 32.3 mL de ácido yodhídrico (57% en peso en agua) en

un frasco de fondo redondo de 250 mL a 0 °C por 2 horas bajo agitación. El precipitado se recuperó quitando el disolvente en exceso a 50 °C en un evaporador rotatorio. El precipitado se lavó tres veces con éter etílico y se secó a 60 °C en un horno en vacío por 24 horas. Una disolución al 50% en peso de precursores se preparó mezclando en DMF el PbI_2 y el MAI previamente sintetizado, en proporción $MAI/PbI_2 = 3$. Las células solares de perovskita se prepararon sobre un sustrato de vidrio con contactos pre-formados de óxido de indio y estaño (ITO). A continuación, se depositó una capa de 80 nm de PEDOT:PSS por *spin-coating* (seguido por un tratamiento térmico de 150 °C por 15 minutos), y una capa de 20 nm de polyTPD. La perovskita se depositó encima del polyTPD por evaporación *flash* y el dispositivo se completó con una capa de 80 nm de PCBM como transportador de electrones. El cátodo (10 nm de Ba recubiertos con 100 nm de Ag) se depositó por evaporación térmica en vacío.

6.2.3 Discusión

En la evaporación *flash* el material que se quiere evaporar se dispone sobre una hoja de metal (normalmente tantalio) conectada entre dos electrodos en una cámara de vacío. Una vez alcanzadas condiciones de alto vacío (10^{-5} – 10^{-6} mbar), se hace pasar una corriente intensa a través del metal, que garantiza una rápida conducción del calor, causando la rápida sublimación del material. Con ésta técnica de deposición la calidad de la capa evaporada se ve muy influenciada por el tipo de material de partida, y se pueden apreciar notables diferencias si se utilizan polvos o si se deposita una capa delgada de material directamente sobre el tantalio. Así, a pesar de que este tipo de técnica permite la evaporación de materiales en polvo, resulta muy difícil obtener un recubrimiento uniforme de la hoja de tantalio, lo que causa una evaporación no uniforme del material con la consecuente formación de capas no homogéneas. Los mejores resultados se obtienen cuando se recubre el tantalio con una capa delgada de perovskita, en particular mediante la técnica de *meniscus coating*. De este modo, el calor se

reparte de manera muy rápida y homogénea en el material a evaporar. El grosor de la capa evaporada puede ser controlado, ya que hay una proporcionalidad directa entre la cantidad (en masa) de perovskita depositada en la hoja metálica y el grosor final de la capa sublimada. En el caso aquí presentado, el grosor de la capa de perovskita utilizado es de 250 nm (Fig. 11a). La capa así formada presenta el patrón de difracción de rayos X típico del $MAPbI_3$ (Fig. 11c), y muestra una superficie uniforme y relativamente plana (Fig. 11b). El espectro de absorción está caracterizado por un rápido aumento de la señal a 760-800 nm, confirmando la formación de $MAPbI_3$ (Fig. 11d). Estos resultados demuestran que la evaporación *flash* permite la formación de materiales altamente cristalinos en capa delgada, aptos para dispositivos optoelectrónicos. Una vez optimizado el proceso, se implementó la capa de perovskita así preparada en una célula solar, con estructura y materiales descritos en el parágrafo de metodología. Las células se caracterizaron en atmósfera inerte, utilizando una fuente de iluminación calibrada. La EQE del dispositivo es alta en el rango visible del espectro solar, alcanzando máximos por encima del 70% a 570 nm y 420 nm (Fig 12a), lo que conlleva una alta fotocorriente (18 mA cm^{-2}). La curva de corriente-voltaje de la célula solar en oscuridad (Fig. 12b), revela una baja corriente de fuga, indicando la baja defectuosidad del dispositivo. Los altos valores de J_{SC} y V_{OC} obtenidos bajo iluminación indican también que la recombinación de carga en el dispositivo es muy baja, probablemente gracias al uso combinado de capas bloqueadoras de electrones y huecos. La combinación de altos valores de corriente, voltaje y *fill factor* resultan en una elevada eficiencia de conversión de potencia, que supera el 12%.

6.2.4 Conclusiones

En este capítulo se ha presentado un método novedoso, la evaporación *flash*, para la deposición de capas delgadas de perovskita y su aplicación en células solares. El desarrollo de un protocolo de evaporación adapto es de fundamental

importancia para obtener dispositivos eficientes. Los mejores resultados se obtuvieron recubriendo la hoja de metal por *meniscus coating*, y utilizando la perovskita en forma de capa delgada para el proceso de evaporación *flash*. Las células solares preparadas con esta técnica presentan EQE altos y buenas prestaciones. Además, la posibilidad de añadir bloqueadores de electrones y huecos, permite aumentar ulteriormente la eficiencia del dispositivo.

Capítulo 6.3

Dispositivos de perovskita con alta eficiencia fotovoltaica y electroluminiscente

6.3.1 Introducción

Las células solares y los diodos emisores de luz son dispositivos basados en mecanismos de funcionamiento complementarios. Las transiciones electrónicas que controlan la recombinación radiativa de las cargas son las mismas que gobiernan los procesos de absorción, implicando una reciprocidad entre los dos fenómenos. En cortocircuito (V=0), la recombinación de la carga debería ser minima, y todos los fotones absorbidos convertidos en cargas libres que puedan extraerse a los electrodos. Por otra parte, en condiciones de voltaje de circuito abierto no se genera corriente, lo cual implica que todas las cargas fotogeneradas tienen que recombinar. Por esto las células solares más eficientes operan en el límite radiativo, donde el flujo de fotones absorbidos es igual al flujo emitido en condiciones de circuito abierto. El V_{OC} más alto se obtendrá, por tanto, cuando todos los procesos de recombinación que ocurren en el dispositivo sean radiativos, es decir, cuando la electroluminiscencia de la célula solar sea máxima. Esto implica que la EQE de electroluminiscencia (a voltajes similares al voltaje de circuito abierto) puede ser utilizada como un parámetro adicional para optimizar y comparar las prestaciones de diferentes células solares. En este trabajo, una célula solar de $MAPbI_3$ será caracterizada también como LED, polarizándola y midiendo la electroluminiscencia. Al aumentar el voltaje aplicado, las altas corrientes y la consecuente disipación de calor pueden causar la rápida degradación del material activo. Una solución a este problema es la aplicación de una corriente pulsada. En estas condiciones es posible aplicar altas corrientes por un tiempo muy corto, dejando que el sistema se relaje y que el calor acumulado se disipe cuando la corriente aplicada vuelve a cero. En este capítulo

se presenta un dispositivo multifuncional que presenta al mismo tiempo buena actividad fotovoltaica e intensa electroluminiscencia. La capa de perovskita se deposita por co-evaporación, y las propiedades luminiscentes se evalúan a través de la aplicación de corriente continua y pulsada.

6.3.2 Metodología

Todos los materiales empleados en este trabajo están disponibles comercialmente y se han utilizado sin purificación posterior a su adquisición. La arquitectura del dispositivo consiste en: ITO/PEDOT:PSS (80 nm)/polyTPD (20 nm)/$MAPbI_3$ (320 nm)/PCBM (100 nm)/Ba (10 nm)/Ag (100 nm). La capa de PEDOT:PSS se preparó por *spin-coating*, mientras que la capa de polyTPD se depositó mediante *meniscus coating*. Después de cada deposición las capas fueron sometidas a un tratamiento térmico como descrito en la metodología del capítulo 2. La capa de perovskita $MAPbI_3$ se preparó mediante co-evaporación de yoduro de metilamonio y yoduro de plomo. La perovskita se recubrió con una capa de PCBM de 100 nm de grosor, mediante *meniscus coating*. El dispositivo se completó con la deposición térmica en vacío de un cátodo metálico formado por 10 nm de Ba y 100 nm de Ag.

6.3.3 Discusión

La co-evaporación es una técnica que permite la formación de capas altamente cristalinas y con óptimas calidades opto-electrónicas, como se demuestra por el patrón de difracción de rayos-X, así como por el espectro de absorción. La ecuación de Scherrer permite estimar el tamaño medio de los cristales de perovskita en la capa, que en este caso resulta de alrededor de 35 nm. Para asegurar una buena inyección de carga en el dispositivo se utilizó un cátodo de bario (la plata depositada sirve principalmente para proteger el bario), cuya baja función de trabajo asegura que no haya barreras energéticas para la inyección de

electrones (Fig.13). Cuando el dispositivo se mide como una célula solar, presenta altas EQE con máximo de 90 % a 570 nm (Fig. 15a). Esto resulta en una corriente de cortocircuito que supera los 18 mA cm^{-2} y que, junto con alto V_{OC} (1.08 V) y alto FF (64%), genera una eficiencia ligeramente inferior a 13%.

Posteriormente a la caracterización fotovoltaica, el mismo dispositivo se caracterizó como si fuera un LED. Para esto, la corriente y la intensidad de electroluminiscencia (irradiancia, ya que el dispositivo emite en el infrarrojo cercano) se midieron durante un barrido de voltaje. La curva de la corriente-voltaje presenta muy baja corriente de fuga, confirmando la baja defectuosidad del dispositivo. Los diferentes regímenes de la curva de diodo son claramente identificables (Fig. 16a). En correspondencia con la inyección de carga, la electroluminiscencia sube rápidamente, llegando a 84 μW cm^{-2} a 2.5 V. El máximo del espectro de electroluminiscencia está posicionado en 765 nm, de acuerdo con el ancho de banda de la perovskita. A pesar del bajo voltaje necesario por obtener electroluminiscencia, que apunta a las buenas características de transporte del dispositivo, la EQE de electroluminiscencia es muy baja (0.014%), si se compara con otros LEDs que emiten en el infrarrojo. A diferencia de los OLEDs, la electroluminiscencia de los dispositivos de perovskita es directamente proporcional a la densidad de corriente, debido al progresivo llenado de los niveles asociados a trampas que causan la reducción de la recombinación radiativa. Así que, en principio, al aumentar la corriente podría alcanzarse una eficiencia más alta. Desafortunadamente, como estàa explicado anteriormente, la disipación de calor causado por altas corrientes puede ser perjudicial para la estabilidad de la capa emisora. A fin de evitar este efecto, se ha utilizado una corriente pulsada a una frecuencia de 100 Hz, con forma de onda cuadrada y ciclos de trabajo del 50%. Esto corresponde a un pulso de corriente de 5 ms alternado a un tiempo en reposo equivalente (Fig. 17a). Con esta técnica es posible aplicar corrientes de pico de 2300 mA cm^{-2} (equivalentes a una corriente media de 1150 mA cm^{-2}), obteniendo una irradiancia de 770 μW cm^{-2}. La mayoría de las células medidas en corriente pulsada presentan un EQE de

electroluminiscencia de 0.03%, que es el doble de lo obtenido con la aplicación de corriente continua.

6.3.4 Conclusiones

Se ha demostrado como los materiales de perovskita tienen un gran potencial tanto en aplicaciones fotovoltaicas como en dispositivos emisores de luz. Una célula solar de MAPI con eficiencia cerca de 13% exhibe también electroluminiscencia que, contrariamente a los LEDs orgánicos, incrementa al aumentar la densidad de corriente. Se ha demostrado que con la utilización de corriente pulsada, en lugar de la continua, es posible aplicar corrientes muy elevadas sin degradar la capa activa, alcanzando así valores de EQE de más del doble con respeto a los obtenidos en corriente continua.

Capítulo 6.4

Compuestos de perovskita-oxido de aluminio altamente luminiscentes.

6.4.1 Introducción

Recientemente las perovskita tridimensionales híbridas de bromo ($MAPbBr_3$) han sido señaladas como posibles materiales emisores en dispositivos electroluminiscentes. La EQE es un parámetro muy importante para definir las prestaciones de los dispositivos, y es proporcional al rendimiento cuántico de fotoluminiscencia (PLQY) (Ecuación 8). En consecuencia, la mejora del PLQY del material es fundamental para obtener dispositivos eficientes. Sin embargo, las perovskitas, como el $MAPbBr_3$, presentan PLQY muy baja, con luminiscencia apreciable sólo por medio de excitación intensa como la obtenida con un láser. Esto puede ser debido a la alta concentración de trampas electrónicas en el material, que aumentan la probabilidad de recombinación no-radiativa reduciendo el PLQY. La elevada concentración de carga generada con una fuente de excitación intensa permite llenar las trampas, con el consecuente incremento de la intensidad de fotoluminiscencia. Desde una perspectiva de dispositivo, materiales con altos PLQY a bajas intensidades de excitación son muy deseables, dado que esto se traduce en un bajo consumo de energía. La morfología tiene una fuerte influencia sobre las propiedades foto-físicas de las perovskitas, y mediante la formación de nanopartículas es posible aumentar sustancialmente el PLQY de $MAPbBr_3$ (en analogía con los puntos cuánticos de semiconductores inorgánicos). Una alternativa a la síntesis de nanopartículas consiste en mezclar la perovskita con un material que confine su crecimiento, como un polímero, donde el tamaño de las partículas depende de la agregación y de la cantidad de polímero añadido. Otra posibilidad para reducir el tamaño de los granos de $MAPbBr_3$ es la infiltración de la disolución de precursores de la perovskita en

una matriz porosa de óxido metálico. Se ha demostrado que la fotoluminiscencia del $MAPbBr_3$ aumenta si se deposita el material sobre Al_2O_3 mesoporoso, aunque no se ha cuantificado el PLQY. El medio poroso de alúmina se preparó con un proceso de sinterización a alta temperatura, lo que limita la aplicación de esta técnica a sustratos que sobrevivan a estas condiciones. En este capítulo se presentará una estrategia más versátil que consiste en la formación simultánea de la perovskita y de la matriz de óxido de aluminio a baja temperatura y en aire. Se prestará particular atención a la composición del precursor de la perovskita, cuya estequiometría ha sido optimizada en un estudio preliminar.

6.4.2 Metodología

Todos los materiales empleados en este trabajo están disponibles comercialmente y se han utilizado sin purificación posterior a su adquisición. Por el estudio preliminar del precursor de la perovskita, se prepararon una solución estequiométrica (MA/Pb = 1) y una no-estequiométrica (MA/Pb = 3) de MABr y $PbBr_2$ (70 mg/mL en DMF). Con estas disoluciones se prepararon capas delgadas de perovskita (denominadas F1 y F3 la estequiométrica y la no-estequiométrica, respectivamente) sobre vidrio por *spin-coating*. Las capas fueron sometidas a un tratamiento térmico de 90 °C durante 15 minutos. Estos estudios se llevaron a cabo en atmosfera inerte en una caja de guantes. Para las medidas de difracción de rayos-X y de resonancia magnética nuclear (NMR) en estado sólido, se prepararon muestras de polvo de perovskita por precipitación desde una disolución al 40 % en peso (en DMF) de precursores estequiométricos (P1) y no-estequiométricos (P3), usando clorobenceno como agente precipitante. Los materiales policristalinos obtenidos se secaron en horno a 70 °C durante 48 horas. Parte de la muestra P3 fue sometida a un ulterior tratamiento térmico a 115 °C durante 24 horas. Las mismas disoluciones se utilizaron también para la preparación de los diodos emisores de luz. La estructura de los dispositivos preparados es ITO/PEDOT:PSS:Nafion (80 nm)/$MAPbBr_3$ (900 nm)/BmPyPhB

(40 nm)/Ba (5 nm)/Ag (100 nm). La deposición de la capa de perovskita se llevó a cabo por *spin-coating* en caja de guantes con atmosfera de N_2, seguida por un tratamiento térmico a 100 °C por 15minutos.

Para la preparación de los compuestos perovskita-alúmina, diferentes cantidades en peso (30%, 50% y 75%) de nanopartículas de alúmina se añadieron a la disolución no-estequiométrica de perovskita (70 mg/mL en DMF). También en este caso, la capa delgada se depositó por *spin-coating*, con un tratamiento térmico de 90 °C por 1 hora. La deposición de las capas y el tratamiento térmico se llevaron a cabo en aire.

6.4.3 Discusión

Las perovskitas estequiométricas y la no-estequiométricas presentan diferencias tanto desde el punto de vista morfológico, como en sus propiedades opto-electrónicas. Por tanto, antes de preparar los compuestos de alúmina y perovskita, se llevó a cabo un estudio para evaluar que estequiometría de perovskita es la más adapta. La difracción de rayos-X (Fig. 19 izquierda) de la muestra P3 presenta numerosos picos adicionales comparada con la P1, debido al exceso de metilamonio. El mismo exceso es también apreciable en los espectros de ^{13}C NMR (Fig. 19 derecha). En el compuesto P3 coexisten dos señales de metilamonio, uno correspondiente a la sal enlazada (presente también en la muestra P1, pero ausente en la muestra de referencia de metilamonio puro), y otro asociado al metilamonio libre (única señal presente en la referencia de metilamonio). Es interesante destacar como, a diferencia de la correspondiente perovskita de yodo, el exceso de metilamonio se mantiene a pesar del tratamiento térmico adicional (como demuestran los dos picos en el espectro de NMR). Esto implica que el exceso de precursor orgánico se mantiene en la perovskita y, por tanto, tendrá un efecto en la morfología del material. De hecho la muestra estequiométrica se caracteriza por la presencia de cristales cúbicos grandes (micrométricos) con conectividad limitada y un bajo grado de recubrimiento del

sustrato. Por otra parte, la perovskita no-estequiométrica presenta una superficie uniforme y compacta, recubriendo completamente el sustrato. El cambio en la morfología se traduce además en un cambio de las propiedades optoelectrónicas de los materiales. El espectro de absorción de la muestra F1 se caracteriza por la presencia de un pico excitónico, característico de estructuras de gran tamaño, y el material no presenta fotoluminiscencia. Por el contrario, la muestra F3 no presenta señales excitónicas, pero sí exhibe fotoluminiscencia. Las prestaciones de los dispositivos electroluminiscentes preparados con las dos perovskitas reflejan sus diferentes morfologías. En particular el LED3, fabricado con perovskita no-estequiométrica, luce la eficiencia más alta. Este estudio preliminar demostró como el exceso de metilamonio resulta beneficioso para la formación y para la luminiscencia de la perovskita. Por eso, los compuestos de perovskita-alúmina se prepararon empleando una disolución de perovskita con exceso de metilamonio. Se prepararon compuestos de alúmina-perovskita con tres concentraciones diferentes de nanopartículas de alúmina: 30%, 50% and 75% en peso. Los espectros de absorción indican como la muestra con más alto contenido en óxido no muestra las características típicas de la perovskita de bromo, cuya formación es inhibida por la alta cantidad de nanopartículas inorgánicas. Por otro lado, de los espectros de fotoluminiscencia se puede apreciar fácilmente el efecto benéfico de la alúmina en el PLQY. En particular, para el compuesto al 50% de alúmina, se han obtenido valores de PLQY de hasta el 39 %. En cambio, el PLQY tras la incorporación de las nanopartículas de óxido de aluminio es claramente apreciable en el cambio de tiempo de vida de los estados excitados, que resultan mucho más largos comparados con $MAPbBr_3$. Esta modulación en la fotofísica de los compuestos se debe a un cambio en su morfología. Las imágenes obtenidas con microscopios electrónicos de barrido y de transmisión enseñan que en las capas coexisten nanopartículas y cristales grandes. El incremento del rendimiento cuántico de fotoluminiscencia es debido al aumento de la energía de enlace de los excitones, causado por la reducción del tamaño de las partículas de perovskita, así como a una pasivación de las trampas que se traduce en una menor constante de recombinación no-radiativa.

6.4.4 Conclusiones

En este capítulo se ha investigado como la incorporación de nanopartículas de óxido de aluminio puede incrementar sensiblemente el PLQY de $MAPbBr_3$. Se llevó a cabo un estudio preliminar sobre el efecto de la estequiometría de la perovskita, demostrando como un exceso de bromuro de metilamonio resulta beneficioso en términos de morfología y fotoluminiscencia de la capa. Por tanto, se empleó perovskita con exceso de metilamonio en la preparación de los compuestos con la alúmina. El mayor PLQY (39 %) fue registrado para la muestra con el 50 % de óxido de aluminio, y los análisis morfológicos revelaron la formación espontánea de nanopartículas de perovskita, responsables del aumento del PLQY y del tiempo de vida de fotoluminiscencia.

Capítulo 6.5

Conclusiones generales

El objetivo de esta tesis consistía en el desarrollo de métodos y materiales para la preparación de dispositivos optoelectrónicos de perovskita. Para la formación de capas delgadas de perovskita, se emplearon un amplio espectro de técnicas de deposición, preparando tanto células solares como diodos emisores de luz.

En el capítulo 2 se presentó la evaporación *flash*, una técnica novedosa para la deposición de capas aptas para ser implementadas en células solares. Para conseguir dispositivos eficientes, es esencial el perfeccionamiento del protocolo de evaporación. En particular, la calidad de la capa evaporada puede ser sustancialmente modificada dependiendo de la forma de la perovskita empleada como precursor. Los mejores resultados se obtuvieron cuando el material para evaporar es depositado en forma de capa delgada encima de la hoja de metal, asegurando un intercambio de calor uniforme entre metal y perovskita y causando la rápida evaporación del $MAPbI_3$. Con este método se prepararon células solares caracterizadas por una eficiencia superior al 12% con capas activas de perovskita de tan sólo 250 nm de grosor.

En el capítulo 3 se ha estudiado la relación entre fenómenos fotovoltaicos y electroluminiscentes en dispositivos de perovskitas. En particular se ha evidenciado como diodos de $MAPbI_3$, empleados principalmente como células solares, pueden comportarse también cómo dispositivos emisores de luz. La electroluminiscencia de las perovskitas, a diferencia de la de los diodos orgánicos emisores de luz, es directamente proporcional a la densidad de corriente inyectada en el dispositivo. Por tanto, para aumentar la eficiencia de luminiscencia sin dañar los dispositivos por el estrés térmico que conlleva las altas corrientes, se ha medido el diodo de perovskita en corriente pulsada. De este

modo, se ha podido obtener eficiencia doble comparada con la obtenida mediante corriente continua.

Los resultados presentados en el capítulo 3 indican que las perovskitas tridimensionales de metilamonio se caracterizan por una alta concentración de trampas electrónicas, que disminuyen las recombinaciones radiativas afectando negativamente la eficiencia de la electroluminiscencia. Por esta razón, un incremento del rendimiento cuántico de fotoluminiscencia es necesario para la preparación de diodos de perovskitas emisores de luz. El capítulo 4 propone una estrategia para aumentar el PLQY de $MAPbBr_3$, consistente en la preparación de compuestos de perovskita y Al_2O_3. Previamente se condujo un estudio para evaluar el efecto de la estequiometría de la perovskita, a través del cual se observó que un exceso de MABr ayuda a la formación de capas uniformes y compactas, y que además presentan un mayor PLQY. Cuando se añade el óxido de aluminio a la perovskita, el tamaño de los granos es reducido por efecto de la matriz de Al_2O_3, obteniendo un incremento del PLQY hasta el 39%. El comportamiento óptico de los compuestos perovskita-alúmina está dictado por la cantidad de Al_2O_3, y luminiscencia más intensa se ha alcanzado con el 50 wt.% de alúmina. En estas condiciones, el tiempo de vida y la constante radiativa de foto-luminiscencia se alargan gracias al mayor carácter excitónico de las nanopartículas de perovskitas, mientras que la componente no-radiativa se ve reducida por la pasivación de las trampas.

Bibliography

1. M. Konstantakou and T. Stergiopoulos, *J. Mater. Chem. A*, **2017**, DOI: 10.1039/C7TA00929A

2. C. C. Stoumpos, L. Frazer, D. J. Clark, Y. S. Kim, S. H. Rhim, A. J. Freeman, J. B. Ketterson, J. I. Jang and M. G. Kanatzidis, *J. Am. Chem. Soc.*, **2015**, 137, 6804-6819.

3. J.-C. Hebig, I. Kühn, J. Flohre and T. Kirchartz, *ACS Energy Lett*, **2016**, 1, 309-314.

4. A. Kulkarni, T. Singh, M. Ikegami and T. Miyasaka, *RSC Adv.*, **2017**, 7, 9456-9460.

5. C. Li, X. Lu, W. Ding, L. Feng, Y. Gao and Z. Guo, *Acta Crystallogr. B*, **2008**, 64, 702-707.

6. D. B. Mitzi, K. Chondroudis and C. R. Kagan, *IBM J. Res. Dev.*, **2001**, 45, 29-45.

7. T. Ishihara, *J. Lumin.*, **1994**, 60-61, 269-274.

8. X. Hong, T. Ishihara and A. V. Nurmikko, *Phys. Rev. B*, **1992**, 45, 6961-6964.

9. T. Ishihara, J. Takahashi and T. Goto, *Solid State Commun.*, **1989**, 69, 933-936.

10. T. Ishihara, J. Takahashi and T. Goto, *Phys. Rev. B*, **1990**, 42, 11099-11107.

11. H.-S. Kim, C.-R. Lee, J.-H. Im, K.-B. Lee, T. Moehl, A. Marchioro, S.-J. Moon, R. Humphry-Baker, J.-H. Yum, J. E. Moser, M. Gratzel and N.-G. Park, *Sci. Rep.*, **2012**, 2:591.

12. M. M. Lee, J. Teuscher, T. Miyasaka, T. N. Murakami and H. J. Snaith, *Science*, **2012**, 338, 643-647.

13. N. Kitazawa, Y. Watanabe and Y. Nakamura, *J. Mater. Sci.*, **2002**, 37, 3585-3587.

14. W.-J. W. Yin, J.-H. J. Yang, J. Kang, Y. Yan and S.-H. Wei, *J. Mater. Chem. A*, **2015**, 3, 8926-8942.

15. J. H. Noh, S. H. Im, J. H. Heo, T. N. Mandal and S. I. Seok, *Nano Lett.*, **2013**, 13, 1764-1769.

16. B. Suarez, V. Gonzalez-Pedro, T. S. Ripolles, R. S. Sanchez, L. Otero and I. Mora-Sero, *J.Phys. Chem. Lett.*, **2014**, 5, 1628-1635.

17. M. A. Green, A. Ho-Baillie and H. J. Snaith, *Nat. Photon.*, **2014**, 8, 506-514.

18. E. T. Hoke, D. J. Slotcavage, E. R. Dohner, A. R. Bowring, H. I. Karunadasa and M. D. McGehee, *Chem. Sci.*, **2015**, 6, 613-617.

19. R. Comin, G. Walters, E. S. Thibau, O. Voznyy, Z.-H. Lu and E. H. Sargent, *J. Mater. Chem. C*, **2015**, 3, 8839-8843.

20. G. Grancini, A. R. Srimath Kandada, J. M. Frost, A. J. Barker, M. De Bastiani, M. Gandini, S. Marras, G. Lanzani, A. Walsh and A. Petrozza, *Nat. Photon.*, **2015**, 9, 695-701.

21. J.-W. Lee and N.-G. Park, *MRS Bulletin*, **2015**, 40, 654-659.

22. M. Sessolo, C. Momblona, L. Gil-Escrig and H. J. Bolink, *MRS Bulletin*, **2015**, 40, 660-666.

23. H. Zhou, Q. Chen and Y. Yang, *MRS Bulletin*, **2015**, 40, 667-673.

24. L. Zheng, D. Zhang, Y. Ma, Z. Lu, Z. Chen, S. Wang, L. Xiao and Q. Gong, *Dalton Trans.*, **2015**, 44, 10582-10593.

25. D. T. Moore, H. Sai, K. W. Tan, D.-M. Smilgies, W. Zhang, H. J. Snaith, U. Wiesner and L. A. Estroff, *J. Am. Chem. Soc.*, **2015**, 137, 2350-2358.

26. G. Longo, A. Wong, M. Sessolo and H. J. Bolink, *J. Lumin.*, **2017**, 189, 120-125.

27. N. J. Jeon, J. H. Noh, Y. C. Kim, W. S. Yang, S. Ryu and S. I. Seok, *Nat. Mater.*, **2014**, 13, 897-903.

28. J. W. Jung, S. T. Williams and A. K. Y. Jen, *RSC Adv.*, **2014**, 4, 62971-62977.

29. H. Cho, S.-H. Jeong, M.-H. Park, Y.-H. Kim, C. Wolf, C.-L. Lee, J. H. Heo, A. Sadhanala, N. Myoung, S. Yoo, S. H. Im, R. H. Friend and T.-W. Lee, *Science*, **2015**, 350, 1222-1225.

30. J. Burschka, N. Pellet, S.-J. Moon, R. Humphry-Baker, P. Gao, M. K. Nazeeruddin and M. Gratzel, *Nature*, **2013**, 499, 316-319.

31. J.-H. Im, I.-H. Jang, N. Pellet, M. Grätzel and N.-G. Park, *Nat. Nano*, **2014**, 9, 927-932.

32. J.-H. Im, H.-S. Kim and N.-G. Park, *APL Mater.*, **2014**, 2, 081510.

33. K. Liang, D. B. Mitzi and M. T. Prikas, *Chem. Mater.*, **1998**, 10, 403-411.

34. M. Liu, M. B. Johnston and H. J. Snaith, *Nature*, **2013**, 501, 395-398.

35. O. Malinkiewicz, A. Yella, Y. H. Lee, G. M. Espallargas, M. Graetzel, M. K. Nazeeruddin and H. J. Bolink, *Nat. Photon.*, **2014**, 8, 128-132.

36. M. Era, T. Hattori, T. Taira and T. Tsutsui, *Chem. Mater.*, **1997**, 9, 8-10.

37. Q. Ma, S. Huang, X. Wen, M. A. Green and A. W. Y. Ho-Baillie, *Adv. Energy Mater.*, **2016**, 6, 1502202.

38. G. Longo, L. Gil-Escrig, M. J. Degen, M. Sessolo and H. J. Bolink, *Chem. Commun.*, **2015**, 51, 7376-7378.

39. C.-W. Chen, H.-W. Kang, S.-Y. Hsiao, P.-F. Yang, K.-M. Chiang and H.-W. Lin, *Adv. Mater.*, **2014**, 26, 6647-6652.

40. L. Gil-Escrig, A. Miquel-Sempere, M. Sessolo and H. J. Bolink, *J. Phys. Chem. Lett.*, **2015**, 6, 3743-3748.

41. Q. Chen, H. Zhou, Z. Hong, S. Luo, H.-S. Duan, H.-H. Wang, Y. Liu, G. Li and Y. Yang, *J. Am. Chem. Soc.*, **2013**, 136, 622-625.

42. F. Brivio, K. T. Butler, A. Walsh and M. van Schilfgaarde, *Phys. Rev. B*, **2014**, 89, 155204.

43. D. W. deQuilettes, S. Koch, S. Burke, R. K. Paranji, A. J. Shropshire, M. E. Ziffer and D. S. Ginger, *ACS Energy Lett.*, **2016**, 1, 438-444.

44. T. M. Brenner, D. A. Egger, A. M. Rappe, L. Kronik, G. Hodes and D. Cahen, *J. Phys. Chem. Lett.*, **2015**, 6, 4754-4757.

45. R. E. Brandt, V. Stevanović, D. S. Ginley and T. Buonassisi, *MRS Communications*, **2015**, 5, 265-275.

46. T. M. Brenner, D. A. Egger, L. Kronik, G. Hodes and D. Cahen, *Nat. Rev. Mater.*, **2016**, 1, 15007.

47. A. Baumann, S. Väth, P. Rieder, M. C. Heiber, K. Tvingstedt and V. Dyakonov, *J. Phys. Chem. Lett.*, **2015**, 6, 2350-2354.

48. M. Samiee, S. Konduri, B. Ganapathy, R. Kottokkaran, H. A. Abbas, A. Kitahara, P. Joshi, L. Zhang, M. Noack and V. Dalal, *Appl. Phys. Lett.*, **2014**, 105, 153502.

49. H.-S. Duan, H. Zhou, Q. Chen, P. Sun, S. Luo, T.-B. Song, B. Bob and Y. Yang, *Phys. Chem. Chem. Phys.*, **2015**, 17, 112-116.

50. X. Wu, M. T. Trinh, D. Niesner, H. Zhu, Z. Norman, J. S. Owen, O. Yaffe, B. J. Kudisch and X. Y. Zhu, *J. Am. Chem. Soc.*, **2015**, 137, 2089–2096.

51. S. D. Stranks and H. J. Snaith, *Nat. Nanotechnol.*, **2015**, 10, 391-402.

52. S. D. Stranks, G. E. Eperon, G. Grancini, C. Menelaou, M. J. Alcocer, T. Leijtens, L. M. Herz, A. Petrozza and H. J. Snaith, *Science*, **2013**, 342, 341.

53. X. Sun, R. Asadpour, W. Nie, A. D. Mohite and M. A. Alam, *IEEE Journal of Photovoltaics*, **2015**, 5, 1389-1394.

54. A. Kojima, K. Teshima, Y. Shirai and T. Miyasaka, *J. Am. Chem. Soc.*, **2009**, 131, 6050-6051.

55. J.-H. Im, C.-R. Lee, J.-W. Lee, S.-W. Park and N.-G. Park, *Nanoscale*, **2011**, 3, 4088-4093.

56. L. Etgar, P. Gao, Z. Xue, Q. Peng, A. K. Chandiran, B. Liu, M. K. Nazeeruddin and M. Grätzel, *J. Am. Chem. Soc.*, **2012**, 134, 17396-17399.

57. J. H. Heo, S. H. Im, J. H. Noh, T. N. Mandal, C.-S. Lim, J. A. Chang, Y. H. Lee, H.-j. Kim, A. Sarkar, K. NazeeruddinMd, M. Gratzel and S. I. Seok, *Nat. Photon.*, **2013**, 7, 486-491.

58. J. H. Park, J. Seo, S. Park, S. S. Shin, Y. C. Kim, N. J. Jeon, H.-W. Shin, T. K. Ahn, J. H. Noh, S. C. Yoon, C. S. Hwang and S. I. Seok, *Adv. Mater.*, **2015**, 27, 4013-4019.

59. Z. Song, S. C. Watthage, A. B. Phillips and M. J. Heben, *J. Photon. Energy*, **2016**, 6, 022001.

60. J. Wang, N. Wang, Y. Jin, J. Si, Z.-K. Tan, H. Du, L. Cheng, X. Dai, S. Bai, H. He, Z. Ye, M. L. Lai, R. H. Friend and W. Huang, *Adv. Mater.*, **2015**, 27, 2311-2316.

61. J. C. Yu, D. B. Kim, G. Baek, B. R. Lee, E. D. Jung, S. Lee, J. H. Chu, D.-K. Lee, K. J. Choi, S. Cho and M. H. Song, *Adv. Mater.*, **2015**, 27, 3492-3500.

62. W. G. Aulbur, L. Jönsson and J. W. Wilkins, *Solid State Phys.*, **2000**, 54, 1-218.

63. S. De Wolf, J. Holovsky, S.-J. Moon, P. Löper, B. Niesen, M. Ledinsky, F.-J. Haug, J.-H. Yum and C. Ballif, *J. Phys. Chem. Lett.*, **2014**, **5**, 1035-1039.

64. V. D'Innocenzo, G. Grancini, M. J. P. Alcocer, A. R. S. Kandada, S. D. Stranks, M. M. Lee, G. Lanzani, H. J. Snaith and A. Petrozza, *Nat. Commun.*, **2014**, 5, 3586.

65. K. Tanaka, T. Takahashi, T. Ban, T. Kondo, K. Uchida and N. Miura, *Solid State Commun.*, **2003**, 127, 619-623.

66. M. Saba, M. Cadelano, D. Marongiu, F. Chen, V. Sarritzu, N. Sestu, C. Figus, M. Aresti, R. Piras, A. Geddo Lehmann, C. Cannas, A. Musinu, F. Quochi, A. Mura and G. Bongiovanni, *Nat. Commun.*, **2014**, 5, 5049.

67. A. Miyata, A. Mitioglu, P. Plochocka, O. Portugall, J. T.-W. Wang, S. D. Stranks, H. J. Snaith and R. J. Nicholas, *Nat. Phys.*, **2015**, 11, 582-587.

68. A. R. Srimath Kandada and A. Petrozza, *Accounts Chem. Res.*, **2016**, 49, 536-544.

69. Y. Zhao and K. Zhu, *Chem. Soc. Rev.*, **2016**, 45, 655-689.

70. Y. Dang, D. Ju, L. Wang and X. Tao, *CrystEngComm.*, **2016**, 18, 4476-4484.

71. W. S. Yang, J. H. Noh, N. J. Jeon, Y. C. Kim, S. Ryu, J. Seo and S. I. Seok, *Science*, **2015**, 348, 1234-1237.

72. D. Bi, W. Tress, M. I. Dar, P. Gao, J. Luo, C. Renevier, K. Schenk, A. Abate, F. Giordano, J.-P. Correa Baena, J.-D. Decoppet, S. M. Zakeeruddin, M. K. Nazeeruddin, M. Grätzel and A. Hagfeldt, *Sci. Adv.*, **2016**, 2, e1501170.

73. M. Saliba, T. Matsui, J.-Y. Seo, K. Domanski, J.-P. Correa-Baena, M. K. Nazeeruddin, S. M. Zakeeruddin, W. Tress, A. Abate, A. Hagfeldt and M. Gratzel, *Energ. Environ. Sci.*, **2016**, 9, 1989-1997.

74. C. Momblona, L. Gil-Escrig, E. Bandiello, E. M. Hutter, M. Sessolo, K. Lederer, J. Blochwitz-Nimoth and H. J. Bolink, *Energ. Environ. Sci.*, **2016**, 9, 3456-3463.

75. L. Harris and B. M. Siegel, *J. Appl. Phys.*, **1948**, 19, 739-741.

76. J. L. Richards, P. B. Hart and L. M. Gallone, *J. Appl. Phys.*, **1963**, 34, 3418-3420.

77. D. B. Mitzi, M. T. Prikas and K. Chondroudis, *Chem. Mater.*, **1999**, 11, 542-544.

78. K. Chondroudis and D. B. Mitzi, *Chem. Mater.*, **1999**, 11, 3028-3030.

79. S. Ahmad, C. Hanmandlu, P. K. Kanaujia and G. V. Prakash, *Opt. Mater. Express*, **2014**, 4, 1313-1323.

80. K. Tvingstedt, O. Malinkiewicz, A. Baumann, C. Deibel, H. J. Snaith, V. Dyakonov and H. J. Bolink, *Sci. Rep.*, 2014, **4**, 6071.

81. T. Kirchartz, A. Helbig, W. Reetz, M. Reuter, J. H. Werner and U. Rau, *Progress in Photovoltaics: Research and Applications*, **2009**, 17, 394-402.

82. T. Trupke, P. Würfel, I. Uhlendorf and I. Lauermann, *J. Phys. Chem. B*, **1999**, 103, 1905-1910.

83. K. Vandewal, K. Tvingstedt, A. Gadisa, O. Inganas and J. V. Manca, *Nat. Mater.*, **2009**, 8, 904-909.

84. O. Grånäs, D. Vinichenko and E. Kaxiras, *Sci. Rep.*, **2016**, 6, 36108.

85. W. E. I. Sha, X. Ren, L. Chen and W. C. H. Choy, *Appl. Phys. Lett.*, **2015**, 106, 221104.

86. D. Tordera, S. Meier, M. Lenes, R. D. Costa, E. Ortí, W. Sarfert and H. J. Bolink, *Adv. Mater.*, **2012**, 24, 897-900.

87. O. Malinkiewicz, M. Lenes, H. Brine and H. J. Bolink, *RSC Adv.*, **2012**, 2, 3335-3339.

88. C. Borek, K. Hanson, P. I. Djurovich, M. E. Thompson, K. Aznavour, R. Bau, Y. Sun, S. R. Forrest, J. Brooks, L. Michalski and J. Brown, *Angew. Chem. Int. Ed.*, **2007**, 46, 1109-1112.

89. A. Pertegas, N. M. Shavaleev, D. Tordera, E. Orti, M. K. Nazeeruddin and H. J. Bolink, *J. Mater. Chem. C*, **2014**, 2, 1605-1611.

90. F. Deschler, M. Price, S. Pathak, L. E. Klintberg, D. D. Jarausch, R. Higler, S. Hüttner, T. Leijtens, S. D. Stranks, H. J. Snaith, M. Atatüre, R. T. Phillips and R. H. Friend, *J. Phys. Chem. Lett.s*, **2014**, 5, 1421-1426.

91. L. C. Schmidt, A. Pertegás, S. González-Carrero, O. Malinkiewicz, S. Agouram, G. Mínguez Espallargas, H. J. Bolink, R. E. Galian and J. Pérez-Prieto, *J. Am. Chem. Soc.*, **2014**, 136, 850-853.

92. S. Gonzalez-Carrero, R. E. Galian and J. Perez-Prieto, *J. Mater. Chem. A*, **2015**, 3, 9187-9193.

93. H. Huang, A. S. Susha, S. V. Kershaw, T. F. Hung and A. L. Rogach, *Adv. Sci.*, **2015**, 2, 1500194.

94. F. Zhu, L. Men, Y. Guo, Q. Zhu, U. Bhattacharjee, P. M. Goodwin, J. W. Petrich, E. A. Smith and J. Vela, *ACS Nano*, **2015**, 9, 2948-2959.

95. D. Di, K. P. Musselman, G. Li, A. Sadhanala, Y. Ievskaya, Q. Song, Z.-K. Tan, M. L. Lai, J. L. MacManus-Driscoll, N. C. Greenham and R. H. Friend, *J. Phys. Chem. Lett.*, **2015**, 6, 446-450.

96. J. Li, S. G. R. Bade, X. Shan and Z. Yu, *Adv. Mater.*, **2015**, 27, 5196-5202.

97. G. Li, Z.-K. Tan, D. Di, M. L. Lai, L. Jiang, J. H.-W. Lim, R. H. Friend and N. C. Greenham, *Nano Lett.*, **2015**, 15, 2640-2644.

98. A. Kojima, M. Ikegami, K. Teshima and T. Miyasaka, *Chem. Lett.*, **2012**, 41, 397-399.

99. X. Zhang, H. Lin, H. Huang, C. Reckmeier, Y. Zhang, W. C. H. Choy and A. L. Rogach, *Nano Lett.*, **2016**, 16, 1415-1420.

100. J. S. Manser, B. Reid and P. V. Kamat, *J. Phys. Chem. C*, **2015**, 119, 17065-17073.

101. N. Sakai, S. Pathak, H.-W. Chen, A. A. Haghighirad, S. D. Stranks, T. Miyasaka and H. J. Snaith, *J. Mater. Chem. A*, **2016**, 4, 4464-4471.

102. K. G. Stamplecoskie, J. S. Manser and P. V. Kamat, *Energ. Environ. Sci.*, **2015**, 8, 208-215.

103. V. D'Innocenzo, A. R. Srimath Kandada, M. De Bastiani, M. Gandini and A. Petrozza, *J. Am. Chem. Soc.*, **2014**, 136, 17730-17733.

104. K. Zheng, Q. Zhu, M. Abdellah, M. E. Messing, W. Zhang, A. Generalov, Y. Niu, L. Ribaud, S. E. Canton and T. Pullerits, *J. Phys. Chem. Lett.*, **2015**, 6, 2969-2975.

Other contributions of the author

1. S. Keller; A. Pertegás; G. Longo; L. Martínez; J. Cerdá; J. M. Junquera-Hernández; A. Prescimone; E. C. Constable; C. E. Housecroft; E. Ortí; H. J. Bolink; "Shine bright or live long: substituent effects in [Cu(N^N)(P^P)]+-based light-emitting electrochemical cells where N^N is a 6-substituted 2,2′-bipyridine." *Journal of Material Chemistry C*, **2016**, 4, 3857

2. M. Sessolo; L. Gil-Escrig, G. Longo; H. J. Bolink. "Perovskite Luminescent Materials." *Topics in Current Chemistry*, **2016**, 374, 52.

3. N. Kaihovirta; G. Longo; L. Gil-Escrig; H. J. Bolink; L. Edman. "Self-absorption in a light-emitting electrochemical cell based on an ionic transition metal complex." *Applied Physics Letters*, **2015**, 106, 103502

4. A. M. Bünzli; E. C. Constable; C. E. Housecroft; A. Prescimone; J. A. Zampese; G. Longo; L. Gil-Escrig; A. Pertegás; E. Ortí; H. J. Bolink. "Exceptionally long-lived light-emitting electrochemical cells: multiple intra-cation pi-stacking interactions in [Ir(C^N)2(N^N)][PF6] emitters." *Chem. Sci.*, **2015**, 6, 2843

5. C. Roldán-Carmona; O. Malinkiewicz; R. Betancur; G. Longo; C. Momblona; F. Jaramillo; L. Camacho; H. J. Bolink. "High efficiency single-junction semitransparent perovskite solar cells." *Energy & Environmental Science*, **2014**, 7, 351

6. S. Keller; E. C. Constable; C. E. Housecroft; M. Neuburger; A. Prescimone; G. Longo; A. Pertegás; M. Sessolo; H. J. Bolink. "[Cu(bpy)(P^P)]+

containing light-emitting electrochemical cells: improving performance through simple substitution." *Dalton Transactions*, **2014**, 43, 16593

7. F. Fresno; G. Longo; S. Gross; U. Lavrencic Stangar. “Synthesis of $BiVO_4/TiO_2$ composites and evaluation of their photocatalytic activity under indoor illumination.” *Environmental science and pollution research international*, 2014.

List of abbreviations

AFM	Atomic force microscopy
BmPyPhB	1,3-Bis[3,5-di(pyridin-3-yl)phenyl]benzene
DC	Direct current
DMF	Dimethylformamide
E_g	Band gap energy
ETM	Electron transport material
EQE	External quantum efficiency
FF	Fill factor
GOPS	glycidoxypropyltrimethoxysilane
HOMO	Highest occupied molecular orbital
HTM	Hole transport material
I	Current
ITO	Indium tin oxide
J	Current density
J_{SC}	Short circuit current density
LED, OLED, PeLED	Light emitting diodes, organic-LED, perovskite-LED
LUMO	Lowest unoccupied molecular orbital
$MAPbBr_3$	Methylammonium lead tribromide
$MAPbI_3$	Methylammonium lead triiodide

NP	Nanoparticles
NMR	Nuclear magnetic resonance
PCE	Power conversion efficiency
PCBM	(6,6)-phenyl C61-butyric acid methyl ester
PL	Photoluminescence
PLQY	Photoluminescence quantum yield
PEDOT:PSS	Poly(3,4ethylenedioxythiophene)-poly(styrenesulfonate)
polyTPD	poly(N,N0-bis(4-butylphenyl)-N,N0-bis(phenyl)benzidine)
SEM	Scanning electron microscopy
TEM	Transmission electron microscopy
TPBi	2,2',2''-(1,3,5-Benzinetriyl)-tris(1-phenyl-1-H-benzimidazole
V	Voltage
V_{bi}	Built-in voltage
V_{OC}	Open circuit voltage
XRD	X-Ray diffraction